Final Technical Report
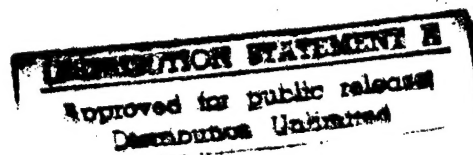

Ocean Optical Modeling: Higher Order Interactions, Light Field Structure, and Internal Radiant Emission

Robert Hans Stavn
Department of Biology
University of North Carolina at Greensboro
Greensboro, NC 27412

Telephone: (910) 334-5391 ex. 18
FAX: (910) 334-5839

e-mail: stavnrh@iris.uncg.edu

19970227 338

REPORT DOCUMENTATION PAGE

1. AGENCY USE ONLY (Leave blank)	2. REPORT DATE January 1997	3. REPORT TYPE AND DATES COVERED Final Technical Fiscal 1990-1994

4. TITLE AND SUBTITLE

Ocean Optical Modeling: Light Field Structure, Internal Radiant Emission, and Vertical Inhomogeneities

5. FUNDING NUMBERS
G
N00014-89-J-3137

6. AUTHOR(S)

Robert H. Stavn

7. PERFORMING ORGANIZATION NAME(S) AND ADDRESS(ES)

Dept. of Biology
Univ. of North Carolina/Greensboro
Greensboro, NC 27412

8. PERFORMING ORGANIZATION REPORT NUMBER

9. SPONSORING / MONITORING AGENCY NAME(S) AND ADDRESS(ES)

Office of Naval Research
Ocean Science Directorate
Ocean Optics Division
800 N. Quincy Street
Arlington, VA 22217-5000

10. SPONSORING / MONITORING AGENCY REPORT NUMBER

11. SUPPLEMENTARY NOTES

Approved for Public Release: Distribution unlimited

12a. DISTRIBUTION / AVAILABILITY STATEMENT

Portions published in Applied Optics, Journal of Geophysical Research, and Proceedings, Soc. Photo-Opt. Inst. Engineers

12b. DISTRIBUTION CODE

13. ABSTRACT (Maximum 200 words)

This report documents the controlling effects of light field geometry and internal radiant emission on the apparent optical properties used to construct simplified optical inversion algorithms for Case 1 waters. Monte Carlo simulations utilizing the accepted physical properties of the water molecule and suspended matter are utilized to solve the Radiative Transfer Equation and generate apparent optical properties. Water Raman scattering activity is documented in clear ocean waters and algorithms proposed to evaluate water Raman scattering quantitatively. The geometry of light fields from open ocean to Case 1 coastal waters is evaluated relative to individual volume scattering functions of hydrosol components. From this information, correction factors are proposed for remote-sensing algorithms that invert the radiance-irradiance field to retrieve the backscattering coefficient.

14. SUBJECT TERMS

ocean optics, water Raman scattering, optical energy trapping, remote sensing reflectance, backscattering coefficient

15. NUMBER OF PAGES

96

16. PRICE CODE

17. SECURITY CLASSIFICATION OF REPORT	18. SECURITY CLASSIFICATION OF THIS PAGE	19. SECURITY CLASSIFICATION OF ABSTRACT	20. LIMITATION OF ABSTRACT
UNCLASSIFIED	UNCLASSIFIED	UNCLASSIFIED	

Introduction

I will report on the research accomplishments during the five year tenure of ONR Grant No. N00014-86-J-3137. The grant involved activities at University of North Carolina at Greensboro, the North Carolina Supercomputing Center, the Naval Research Laboratory (at that time the Naval Oceanographic and Atmospheric Research Laboratory), and the Primary Oceanographic Prediction System at the U. S. Naval Oceanographic Office. During this time frame, the academic year (August - May) was spent at the University of North Carolina at Greensboro while the summer months (June - August) were spent at the Stennis Space Center, Bay St. Louis, MS. The goals of this research effort were the quantification of important constraints on the light field penetrating the open ocean. These constraints are the geometrical structure of the light field and the process of internal radiant emission into the light field. The geometrical structure of the light field is primarily a result of the volume scattering function of the hydrosol, but at longer wavelengths in the open ocean internal emission by Raman scattering can affect the light field geometry. The geometry, i.e. the radiance distribution of the light field, will exert a control on the amount of energy abstracted from the light field by the surrounding hydrosol and consequently the visibility characteristics of the hydrosol, its rate of heat storage, its biological productivity, etc. The mode of study was to simulate solutions of the radiative transfer equation from Monte Carlo modeling which yielded radiance distributions for geometrical study. Among the advantages of Monte Carlo modeling is the partitioning of the hydrosol volume scattering function into the volume scattering function for each of the hydrosol components -- one can ascertain the quantitative effect of a given hydrosol component on the geometry of the submarine light field. It is also possible to study separate radiation streams in the simulation which are extremely difficult or impossible to measure directly.

Grant Period 1989 - 1990

Among the tasks accomplished during this grant period was the porting of FORTRAN code for the NOARL (now NRL) optical model to the Cray Y-MP of the North Carolina Supercomputing Center, Research Triangle Park, NC. This porting resulted in about an 8 fold increase in computation speed with the concomitant increase in the accuracy of the Monte Carlo simulations employed with the NOARL optical model. This allowed more detailed investigation of spectral effects of water Raman scattering in open ocean Case 1 type waters. A key feature for predicting water Raman scattering effects is the absorption coefficient of the marine hydrosol. The most penetrating wavelengths, say 440 nm to 480 nm, are major contributors to water Raman emissions which appear at longer wavelengths in the marine hydrosol. The contribution of these wavelengths (440 - 480 nm) to the longwavelength region of

the lightfield becomes greater with depth because the absorption coefficient of the hydrosol is higher at the longer wavelengths. Relatively fewer longwavelength solar photons, then, are contributing to the light field at depth. Data from NOARL indicated a possible contribution of water Raman emission of 50% of the submarine light field at 80 m depth.

Among the results of the Monte Carlo simulations at short wavelengths was the demonstration that the apparent constancy of the irradiance ratio with depth in the blue region of the spectrum (430 - 490 nm) is likely caused by water Raman scattering. The Monte Carlo simulation of the irradiance ratios in the blue region indicated that the irradiance ratios should increase with depth. The water Raman emissions in the blue region are adding to the backscattered solar photons in the surface layers and they create an apparent constancy of the irradiance ratio with depth. The contribution of water Raman scattering declines with depth in the blue region. This fact will affect attempts to devise simple remote-sensing type algorithms which attempt the retrieval of hydrosol component concentrations based on inversion of the irradiance ratio based on backscattering activity. In the surface layers, at short wavelengths, the increment to the irradiance ratio of about 15% from water Raman emission holds steady into the longer wavelengths (500 nm+). However, the increment from water Raman scattering increases with depth at the longer wavelengths. This preliminary result from Monte Carlo modeling was in accord with the field data reported from the NOARL cruises.

Studies of the irradiance ratio at 490 nm indicated that the water Raman emission at this wavelength (source at approximately 420 nm) increased with the solar zenith angle which caused an increase in the irradiance ratio. This is explained as a result of the increased mean photon path at greater solar zenith angles and the contribution of forward scattering to the upwelling irradiant flux. However, the increased upwelling flux, both solar and water Raman emission, is not transmitted through the water/air interface. The irradiance ratio is constant with solar zenith angle. Thus the increased upwelling radiance is totally internally reflected off the water/air interface and trapped within the hydrosol.

Skylight effects were incorporated into the NOARL(NRL) optical model with a simple skylight radiance distribution model (Harrison and Coombes, 1988) and a simple model of the direct solar beam and skylight irradiance percentiles (Iqbal, 1983) from the meteorological literature. I demonstrated that adequate bracketing of the radiance distribution external to and feeding into the marine hydrosol is not achieved by a zenith sun without skylight contrasted with a totally uniform sky radiance distribution. The desired effect of this bracketing is to obtain a relatively small mean photon path with a no-skylight zenith sun and the largest possible mean photon path with an overcast sky. However, the mean photon path achieved with an air mass 2 sun and skylight exhibits a larger mean photon path than that of an overcast sky and thus achieves better bracketing of the external radiance distribution for modeling and algorithm construction.

Grant Period 1990 - 1992

During this grant period, progress was made in increasing the efficiency of the port of the NOARL optical model FORTRAN code to the Cray Y-MP at the North Carolina Supercomputing Center, Research Triangle Park, NC. In addition, the code was ported to the comparable Cray Y-MP setup at the Primary Oceanographic Prediction System of the U.S. Naval Oceanographic Office, Stennis Space Center, Bay St. Louis, MS. One improvement in the architecture of the Monte Carlo code of the NOARL optical model was optimization of the the random number generator (RNG) in the code by utilizing the RNG of the Cray Y-MP unmodified by shufflers. The improvement came about from the fact that the Cray RNG utilizes a 64-bit word in the linear congruential algorithm and this virtually eliminates the serial correlations that plague other linear congruential RNG's.

Increased efficiency of the Monte Carlo code allowed more precise estimation of the shape factor parameters for the Two-Flow Model, a popular approximation to the radiative transfer equation. The Two-Flow Model amounts to a pair of coupled differential equations that attempt to describe the fate of the upwelling and downwelling photon stream in natural hydrosols. The parameters used in these equations are the backscattering coefficient and the absorption coefficient of the hydrosol. This approximation is utilized in many remote-sensing algorithms for retrieving chlorophyll concentrations from inverted irradiance data, etc. Many simplifying assumptions are required to solve the Two-Flow Model. The backscattering coefficient must act alone and there must be no contribution to the two photon streams from forward scattering. If these assumptions are not met, the model cannot be solved or inverted. Specifically, the two parameters in the two-flow model estimated with increased precision, the downwelling shape factor r_d and the upwelling shape factor r_u, must both be equal to 1.0 if there is no contribution from forward scattering. I and my colleagues demonstrated that the down- and upwelling shape factors are neither equal to 1.0 nor to each other; therefore, the Monte Carlo model has demonstrated a significant contribution to the two photon streams from forward scattering. And the unmodified two-flow model is not solvable.

The results for the shape factors are as follows. The downwelling shape factor coefficient r_d varies from about 1.3 at zero depth to 1.5 after penetration of a few optical depths for an Air Mass of 1.0 and chlorophyll concentrations of 0.05 mg/m³ to 20.0 mg/m³. The r_d coefficient increases to 1.5 to 1.9 for Air Mass 2 and the same chlorophyll concentrations. The upwelling shape factor coefficients show an even greater variability with increase in chlorophyll concentration and increase in air mass. The r_u values for chlorophyll concentrations of 0.05 mg/m³ to 1.0 mg/m³ are from 3.0 to 4.5 for Air Masses 1 and 2. for chlorophyll concentrations of 5.0 mg/m³ to 20.0 mg/m³, the r_u values range from 5.5 to 8.0 for Air Mass 1 and 6.0 to 8.9 for Air Mass 2. The effect of increasing to Air Mass 2 is equivalent to increasing the chlorophyll concentration by a factor of 1.5 to 2.0. The bacteria concentration has a strong effect on the r_u values whereby they drop by a value of 2.0 when bacteria are removed from

the simulation. The overall effect of bacteria is to scatter much more light into the two photon streams than would be the case if scattering were just from the backscattering lobe of the volume scattering function. This occurs because the bacteria are Rayleigh-Gans scatterers and their forward scattering is much less concentrated around the forward scattering direction than is the case with larger suspended particles. The ratio r_u/r_d in these simulations ranged from 2.4 at low chlorophyll concentrations to 5.5 at high chlorophyll concentrations. The ratio of 2.4 is nearly constant for chlorophyll concentrations between 0.05 and 0.5 mg/m^3. The bacterial concentration is nearly constant at these chlorophyll levels. Increase in the solar zenith angle has a small effect on these ratios but a large effect on the separate values of r_u and r_d. Thus, the shape factor ratios are nearly constant with solar zenith angle so that the ratios will be useful in generating viable and accurate algorithms for inverting irradiances to retrieve the backscattering coefficient. Furthermore, the r_d coefficient appears to be primarily a simple function of air mass and this will allow more accurate simple algorithms to be constructed. These shape factors cause an overestimate of the backscattering coefficient, due to the forward scattering contribution to the photon streams, and they are a function of chlorophyll concentration, solar angle, and the presence or absence of bacteria. The contribution to these shape factors comes from more forward scattering going into the upwelling stream as the zenith angle increases or with an increased forward scattering function at large scattering angles from bacteria. Certainly, these optical properties delineated above are a large part of the inability of standard remote-sensing algorithms to make accurate predictions for coastal waters while their predictions appear to be adequate for open ocean waters.

More progress was made in understanding the process of water Raman scattering in open ocean waters. External irradiance conditions were shown to have a significant effect on the generation of water Raman photons. The effect of external radiance-irradiance conditions differs across the visible spectrum with 520 nm being the point where short-wavelength optical phenomena differ from long-wavelength optical phenomena. At the shorter wavelengths (<520 nm) the mean cosine of the average photon path for the submarine light field at Air Mass 1 is relatively small (approx. 0.75), implying a large mean photon path and a relatively large angular deviation of the mean photon path from the zenith. At Air Mass 2 the mean cosine becomes even smaller (approx. 0.58). Under Air Mass 2 conditions the mean photon path represents an angular deviation from the zenith of about 55 ° which is beyond the critical angle, while the angular deviation of the mean photon path under Air Mass 1 conditions represents an angular deviation of the mean photon path from the zenith of about 41 ° which is less than the critical angle. Thus, relatively more photons can escape to the air at the surface under Air Mass 1 conditions than is the case for Air Mass 2 conditions. Since the mean photon path of the light field under Air Mass 2 conditions, for shorter wavelengths, is at a greater angular deviation than the critical angle, the backscattered photons have a greater probability of encountering the water/air interface at greater than the critical angle and being totally internally reflected. This is the phenomenon of interface energy-trapping which I have described

elsewhere. Thus, for shorter wavelengths (<520 nm), the absolute number of photons from water Raman emission is greater in the surface layers for Air Mass 2 conditions than is found for Air Mass 1 conditions. However, at longer wavelengths (>520 nm), the mean photon path deviates from the zenith by an angle of 44 ° or less which is less than the critical angle so that interface energy-trapping is not occurring. The absolute number of water Raman photons generated for the longer wavelengths is not significantly greater for Air Mass 2 conditions than for Air Mass 1 conditions at the surface. These phenomena are reflected in an augmented irradiance ratio near the surface for short wavelengths and no appreciable change in the irradiance ratio near the surface for longer wavelengths. However, at depth the irradiance ratio at shorter wavelengths with water Raman emission diminishes with depth until there is no appreciable effect of water Raman emission. With an appreciable transmission of solar photons at shorter wavelengths, the photons generated from water Raman emission become a smaller fraction of the total photon flux and their effect becomes unmeasurable. At longer wavelengths, the high absorption capacity of the water molecule removes appreciable amounts of solar photons with depth and the water Raman emission comes to dominate the long wavelength light field. This is reflected in the significant increase of the irradiance ratio with depth. Nearly equal amounts of water Raman photons are being transmitted upwards and downwards which gives a high value to the irradiance ratio.

Grant Period 1992 - 1994

The study of water Raman scattering effects was extended to the entire visible spectrum under Air Mass 1 conditions for open ocean waters. There will be different effects of water Raman scattering depending on the absorption coefficient of the hydrosol for the water Raman source wavelength and the emission wavelength. The ratio of these respective absorption coefficients determines whether water Raman scattering will exert a relatively small effect on the open ocean light field or a dominant, controlling effect on the light field. The ratio of absorption coefficients of the source and emission wavelengths for the hydrosol is of even greater importance than the absolute number of water Raman emission photons produced. The lambda $^{-4}$ power law dictates that greater water Raman emission will occur for the shorter wavelengths that for the longer wavelengths. For example, the percentile contribution to the scalar irradiance at 430 nm from water Raman emission is nearly 2%. The percentile contribution from water Raman emission at 660 nm is only 0.04%. Yet the emission from water Raman scattering dominates the submarine light field at 660 nm and is almost insignificant at 430 nm. The absorption coefficient ratio for 430 nm is 0.5437 (absorption of potential source photons is greater than the absorption of solar photons at the emission wavelength) while the same ratio for 660 nm is 6.75 (absorption of potential source photons is much less than the absorption of solar photons at the emission wavelength). The decrease in the percentile contribution of water Raman photons recorded for the different wavelengths at the surface, however, did not follow

the lambda $^{-4}$ power law. The decrease in percentile contribution has a smaller slope at the shorter wavelengths (<490 nm) and a greater slope at the longer wavelengths (>490 nm) than would be the case with the lambda $^{-4}$ power law. We have another demonstration here of interface energy-trapping.

Among the ways in which the effects of water Raman scattering were demonstrated was the elucidation of the irradiance ratio (R) when water Raman scattering was ignored and when it was added in to the total photon stream. At 430 nm water Raman scattering will increase the irradiance ratio by about 1% near the surface but the effect disappears with depth. The irradiance ratio (R), calculated from the solar photon stream alone, gradually increases with depth. The irradiance ratio (R), calculated from the total photon stream (solar photons plus Raman photons) indicates an apparently constant irradiance ratio with depth. Thus the water Raman contribution in the surface layers adds enough photons to give this apparent constancy. At 490 nm the water Raman contribution to the irradiance ratio remains constant with depth, giving an increase of about 0.5 % down to the maximum optical depth obtainable with the Monte Carlo model. For 520 nm the irradiance ratio increases to about 40% after a penetration of several optical depths. This pattern continues to the longest wavelengths utilized in the study (660 nm) where the irradiance ratio approaches 1.0 after penetration of several optical depths. When one looks at the scalar irradiance values for these simulations, the value of water Raman contribution is essentially 100% after penetration of several optical depths. The irradiance ratio being less than 1.0 is a reflection of the fact that the downwelling irradiance at any depth receives the integrated water Raman emission from all points up to the surface. The upwelling irradiance, however, represents the integrated water Raman emission from all points below the reference depth, thus there are fewer available source photons to contribute to the upwelling water Raman irradiance than are available to contribute to the downwelling water Raman irradiance.

The depths of initiation of maximal water Raman emission influence on the submarine light field were determined across the visible spectrum. The depth at which the upwelling photon stream consisted of 50% water Raman photons was extrapolated to 600 m for light of 490 nm wavelength. This influence of water Raman emission would apparently not be felt for shorter wavelengths. This depth dropped to about 60 m for light of 520 nm wavelength and, as the wavelength was increased, dropped non-linearly to about 5 m for light of 660 nm wavelength. At greater depths than those just reported, the submarine light field would be dominated by water Raman scattering for the longer wavelengths.

An extensive series of comparative optical model runs, numerical solutions to the radiative transfer equation, was published during this grant period, senior author Curtis D. Mobley. The utility of seven different models, one of which was the NRL optical model, for calculating radiances and irradiances was evaluated given 7 different standardized suites of optical properties. The optical properties incorporated into the calculations ranged from highly absorbing marine hydrosols to highly scattering marine hydrosols. The errors from statistical fluctuation in the Monte Carlo outputs were generally lower for computed irradiances than for irradiances reported from field

results. The error in computed radiances was somewhat higher. The process of optical energy trapping, discussed in Stavn (1987) and Stavn et al (1984), is nicely demonstrated in Fig. 2(a) of the Mobley et al paper. It is demonstrated that in a highly scattering system, scattering to attenuation ratio (b/c) in the range of 0.8 to 0.9, the downwelling irradiance just beneath the surface is greater than in the air. Since the downwelling irradiance in the water is often approximated by taking the downwelling irradiance in air and subtracting the surface reflectance, this result can have great importance for studies of radiant energy available for diverse photochemical processes: visibility, primary productivity, photodegradation of colored organic compounds, etc. The simplified atmospheric model utilized in the NRL optical model was also demonstrated to be nearly as efficient as more complex, multilayered atmospheric models.

In keeping with the goals of investigating light field geometry in this grant, I instituted a series of studies, with my colleague Alan Weidemann of the NRL, of a remote-sensing algorithm first proposed by Zaneveld (1982). This algorithm is based on a solution to the radiative transfer equation with no simplifying assumptions but with two unknown parameters: the backscattering shape factor f_b and the forward scattering shape factor f_L. The algorithm proposed a retrieval of the backscattering coefficient b_b from knowledge of the nadir radiance and the hemispherical downwelling irradiance of a hydrosol. The original algorithm proposed that these unknown parameters be assumed equal to 1.0. It was possible to show that the assumption of a value of 1.0 for f_L is fairly robust, but that this is not the case for f_b. The reason for this is the non-isotropic nature of both the downwelling radiance field (a function of the Air Mass) and of the backscattering lobe of the hydrosol volume scattering function, the two major contributing factors to f_b. I studied the variation of f_b by Monte Carlo simulations of the radiative transfer equation utilizing known ocean optical properties of Case 1 waters and constructing solutions for the radiance and irradiance fields, given the concentration of chlorophyll. The chlorophyll concentrations varied from 0.05 mg/m^3 to 20.0 mg/m^3. This covered the range of Case 1 waters from the "blue" waters of the open ocean to the near-coastal Case 1 waters affected by nutrient upwelling but not affected significantly by minerogenic matter. From the radiance and irradiance fields generated numerically it was possible to solve the remote-sensing algorithm, retrieve the backscattering coefficient b_b, and compare it with the known backscattering coefficient that generated the the radiance-irradiance fields in the simulation. Thus I obtained both the shape factors from the complete set of light field data and the errors of estimate for the backscattering coefficient. One of the first conclusions was that the error of estimate for the retrieval of the backscattering coefficient b_b was almost totally explained by the magnitude of the backscattering shape factor f_b. Thus, any deviation of the backscattering shape factor from 1.0 was a statement of the error in the retrieved b_b. That is, an f_b of 1.50 meant an error of 50% in the estimated b_b. In addition, since the Monte Carlo simulation allows the partitioning of the volume scattering function into its separate components, water molecule, bacterial cells, algal cells, etc., it was possible to determine which hydrosol components were responsible

for the error in the retrieval of the backscattering coefficient b_b. The individual components of the hydrosol exhibited shape factors that varied outside the ranges being established for the hydrosol. For example, at this stage of the investigations, the f_b of the hydrosol varied from about 0.814 to 1.50 while the quartzlike material exhibited an f_b value of nearly 2.50 at Air Mass 1. The contribution of each hydrosol component to the f_b value of the total hydrosol was simply the component weighted by the fraction of the backscattering coefficient b_b that the hydrosol component represented. Thus, a particular component in very high concentration will have the potential of creating a shape factor and error function greatly outside the range of shape factor coefficients reported so far from the simulations of radiative transfer in the ocean.

We demonstrated a "hinge point" in the results at the chlorophyll concentration of 1 mg/m³. Apparently, at low chlorophyll concentrations which were less than the "hinge point," the properties of the water molecule and a small amount of suspended quartz-like matter were important. At chlorophyll concentrations greater than the "hinge point" the scattering properties of the algal cells began to dominate. The backscattering lobe of the model algal cells is relatively depressed at 180° off the scattering axis while the water molecule and quartzlike material are enhanced in this region of the backscattering function. The minerogenic components and the algal cells then work against each other to reduce the error of estimate as the chlorophyll concentration increases at Air Mass 1. Thus, the variation in the hydrosol backscattering shape factor f_b is 1.49 - 1.47 at chlorophyll concentrations of less than 1 mg/m³ while it drops rapidly from 1.47 to 0.99 at 20 mg/m³ for Air Mass 1. However, change in the radiance distribution, as occurs with a change in Air Mass, generates different results. The volume scattering function of the hydrosol components interacts with the different radiance distribution to change its contribution to the upwelling nadir radiance. Thus for Air Mass 2, the low chlorophyll values of f_b are 1.026 - 0.998 while increasing the chlorophyll concentration to 20.0 mg/m³ results in a drop of the f_b value to 0.814. Therefore the depressed portions of the backscattering lobe for algae cells, plus the depressed portions of the backscattering lobe of water and quartzlike material for the Air Mass 2 radiance distribution, generate much less radiant flux into the nadir radiance -- resulting in a significant underestimate of the backscattering coefficient. Bacterial cells also have an effect that varies with the radiance distribution (Air Mass). For Air Mass 1 conditions, removing bacteria from the hydrosol and replacing them with particulate organic matter decreases the backscattering shape factor for the hydrosol by 10 %. For Air Mass 2 conditions, however, removing bacterial cells from the hydrosol increases the backscattering shape factor by 10%. The important factors to consider in these errors in retrieval of the backscattering coefficient are the shape of the backscattering lobe of the volume scattering function and the shape of the radiance distribution that is interacting with the backscattering lobe of the volume scattering function. The contrast between the most active backscattering materials is a matter of the enhanced backscatter around 180° for quartz-like minerogenic material and then the reduced backscatter around 180° with enhanced backscatter around 100° for the

bacterial cells. In the open ocean, with an Air Mass of 1 and chlorophyll concentration less than 1 mg/m³ the enhanced backscatter of the quartz-like material at 180° off the scatter axis interacts directly with the radiance in the region of 0-11° off the solar axis to scatter much more radiant energy in the backward direction and into the nadir radiance than is the case with a uniform radiance distribution and a uniform backscattering lobe. The other extreme investigated in this study was that of an Air Mass 2 (solar zenith of 60°) and the backscattering lobe of bacterial cells. Under Air Mass 2 conditions the maximum in the radiance distribution (at approximately 40° deviation from the zenith) interacts with an extreme minimum in the backscattering lobe of the bacterial volume scattering function. This results in minimal contribution of the bacterial cells to the upwelling nadir radiance. Thus, the bacterial cells depress the already low backscattering shape factors by another 10%.

I made progress in the theoretical nature of the backscattering shape factor and in its estimation from actual field optical measurements. Various attempts have been made to generate relationships of the form $R = f(b_b/a)$ where $R = L_u/E_d$, the ratio of the nadir radiance to the downwelling irradiance. The Monte Carlo results that have been generated here indicate that the correlation coefficient f between the remote sensing reflectance defined with downwelling irradiance and the backscatter to absorption ratio has too much variability, that is it will not generalize from open ocean waters into coastal waters. The backscattering shape factor has the potential of being much more useful because it incorporates the shape of the volume scattering function and the vagaries of the radiance distribution into its definition. There are possibilities of making extensive enough simulations to characterize the variability of f_b for various regions of open ocean and coastal systems so that inversion algorithms will be made much more accurate. The volume scattering ratio of the volume scatter coefficient at the angular deviation of the maximum radiance to the backscatter coefficient has been shown to be an accurate estimate of f_b ranging from overcast conditions to Air Masses 1 to 2. A new era of accuracy in remote sensing algorithms may be upon us.

References

Harrison, A.W. and C.A. Coombes. 1988. Angular distribution of clear sky short wavelength radiance. Solar Energy **40**: 57-63.

Iqbal, M. 1983. An Introduction to Solar Radiation. Academic, New York.

Stavn, R. H. 1987. The three-parameter model of the submarine light field: radiant energy absorption and trapping in nepheloid layers recalculated. Journal of Geophysical Research **92**: 1934-1936.

Stavn, R.H., F. R. Schiebe, and C. L. Gallegos. 1984. Optical controls on the radiant energy dynamics of the air/water interface: the average cosine and the absorption

coefficient. Proceedings of the Society of Photo-Optical Instrumentation Engineers **489**-Ocean Optics VII: 62-67.

Zaneveld, J.R.V. 1982. Remotely sensed reflectance and its dependence on vertical structure: A theoretical derivation. Applied Optics **21**: 4146-4150.

Technical Reports

Progress Report, N00014-89-J-3137, ONR: Oceanic Optics Program Abstract Book, FY 1990.
Annual Letter Report, N00014-89-3137, February 1991.
Progress Report, N00014-89-J-3137(P00002), ONR: Oceanic Optics Program Abstract Book, FY 1991.
Annual Letter Report, N00014-89-3137(P00002), February 1992.
Progress Report, N00014-89-J-3137(P00003), ONR: Oceanic Optics Program Abstract Book, FY 1992.
Annual Letter Report, N0001-J-3137(P00003), February 1993.
Progress Report, N00014-89-J-3137(P00004), ONR: Oceanic Optics Program Abstract Book, FY 1993.
Annual Letter Report, N0001-J-3137(P00004), April 1994.
Progress Report, N00014-89-J-3137(P00005), ONR: Oceanic Optics Program Abstract Book, FY 1994.

Workshop

The NOARL optical model: assumptions and limitations. Workshop on Modeling in Oceanographic Optics. Sponsored by Naval Oceanographic and Atmospheric Research Laboratories, Long Beach, MS. March 6, 1991. (invited paper)

Publications

Stavn, R.H. 1990. Raman scattering effects at the shorter visible wavelengths in clear ocean waters. Proceedings of the Society of Photo-Optical Instrumentation Engineers **1302**-Ocean Optics X: 94-100.

Stavn, R.H. 1992. External factors and water Raman scattering in clear ocean waters: skylight, solar angle, and the air/water interface. Proceedings of the Society of Photo-Optical Instrumentation Engineers **1750**-Ocean Optics XI: 138-148.

* Stavn, R. H. and A. D. Weidemann. 1992. Raman scattering in ocean optics: quantitative assessment of internal radiant emission. Applied Optics, **31**: 1294-1303.

Stavn, R. H. 1993. The effects of Raman scattering across the visible spectrum in clear ocean water: a Monte Carlo study. Applied Optics **32**: 6853-6863.

Mobley, C. D., Gentili, B., Gordon, H. R., Jin, Z., Kattawar, G. W., Morel, A., Reinersman, P., Stamnes, K., and Stavn, R. H. 1993. Comparison of numerical models for computing underwater light fields. Applied Optics **32**: 7484-7504.

Stavn, R.H. and A. D. Weidemann. 1994. Geometrical light field parameters for improving remote sensing estimates of the backscattering coefficient for the marine hydrosol. Proceedings of the Society of Photo-Optical Instrumentation Engineers **2258**-Ocean Optics XII: 202-209.

Weidemann, A.D., Stavn, R.H., Zaneveld, J.R.V. and M. R. Wilcox. 1995. Error in predicting hydrosol backscattering from remotely sensed reflectance. Journal of Geophysical Research **100: 13,163-13,177.

Selected for inclusion in Frank M. Caimi (ed). Selected Papers on Underwater Optics. Milestone Series of SPIE Optical Engineering Press.

**Recipient of the Alan Berman Research Publications Award, Department of the Navy, Naval Research Laboratory.*

INITIAL DISTRIBUTION LIST

ADDRESSEES	NUMBER OF COPIES
1. Dr. Steven Ackleson Office of Naval Research Code 322 800 North Quincy Street Arlington, VA 22217-5660	3
2. Administrative Contracting Officer Office of Naval Research Resident Representative N66009 Austin, TX 78701	1
3. Director, Naval Research Laboratory Attn: Code 2627 Washington, DC 20375	1
4. Defense Technical Information Center 8725 John J. Kingman Road, Suite 0944 Ft. Belvoir, VA 22060-6218	2

Reprinted from

Ocean Optics X

16–18 April 1990
Orlando, Florida

SPIE

P

Volume 1302

Raman scattering effects at the shorter visible wavelengths in clear ocean waters

Robert Hans Stavn

University of North Carolina/Greensboro, Department of Biology
Greensboro, NC 27412

ABSTRACT

The limits and nature of the influence of water Raman scattering in clear ocean waters are the subject of continuing investigations. At shorter wavelengths (less than 500 nm) the in-water effects of water Raman scattering are confined to the near surface layers while the water leaving irradiance is significantly augmented by Raman emission. The water leaving Raman irradiance is apparently affected by the Fraunhofer lines of the solar spectrum.

2. INTRODUCTION

The purpose of this report is to extend our knowledge of the limits of the water Raman scattering effects in clear ocean waters. This phenomenon is an inelastic transpectral scattering of photons due to thermal vibration and rotation of the water molecule. One of the most important modes, the one investigated in this report, is the OH-stretch vibration of the water molecule. It is expressed as an inelastic scattering of a photon by the water molecule which abstracts energy from the photon and scatters it at a longer wavelength when acting in a Stokesian fashion. The amount of the wavelength shift is controlled by a constant frequency shift associated with the water-photon interaction. Anti-Stokesian interactions are also possible but not quantitatively significant under oceanic conditions. Water Raman scattering was demonstrated to be significant in the long wavelength green-yellow region of the visible spectrum (520 - 589 nm) by Stavn and Weidemann[1,2] and confirmed by Marshall and Smith[3] with an alternate formulation. The results reported here demonstrate the nature of the effects of water Raman emission at the shorter visible wavelengths. It is worthwhile to investigate these processes at the shorter wavelengths because Raman emission increases in intensity with decrease in wavelength. This is due to the λ^{-4} relation.

3. METHODS

The NOARL optical model was used in this investigation, a Monte Carlo simulation of the radiative transfer equation that includes water Raman scattering. The coefficients employed in this investigation are those of the NOARL Blue Water Model[1,2]. The coefficients of the model are those published by Morel[4], Smith and Baker[5], Chang and Young[6], Kullenberg[7], and Gordon et al[8]. Three source wavelengths are used to generate the water Raman emission at a given emission wavelength; this allows an accurate assessment of the effect of a spectrally varying input of solar irradiance on the generation of emission at a particular wavelength. At shorter wavelengths the atmospheric input is significant so that atmospheric routines have been added to NOARL model. The skylight radiance distribution model of Harrison and Coombes[9] is incorporated into the subroutines by which a photon enters the model ocean. The determination of the percentage of entering irradiance from the solar beam and from the sky is calculated from the model of Iqbal[10]. The parameters for a marine aerosol were those employed by Baker and Frouin[11]. The extraterrestrial solar spectrum propagated through the model atmosphere was that reported by Iqbal[10]. Comparisons are made predominantly at air mass 1 with the solar zenith angle of 11°, while some comparisons will be made at air mass 2.

Briefly, the model works by first determining whether a photon enters the water from the solar beam or from the sky dome by probabilities calculated from Iqbal's model and chosen for a given photon by a random number generator. The angle of entry of the photon is then determined from the radiance distribution of Harrison and Coombes for the sky radiance with the angle chosen by the random number generator. Fresnel relations determine whether the photon enters the water or is reflected. The surface of the model ocean is assumed to be flat. Upon entry into the water the photon either scatters or is absorbed depending on probabilities calculated from the absorption and scattering coefficients for the model ocean and the event is chosen by the random number generator. If a photon is absorbed a new one is generated from the solar beam or the sky dome. If a scattering event occurs, the probability of whether it is elastic or inelastic is determined from the respective scattering coefficients and the random number generator. An inelastic scattering transmits the photon to a new set of routines including inherent optical coefficients at the shifted

---

Optical Oceanography Program, NOARL

wavelength. Second order inelastic scattering is not considered. If the event is an elastic scattering, the probability of whether it is from a water molecule or a quartz particle is determined from their scattering coefficients and the random number generator. The trajectory of the photon is determined by the random number generator from the volume scattering function of the particle in question. Duplicate runs of the model are made for each condition of parameters tested and there are 2.5×10^6 photons per run.

The output of the Monte Carlo simulation is in zonal radiances which are summed to give downwelling and upwelling irradiances and scalar irradiances. This information was used to determine the irradiance ratios in air and at depth intervals of 5 meters. The irradiance ratio is defined by

$$R = \frac{E_u}{E_d} , \tag{1}$$

where E_u is the upwelling irradiance and E_d is the downwelling irradiance. The ratio in air is expressed as the emergent irradiance of the water ratioed with the downwelling irradiance from sun and sky and the specular reflectance of the atmospheric photons from the air/water interface is ignored. An assessment of the effect of water Raman photons on the optical parameters determined from the measured irradiances, including penetrating solar photons and transpectrally scattered photons from the water molecule, is achieved by calculating the absorption coefficient from the total irradiances. The basis for this calculation is Gershun's equation[12]

$$\frac{dE_z}{dz} = - a (E_o + E_o^*) , \tag{2}$$

where the original formulation is modified by the presence of water Raman photons in the scalar irradiance term E_o^* added to the scalar irradiance E_o due to solar photons. E_z is the net downwelling irradiance (downwelling irradiance - upwelling irradiance) and z is the geometric depth in meters. The effect of water Raman photons on the net downwelling irradiance is very small because of the nearly uniform emission of water Raman photons and is not delineated in the equation. It is solved with the Three Parameter Model of the submarine light field[1]

$$a = \frac{\ln[E_z(z_2)] - \ln[E_z(z_1)]}{\int_{z_1}^{z_2} \frac{1}{\bar{\mu}(z)} dz} , \tag{3}$$

where $\bar{\mu}(z)$ is the mean cosine of the average photon path of the light field at depth z, the ratio of the net downwelling irradiance and the scalar irradiance. It can be seen readily from Eq. (2) that a significant effect of the quantitative emission of water Raman photons is a decrease in the calculated absorption coefficient of the light field determined from the measured irradiances.

4. RESULTS

The Monte Carlo output for upwelling irradiance is presented for three selected wavelengths in Fig. 1. The logarithmic values of E_u are plotted with depth and we see a tendency for an increase in water Raman photons at the surface with decrease in wavelength. However, the percentile of upwelling photons tends to remain the same over the wavelengths or to decrease in percentile as the absorption coefficient of the water decreases, and more solar photons are masking the water Raman photons. The absorption of the water molecule is much higher at 520 nm than at the shorter wavelengths and the upwelling irradiance becomes dominated by water Raman emission at a little over 40 m depth. At 490 nm the rate of decay of the water Raman photons produced

is equivalent to the rate of decay of solar photons and the Raman emission makes a small contribution to the field at all depths. At 440 nm the rate of decay of the water Raman photons produced is greater than the rate of decay of solar photons and they become an insignificant portion of the total photon flux at about 80 m.
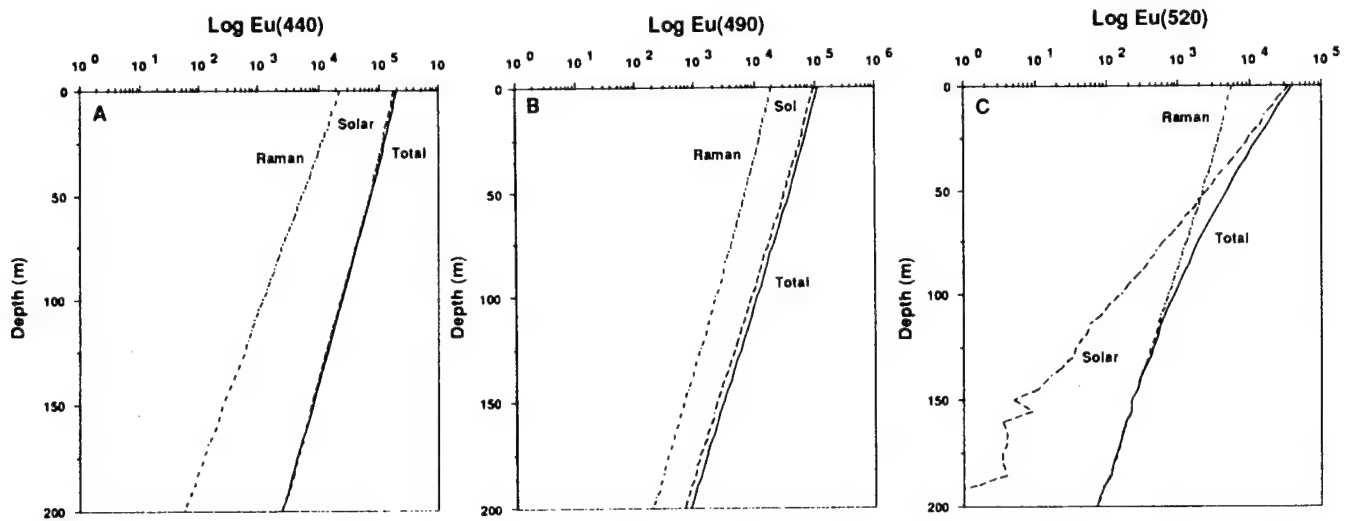

Figure 1. Upwelling Irradiances from three selected wavelengths. Each wavelength normalized to 2.5 x 10^{6} solar photons, Air Mass 1. A) Wavelength 440 nm. B) Wavelength 490 nm. C) Wavelength 520 nm.

The effect of water Raman emission on the total light field is most readily assessed by calculating the absorption coefficient of the hydrosol from the Monte Carlo output and comparing it with the actual absorption coefficient of the hydrosol. We see in Fig. 2 that the calculated absorption coefficient for 520 nm deviates from the actual by 1% at the surface and the deviations increase as the water Raman photons dominate the light field at depth. For the calculation at 490 nm the absorption coefficient deviates
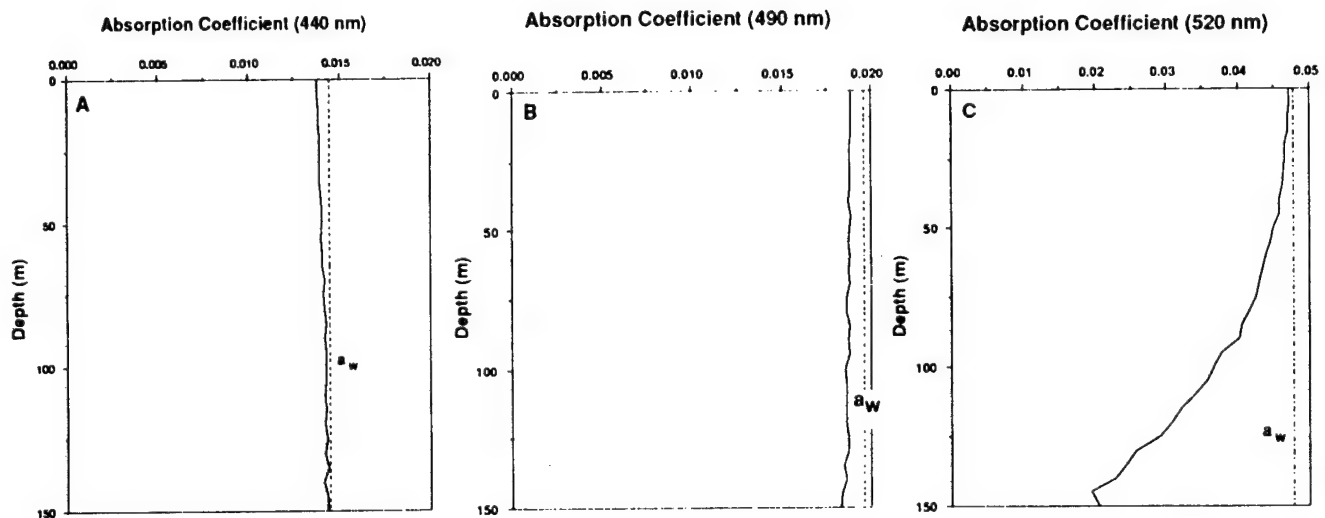

Figure 2. Absorption coefficients calculated from Eq. (3) compared with true absorption coefficient of model. A) Wavelength 440 nm. B) Wavelength 490 nm. C) Wavelength 520 nm.

from the true absorption coefficient by about 4% at the surface and the deviation is nearly constant with depth. By contrast, the calculated absorption coefficient deviates by 6% at 440 nm in the surface layers and the deviations decrease with depth, becoming inconsequential at about 80 m.

The in-water irradiance ratios are illustrated in Fig. 3. The ratio for 520 nm shows an increase of the total photon ratio over the relatively constant ratio for solar photons. At the point where the water Raman photons begin to dominate the upwelling
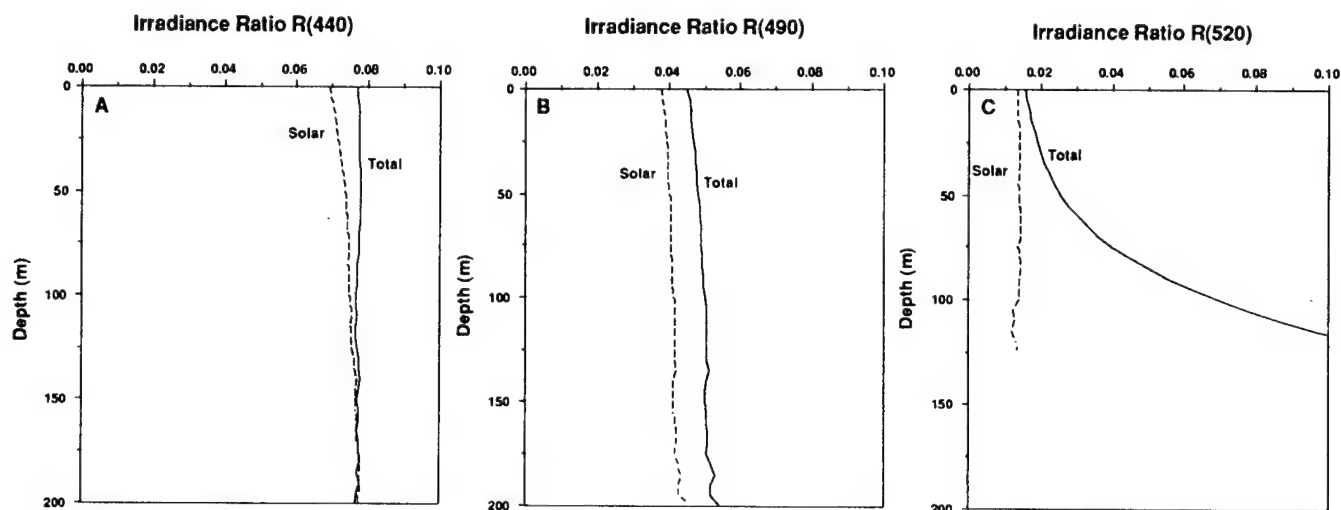

Figure 3. In-water irradiance ratios from three selected wavelengths. A) Wavelength 440 nm.
B) Wavelength 490 nm. C) Wavelength 520 nm.

irradiance field at 40 m the ratio increases dramatically. At 490 nm the irradiance ratio for solar photons shows a tendency to increase with depth and the addition of Raman photons gives a relatively constant augmentation with depth. For the system at 440 nm the solar photons show an increase of R with depth but the addition of Raman photons causes an R ratio nearly constant with depth, the increase is about 10% at the surface with the Raman contribution consistently decreasing with depth.

The irradiant fluxes emerging into the air are treated in Fig. 4. Of the upwelling irradiance contribution to the R ratio at
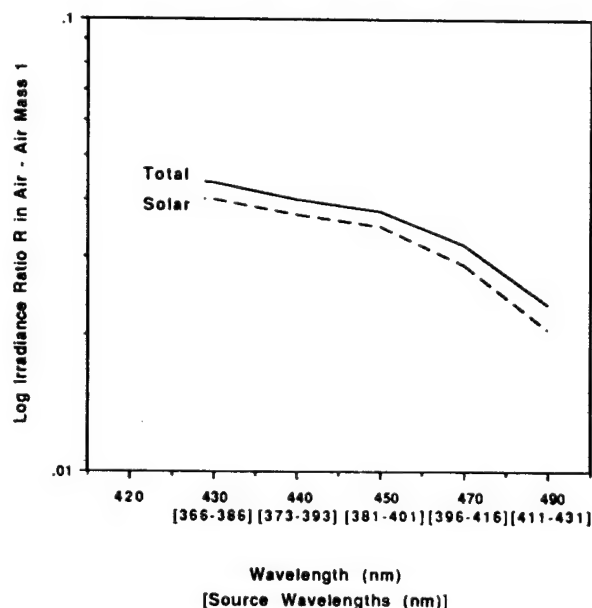

Figure 4. Irradiance ratios in air for solar photons and solar photons augmented by Raman scattering.

490 nm, 12% comes from upwelling water Raman photons. The percentage is 10% at 470 nm and drops to 7% at 440 nm. The percentage of the Raman contribution increases from here to 8% at 430 nm.

A comparison of irradiance ratios for air mass 1 and air mass 2 in air and water at 490 nm is presented in Fig. 5. An increase
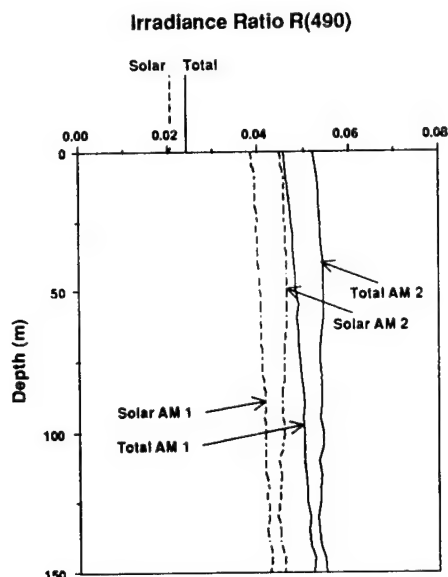
Irradiance Ratio R(490)

Figure 5. Irradiance ratios in air and water at 490 nm for Air Mass 1 and Air Mass 2.

in R values for solar photons and total photons for the in-water values is noted with the increase in the skylight component and the solar zenith angle. However, the R values in air for the water leaving irradiance remain constant.

5. DISCUSSION

At longer wavelengths (500 nm +) the in-water optical properties in clear ocean waters are significantly affected by water Raman scattering[1-3,13]. There are also significant effects from this transpectral scattering phenomenon at the wavelengths less than 500 nm. This activity appears consistently in the surface layers of clear ocean waters.

The demonstrated effects of water Raman scattering differ in the long and short wavelength regions of the electro magnetic spectrum primarily because of the absorption properties of the water molecule. At longer wavelengths (500 nm +) the absorption coefficient of the water molecule for the emission wavelength is greater than that for the source wavelength. Solar flux is relatively rapidly absorbed at the emission wavelengths. At shorter wavelengths the absorption coefficients of the water molecule for both source and emission wavelengths are about equal. Therefore, although the absolute production of Raman photons is greater as the source wavelength decreases, the number of solar photons at the emission wavelength is increasing too. Thus at longer wavelengths the effects of water Raman emission are detectable in the surface layers and increase with depth until the deepest light field is dominated by transpectral scattering. At shorter wavelengths the effects of water Raman scattering are important in the surface layers and become less significant with depth.

The evidence for water Raman effects comes from various aspects of the output of the NOARL optical model. The absolute increase of Raman photons with decrease in wavelength is demonstrated in Fig. 2. Near the air/water interface, the percentile deviation of the calculated absorption coefficient [Eq. (3)] from the true absorption coefficient increases as the emission wavelength decreases. For emission wavelengths less than 430 nm the potential solar flux to generate water Raman photons decreases and this relationship may no longer hold. Water Raman scattering is emitted nearly uniformly which means that although its contribution to the downwelling irradiance is small it can make a significant contribution to the upwelling irradiance as shown in Fig. 3. The upwelling portion of the water Raman emission thus affects both the in-water irradiance ratio and the irradiance ratio in the air (Fig. 4). Multiple scattering of the incoming solar flux at shorter wavelengths creates an increase in the R ratio with depth as the plots of R due to solar photons indicate (Fig. 3) while the water Raman contribution in the upper layers tends to make the

R ratio for the total photon flux nearly constant. Thus the apparent constancy of the R ratio reported by some in this wavelength region for clear ocean waters can be explained by the water Raman emission activity. The water leaving upwelling irradiance, which contributes to the signal detected by remote sensing, is augmented from 7% to 12% by water Raman scattering with a flat ocean surface. Within the range of emission wavelengths investigated, the decrease in this augmentation at 440 nm and 450 nm can be explained by the presence of Fraunhofer lines at 385-395 nm in the extraterrestrial solar irradiance acting as the source for water Raman emission. The water leaving irradiance signal (Fig. 5), at least at 490 nm, is constant with the change in solar zenith angle and percentage of skylight irradiance accompanying a change in the air mass. However the in-water irradiance ratio increases, both for solar photons and for Raman photons, with an increase in air mass. The extra upwelling flux is apparently reflecting off the air/water interface at angles greater than the critical angle and represents interface energy trapping as reported earlier[14]. The relative increase in water Raman emission with increase in air mass is due to the greater average photon path under these conditions; this allows an interaction of the incoming irradiance with more water molecules.

6. SUMMARY

1. Water Raman scattering is a significant factor for the optical properties of clear oceans in the short wavelength region (< 500 nm).

2. This transpectral scattering affects the surface layers of clear oceans and the water leaving irradiance.

3. The apparently constant R value for short wavelengths in clear oceans may be caused by water Raman scattering.

4. The Raman component of water leaving irradiance varies from 8% at 430 nm to 12% at 490 nm. A decrease to 7% in the 440 - 450 nm region is caused by Fraunhofer lines in the extraterrestrial solar spectrum.

7. ACKNOWLEDGMENTS

8. REFERENCES

1. R. H. Stavn and A. D. Weidemann, "Raman scattering effects in ocean optics," in Ocean Optics IX (M. A. Blizard, ed.), SPIE Proceedings, Vol. 925, 131-139 (1988).

2. R. H. Stavn and A. D. Weidemann, "Ocean optical modeling: Raman scattering effects," Appl. Opt., 27(19), 4002-4011 (1988).

3. B. R. Marshall and R. C. Smith, "Raman scattering and in-water ocean optical properties," Appl. Opt., 29(1), 71-84 (1990).

4. A. Morel,"Optical properties of pure water and pure sea water," in Optical Aspects of Oceanography (N. G. Jerlov and E. Steemann Nielsen, eds.), 1-24, Academic Press, London (1974).

5. R. C. Smith and K. S. Baker, "Optical properties of the clearest natural waters," Appl. Opt., 20(2), 177-184(1981).

6. C. H. Chang and L. A. Young, "Seawater temperature measurement from Raman spectra," Research Note 920, sponsored by Advanced Research Projects Agency, ARPA Order No. 1911, 1-59 (1972).

7. G. Kullenberg, "Scattering of light by Sargasso sea water. Deep-Sea Res. 15(4), 423-432 (1968).

8. H. R. Gordon, O. B. Brown, and M. M. Jacobs, "Computed relationships between the inherent and apparent optical properties of a flat homogeneous ocean," Appl. Opt. 14(2), 417-427 (1975).

9. A. W. Harrison and C. A. Coombes, "Angular distribution of clear sky short wavelength radiance," Solar Energy, 40(1), 57-63 (1988).

10. M. Iqbal, An Introduction to Solar Radiation, Academic Press, New York (1983).

11. K. S. Baker and R. Frouin, "Relation between photosynthetically available radiation and total insolation at the ocean surface under clear skies," Limnol. Oceanogr., 32(6), 1370-1377 (1988).

12. A. Gershun, "The light field," J. Math. Phys., 18, 51-151 (1939).

13. S. Sugihara, M. Kishino, and M. Okami, "Contribution of Raman scattering to upward irradiance in the sea," J. Oceanogr. Soc. Japan, 40, 397-404 (1984).

14. R. H. Stavn, F. R. Schiebe, and C. L. Gallegos, "Optical controls on the radiant energy dynamics of the air/water interface: the average cosine and the absorption coefficient," in Ocean Optics VII (M. A. Blizard, ed.), SPIE Proceedings, Vol. 489, 62-67 (1984).

Reprinted from

Ocean Optics XI

20–22 July 1992
San Diego, California

External factors and water raman scattering in clear ocean waters: skylight, solar angle, and the air/water interface

Robert Hans Stavn

Department of Biology
University of North Carolina at Greensboro
Greensboro, NC 27412

ABSTRACT

Water Raman scattering is influenced by the optical factors external to the clear marine hydrosol or bounding it (the air/water interface). At shorter wavelengths (< 490 nm) detectable water Raman scattering is confined to the near surface layers, where an increase in solar zenith angle increases the water Raman emission. Among the effects of water Raman scattering is an increase in the irradiance ratio (reflectance) of the surface layers. Skylight tends to lessen the production of water Raman scattering by a few percent at shorter wavelengths. At longer wavelengths (> 500 nm) the surface effects disappear as hydrosol absorption becomes the dominant factor. However, at depth large solar zenith angles cause "shoaling" of Raman production, i.e. water Raman scattering effects occur closer to the surface layers than is the case for smaller zenith angles. The water leaving irradiance, significantly affected by Raman emission in clear ocean waters, changes little or not at all with solar zenith angle.

2. INTRODUCTION

Water Raman scattering in clear ocean waters is receiving more attention from many investigators. This phenomenon is an inelastic transpectral scattering of photons caused by thermal vibration and rotation of the water molecule. The OH stretch vibration of the water molecule is one of the most important modes. It is expressed as an inelastic scattering of a photon by the water molecule which abstracts energy from the photon and scatters it at a longer wavelength when acting in a Stokesian fashion. The amount of the wavelength shift varies with the wavelength of the interaction and is controlled by a constant frequency shift associated with the water-photon interaction. Anti-Stokesian interactions are also possible but not quantitatively significant at ambient oceanic temperatures. This phenomenon causes an internal emission of photons at all wavelengths of the oceanic light field and this alters certain measured irradiances in clear ocean water. Studies of the effects of inelastic scattering on specified irradiances in 10 nm or similar bandwidths have been conducted by many[1-6].The approach taken here is the application of Monte Carlo modeling to determine optical properties that are difficult or nearly impossible to measure directly, and comparing the Monte Carlo output with directly measured optical properties when feasible. The predictions from the NOARL optical model have been confirmed by direct optical measurements from NOARL (now NRL) cruises and Biowatt cruises. These observations have been concentrated in the mid-visible spectrum. At the shortwave visible and UV end of the spectrum, however, the direct observations have been lacking, although many are rectifying this situation at this moment due to concerns about the effects of ozone depletion. Thus a primarily Monte Carlo approach is required at this time while awaiting direct observations to confirm the predictions.

Water Raman scattering is detectable close to the air/water interface at short wavelengths, and at depth, away from the surface layers, at longer wavelengths[5,6]. In this report we show that the variations in the light field external to the hydrosol can affect the generation of water Raman photons. Skylight represents as much as 50% of the incoming irradiance at or near the UV and shorter visible (blue) wavelengths, with a zenith sun. Also, the absolute production of water Raman emission increases with a decrease in wavelength from the λ^4 relation. Thus skylight has the potential for a significant effect on the stimulation (emission) of water Raman photons. Another significant external factor is the solar zenith angle. This will affect the mean photon path of the submarine light field and therefore the number of potential encounters of photons with water molecules. An increase in photon-water interactions will mean an increase in the production of water Raman photons. Therefore, our basic question is what is the role played by skylight, solar angle, and associated factors external to marine hydrosol in the genesis of Raman scattering in clear ocean waters?

3. METHODS

We utilize the NOARL optical model, a Monte Carlo simulation of the radiative transfer equation. The NOARL Blue Water Model of this report represents a simulation of photon penetration into a nearly "pure" ocean with no suspended particulates. This model utilizes the optical coefficients of the water molecule for: absorption, elastic scattering, inelastic Raman scattering, and depolarization of the water Raman emission[3,4,7-11]. The longer wavelength photons from water Raman scattering are emitted in a broad emission band (about 18 nm at 400 nm and and about 43 nm at 600 nm). Thus for a given waveband of interest, a fairly broad band of source wavelengths can contribute Raman emissions to it. The water Raman scattering coefficient is thus divided into three parts and each part represents the contribution of a particular source waveband of 10 nm bandwidth to the Raman emission. This allows the accurate assessment of how differentially absorbing materials may affect Raman photon production and the water leaving irradiance. In addition, the three different source wavebands feeding water Raman photons into an emission waveband then allow us to account for the effects of depolarization on the Raman scattering coefficient and on the volume scattering function for Raman scattering[3]. A more pronounced depolarization of the water Raman emissions yields greater isotropy (approaching a spherical shape) of the volume scattering function for Raman scattering.

The other component of the NOARL Blue Water model represents the optical coefficients of quartz-like material which are fashioned from the Petzold AUTEC (Tongue of the Ocean) volume scattering data corrected for molecular water and Kullenberg's estimate of the quartz-like scattering coefficient for clear ocean water[12,13].

The atmospheric parameters of the NOARL optical model are modeled as follows. The extraterrestrial solar spectrum of Iqbal[14] is used. These irradiances are transmitted through an atmosphere conforming to the model of Brine and Iqbal[15] and utilizing its parameters and approximations. For each simulation run a stream of solar photons is generated at the given wavelength, and three source wavelengths contribute to the Raman emission of that wavelength. All photon streams are generated by transmission of solar photons of the emission wavelength and solar photons of the source wavelengths through the model atmosphere to the sea surface. The radiances coming from the sky dome and entering the hydrosol vary due to changes in solar position. This variation in the sky radiances is modeled from the distribution of

Harrison and Coombes[16]. The maximal skylight irradiation comes from near the bearing of the solar beam, thus the probable effect of skylight is not immediately obvious. The marine aerosol in the model atmosphere was modeled from the parameters employed by Baker and Frouin[17]. Comparisons are made at air mass 1 with a solar zenith angle of 11° and at air mass 2 or a solar zenith angle of 60°.

Briefly, the model works by first determining whether a photon enters the water from the solar beam or from the sky dome. The probabilities are calculated from Brine and Iqbal[15] and chosen for a given photon by a random number generator. The angle of entry of the photon is also chosen by the random number generator from the sky radiance distribution of Harrison and Coombes[16]. Fresnel relations determine whether the photon enters the water or is reflected from the surface of the flat model ocean. Upon entry into the water the photon is either scattered or absorbed depending on probabilities calculated from the absorption and scattering coefficients for the model ocean. These coefficients are used to determine the probability of the event and the random number generator chooses which one. When a photon is finally absorbed a new one is generated from either the solar beam or the sky dome. For a scattering event the probability of whether it is elastic or inelastic is determined from the respective scattering coefficients and the random number generator. After an inelastic scattering event, the wavelength shifted photon is controlled by the probabilities determined from the inherent optical coefficients at the shifted wavelength. Second order inelastic scattering is not considered. After an elastic scattering event, the probability of whether the scattering event is an encounter with a water molecule or a quartz particle is determined from their respective scattering coefficients and the random number generator. The new trajectory of the photon is determined by the random number generator from the volume scattering function of the particle in question. Duplicate runs of the model are made for each condition of parameters tested: there are 1×10^7 photons per run.

The output of the Monte Carlo simulation is in zonal radiances which are summed to give downwelling and upwelling irradiances and scalar irradiances. From this information we calculate the irradiance ratios in air and at regular depth intervals of 1 – 5 meters, depending on the wavelength of the simulation. The irradiance ratio is defined by

$$
R \; = \; \frac{E_u}{E_d} \quad , \tag{1}
$$

where E_u is the upwelling irradiance and E_d is the downwelling irradiance. The ratio in air is expressed as the emergent upwelling irradiance of the water ratioed with the downwelling irradiance from sun and sky and the specular reflectance of the atmospheric photons from the air/water interface is ignored. We are also investigating the effect of differing mean photon paths of the submarine light field on water Raman photon production, the inverse of the mean photon path per meter being the average cosine of the mean photon path defined by

$$
\bar{\mu} \; = \; \frac{E_z}{E_o} \quad , \tag{2}
$$

where E_z is the net downwelling irradiance and E_o is the scalar irradiance. Two separate photon streams are generated in the Monte Carlo output and they can be combined in any convenient fashion. Usually the total photon stream can be compared with the solar photon stream stream in the figures with the difference being the Raman photon stream.

4. RESULTS

The major optical comparisons that are made in-water for this report occur at 430, 490, and 550 nm. These wavelengths are enough to document the major processes taking place. Other wavelengths will be invoked, as they are available, in various figures and tables of data. At air mass 1 the results did not differ when comparing simulations with skylight and without skylight. Therefore, only data from air mass 1 with skylight will be presented and compared with the air mass 2 simulations.

This report is concerned with determining the possible conditions external to the clear ocean hydrosol that might affect the production of photons from water Raman scattering. Accordingly, the occurrence of Raman photons in the scalar irradiance at zero depth was chosen as a workable single index of photon production by water Raman scattering for comparison between various modes of the external light field. The scalar irradiance of Raman photons at zero depth integrates the upwelling Raman photon stream from most depths below the surface where significant Raman activity is taking place. This variable also integrates the downwelling Raman photon stream at the surface where there exist the maximum number of potential source photons to be converted into Raman photons. In Table 1 we have the Monte Carlo output for spectral scalar Raman photons at the surface.

Table 1. Spectral Scalar Raman Photon Production. Normalized to 10^7 photons per Wavelength. Water/Air Interface.

Emission Wavelength (nm)	Solar-Sky Conditions		
	Air Mass 1:Sky	Air Mass 2:Sky	Air Mass 2:No Sky
430	173,343	232,010	234,424
440	137,118	186,564	186,005
470	143,857	207,120	207,514
490	117,959	128,105	152,103
520	52,374	52,718	53,552
550	33,533	32,502	31,308
640	4,079	3,667	3,678

There is a break point in Table 1 when comparing the Raman photon production at different air masses. In the range 430 nm - 490 nm the production of Raman photons under Air Mass 2 conditions exceeds the Raman production under air mass 1 conditions by anywhere from 19% to 44%. In the region 520 nm - 640 nm the production of Raman photons under air mass 2 conditions does not exceed the production of Raman photons under air mass 1 conditions and might even be less. In the same ranges, possible

effects of skylight can be seen in the short wavelength region while such effects appear to not be discernible in the longwave region.

Since the production of water Raman photons is a function of the probability of encounter of a photon with a water molecule, the mean cosine for the light field serving as a potential source of Raman photons is investigated at zero depth as with the scalar Raman photons. Of the three wavebands serving as a source for Raman photons, the middle band was chosen to illustrate the mean cosine of the light field serving as a source of Raman photons as seen in Table 2.

Table 2. Spectral Mean Cosines at Surface: Mid-Band of Raman Source Wavelengths.

Wavelength		Solar-Sky Conditions		
Source (nm)	**Emission (nm)**	Air Mass 1:Sky	Air Mass 2:Sky	Air Mass 2:No Sky
375.8	**430**	0.7636	0.5966	0.5827
420.8	**490**	0.7491	0.5796	0.5679
464.3	**550**	0.8075	0.6202	0.6088
526.8	**640**	0.9363	0.7183	0.7055

We see a pattern here somewhat similar to that of Table 1. The mean cosine of the source light fields is relatively small for the Raman emission wavelengths less than 490 nm while it is larger for longer Raman emission wavelengths (520 nm +). In addition, the mean cosine is slightly larger for the air mass 2 simulations with skylight than for the simulations without skylight.

Among the optical properties of the submarine light field that can be affected by water Raman scattering are the in-water R values shown in Figs. 1, 2, and 3. In the short wavelength region (< 490 nm) the R values can be seen to increase with increasing solar zenith angle (air mass) near the surface. At 430 nm (Fig. 1), in the surface layers, there is a significant increase of R, both solar and total, at air mass 2 over the value at air mass 1. The increase in R due to increased Raman emission at air mass 2 is visible and there is a slight effect of skylight: a decrease in R from Raman emission of about 1.0%. At 490 nm (Fig. 2), the increase in R in the surface layers due to Raman emission is nearly constant with depth. The increase in R at air mass 2 due to Raman scattering is evident while a 2% decrease in R with skylight present is also evident. At depth the tendency is for the R values at the two different air masses to come together and for the differences between them to be eliminated. The trends for the R values of wavelengths greater than 500 nm are in sharp contrast to those mentioned for the shorter wavelengths. These trends are illustrated in Fig. 3 for 550 nm. There is no increase in the R value due to increased Raman scattering in the surface layers at air mass 2 for the values at 550 nm (Fig. 3A). However, with increasing distance from the surface layers, the

production of Raman photons at air mass 2 becomes quite evident (Fig. 3A,B). In this case the R values diverge increasingly with depth rather than tending to converge.

There are also plots in Figs. 1, 2, and 3 that indicate the R value calculated by ratioing the upwelling flux emerging into the air with the downwelling flux in the air at the water surface. We see that the R values in air change very little or not at all with a change in air mass in contrast with the in-water values.

5. DISCUSSION AND CONCLUSIONS

An Increase in the solar zenith angle in clear ocean waters results in an increase of the water Raman emission in the surface layers at shorter wavelengths (< 490 nm) as seen in Table 1. This effect disappears for longer wavelengths (> 500 nm). An increase in the solar zenith angle increases the mean photon path per meter which could account for part of this effect. We also see the increase of Raman photon production with decrease in wavelength (Table 1) as is predictable from the λ^{-4} relation. This relationship does not hold at 440 nm because the potential source photons of the solar irradiance are lessened by being located in contiguous Fraunhofer lines[5,6]. The increase in mean photon path cannot explain the increase in Raman photon production because the effect does not appear at longer wavelengths. The process of interface energy trapping[18] can explain the increase in Raman photon production however. At longer wavelengths the mean cosine increases relative to the mean cosine at shorter wavelengths (Table 2). At 640 nm the mean cosine approaches the cosine of the refracted solar beam. Thus this smaller mean photon path implies diminished multiple scattering and fewer multiple interreflections of the Raman emissions from the water/air interface. This happens because at longer wavelengths (> 520 nm) the absorption coefficient of the marine hydrosol becomes much greater than the single scattering coefficient and tends to suppress multiple scattering. Thus the small mean cosine at the shorter wavelengths indicates a greatly augmented mean photon path, more chances for collisions of photons with water molecules, and greater production of photons by water Raman scattering.

Although the augmentation of water Raman scattering with increasing zenith angle does not occur near the surface at longer wavelengths (> 500 nm), there is significant activity at greater depths (Fig. 3A,B). The irradiance ratio at 550 nm (Fig. 3A,B) is not augmented at air mass 2 by increased numbers of water Raman photons near the surface and air/water interface. However, with increase of depth, the R ratio for air mass 2 increases over that of air mass 1, indicating not so much greater production of water Raman photons at shallower depths relative to air mass 1 but rather the earlier removal of solar photons at shallower depths due to the increased mean photon path per meter. With a smaller mean cosine value, as under air mass 1 conditions, the solar photons are driven deeper into the hydrosol and will mask the production of water Raman photons at greater depths.

We have seen so far the effects of increasing solar zenith angle on the in-water R value which increases significantly with zenith angle and with increase in Raman photon production. However, in Figs. 1, 2, and 3 there are plots of the extremes of the R values in air recorded for the external conditions that are affecting the in-water values of R. The R values in air do not vary nearly as much as the values in water. The radiances contributing to the increased in-water values of R are apparently encountering the water/air interface outside the critical angle for the most part. The increased Raman emission and backscatter of solar photons at greater solar angles is not transmitted across the water/air interface and the phenomenon may

be difficult to detect directly by remote sensing. This is another aspect of the interface energy trapping mentioned earlier[18]. The importance of the water/air interface for the optical dynamics discussed in this report indicates that the next step in these studies is to investigate the wave-roughened interface.

Skylight per se has a weak effect on the generation of water Raman photons in the surface layers; there is, however, a slightly larger in-water mean cosine for skylight and therefore smaller mean photon path per meter under air mass 2 conditions. For air mass 1 conditions the effects of skylight are not discernible with the routinely measured irradiances and thus these data are not presented. The smaller mean cosine implies potential Raman source photons are transported to greater depths and thus generate fewer Raman photons near the surface layers. This effect can be seen a little for the shorter wavelengths (< 500 nm) where the R coefficient decreases by a maximum of 2% near the surface layers (Fig. 2) for simulations with skylight at air mass 2 compared with simulations lacking skylight. These effects disappear at longer wavelengths. Small skylight effects can be seen at shorter wavelengths (< 490 nm) but not at longer wavelengths.

6. SUMMARY

1. Increase in the solar zenith angle has the strongest effect on stimulating water Raman emission in a flat, clear, ocean at shorter wavelengths (< 500 nm).

2. Skylight conditions may allow for a 2% decrease in water Raman emission relative to a simple solar beam at shorter wavelengths.

3. The mean cosine of the light field of the source wavelength for Raman emission controls the increase in water Raman emission.

4. At shorter wavelengths (< 490 nm) the increased water Raman scattering increases the irradiance ratio R in the near surface layers while at longer wavelengths (> 520 nm) the irradiance ratio R increases at depth from increased absorption of solar photons.

5. The increase in the R value in water due to Raman emission and solar zenith angle is generally not found in air.

7. ACKNOWLEDGEMENTS

8. REFERENCES

1. R. H. Stavn and A. D. Weidemann, "Raman scattering effects in ocean optics," in Ocean Optics IX (M. A. Blizard, ed.), SPIE Proceedings, Vol. 925, 131-139 (1988).

2. R. H. Stavn and A. D. Weidemann, "Ocean optical modeling: Raman scattering effects," Appl. Opt., 27(19), 4002-4011 (1988).

3. B. R. Marshall, "Raman scattering in ocean water," Master's Thesis, Geography Department, U. California at Santa Barbara (1989).

4. B. R. Marshall and R. C. Smith, "Raman scattering and in-water ocean optical properties," Appl. Opt., 29(1), 71-84 (1990).

5. R. H. Stavn, "Raman scattering effects at the shorter visible wavelengths in clear ocean waters," in Ocean Optics X (R. W. Spinrad,ed.), SPIE Proceedings, Vol. 1302, 94-100 (1990).

6. R. H. Stavn, "The effects of Raman scattering across the visible spectrum in clear ocean water: a Monte Carlo study," (in review, Applied Optics).

7. A. Morel,"Optical properties of pure water and pure sea water," in Optical Aspects of Oceanography (N. G. Jerlov and E. Steemann Nielsen, eds.),1-24, Academic Press, London (1974).

8. R. C. Smith and K. S. Baker, "Optical properties of the clearest natural waters," Appl. Opt., 20(2), 177-184 (1981).

9. A. C. Tam and C. K. N. Patel, "Optical absorption of light and heavy water by laser optoacoustic spectroscopy," Appl. Opt., 18, 3348-3358 (1979).

10. S. Sugihara, M. Kishino, and M. Okami, "Contribution of Raman scattering to upward irradiance in the sea," J. Oceanogr. Soc. Japan, 40, 397-404 (1984).

11. W. F. Murphy and H. J. Bernstein, "Raman spectra and an assignment of the vibrational stretching region of water". J. Phys. Chem. 76, 1147-1152 (1972).

12. T. J. Petzold, "Volume scattering functions for selected ocean waters", Univ. California, San Diego, Scripps Inst. of Oceanography, San Diego, CA, SIO Ref. 72-78 (October 1972).

13. G. Kullenberg, "Scattering of light by Sargasso sea water. Deep-Sea Res. 15(4), 423-432 (1968).

14. M. Iqbal, An Introduction to Solar Radiation, Academic Press, New York (1983).

15. D. T. Brine and M. Iqbal, "Diffuse and global solar spectral irradiance under cloudless skies," Solar Energy 30(5), 447-453 (1983).

16. A. W. Harrison and C. A. Coombes, "Angular distribution of clear sky short wavelength radiance," Solar Energy, 40(1), 57-63 (1988).

17. K. S. Baker and R. Frouin, "Relation between photosynthetically available radiation and total insolation at the ocean surface under clear skies," Limnol. Oceanogr., 32(6), 1370-1377 (1988).

18. R. H. Stavn, F. R. Schiebe, and C. L. Gallegos, "Optical controls on the radiant energy dynamics of the air/water interface: the average cosine and the absorption coefficient," in Ocean Optics VII (M. A. Blizard, ed.), SPIE Proceedings, Vol. 489, 62-67 (1984).
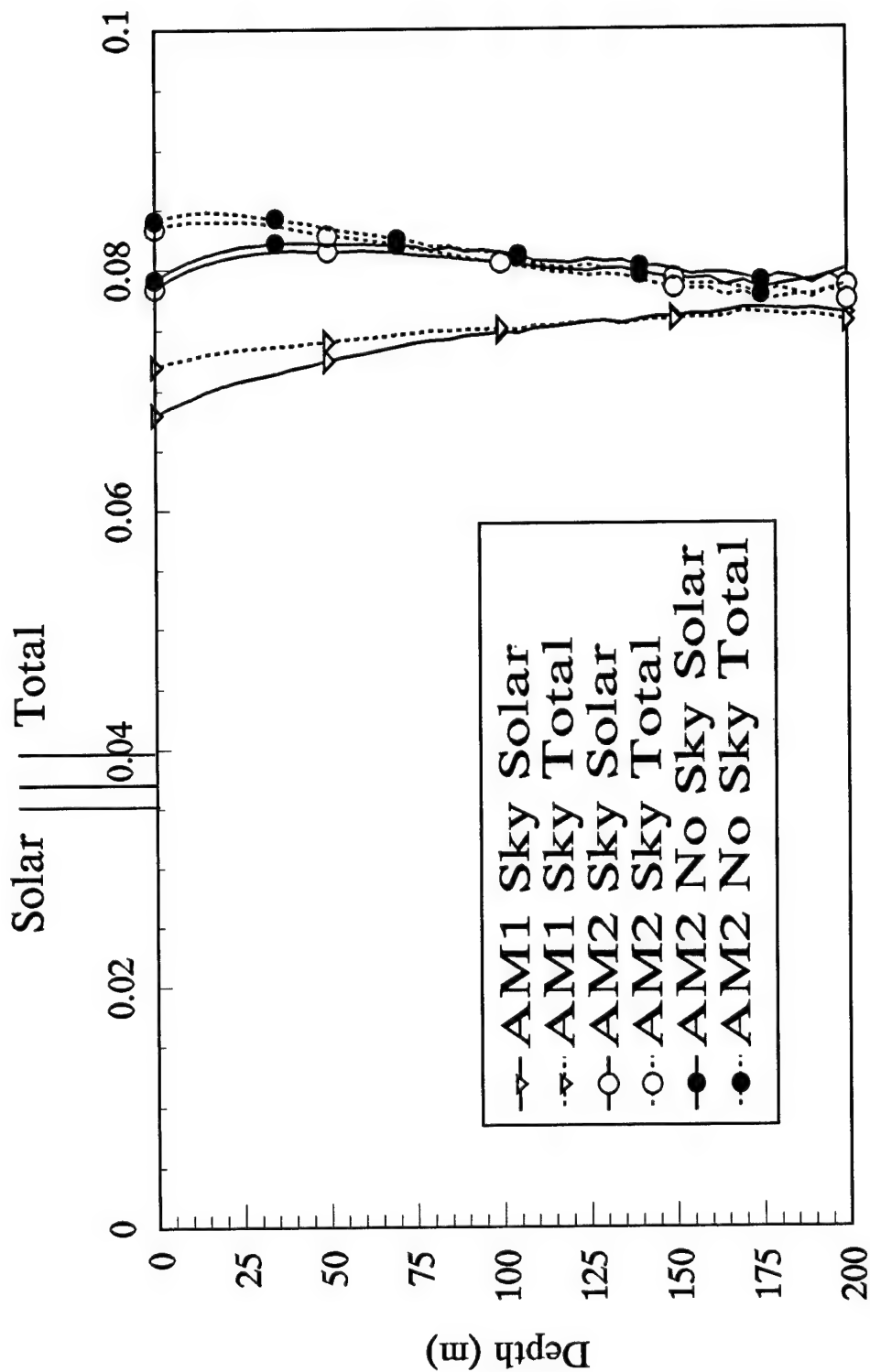
Irradiance Ratio : R

Figure 1. The ratio of upwelling irradiance E_u to downwelling irradiance E_d for both solar photons and total (solar + Raman) photons at 430 nm for a clear ocean with a flat surface. Optical conditions external to the hydrosol are skylight present and absent and solar zenith described by air mass 1 (AM 1) and air mass 2 (AM 2).
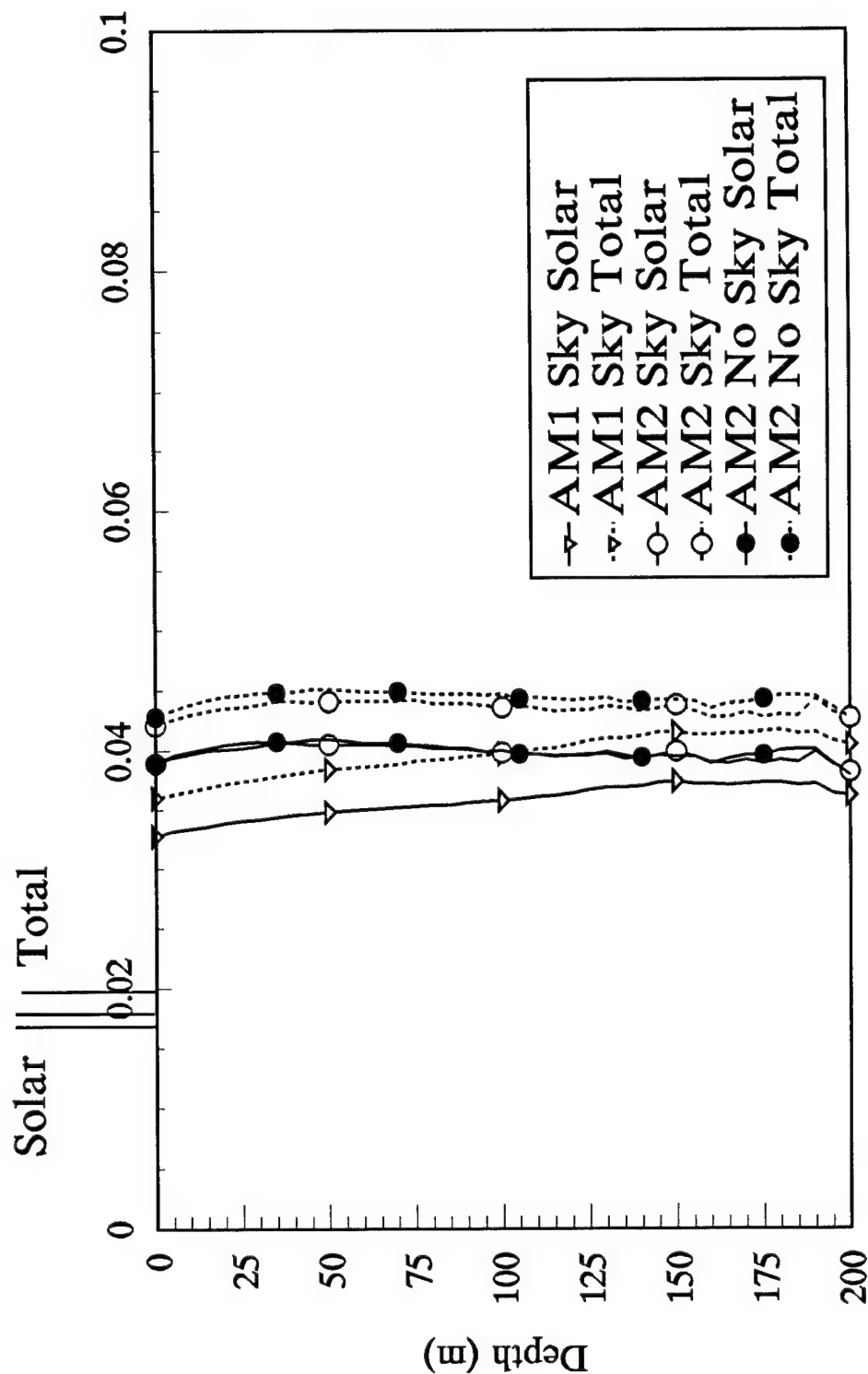
Figure 2. The ratio of upwelling irradiance E_u to downwelling irradiance E_d for both solar photons and total (solar + Raman) photons at 490 nm for a clear ocean with a flat surface. Optical conditions external to the hydrosol are skylight present and absent and solar zenith described by air mass 1 (AM 1) and air mass 2 (AM 2). R in air extends up from the R axis and labelled Solar and Total (Solar + Raman).
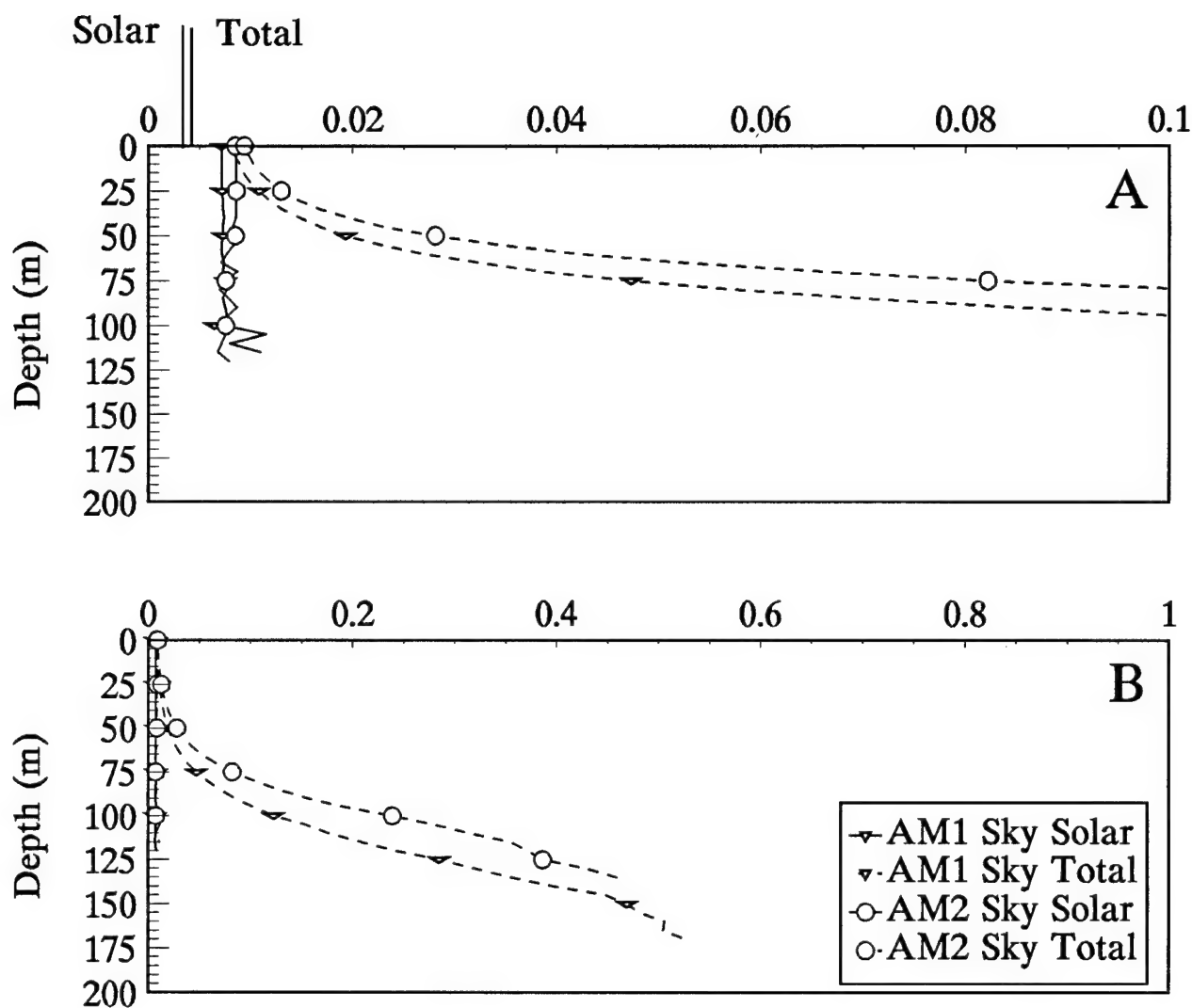
Irradiance Ratio : R

Figure 3. The ratio of upwelling irradiance E_u to downwelling irradiance E_d for both solar photons and total (solar + Raman) photons at 550 nm for a clear ocean with a flat surface. Optical conditions external to the hydrosol are skylight present and solar zenith described by air mass 1 (AM 1) and air mass 2 (AM 2). A) The R axis is 0.1 at the maximum. R in air extends up from the R axis and labelled Solar and Total (Solar + Raman). B) The R axis is 1.0 at the maximum.

Raman scattering in ocean optics: quantitative assessment of internal radiant emission

Robert Hans Stavn and Alan Dean Weidemann

Raman-scattering activity in clear ocean waters is further documented from Monte Carlo simulations and optical data that are collected in the Sargasso Sea. A method is proposed, based on the anomalous absorption coefficient for a nonconservative irradiance field, to assess the percentile composition of internal radiant emission for the irradiance field at any depth.

Key words: Raman scattering, ocean optics, anomalous ocean optical properties, photon budgets.

Introduction

Internal radiant emission in clear oceans has recently been implicated as a possible cause of anomalous ocean optical properties that are determined from the irradiance field at longer wavelengths.[1-5] Various reports indicate that at longer visible wavelengths the absorption coefficient a calculated from the irradiance field is less than the accepted value for molecular water.[6-9] In addition the diffuse attenuation coefficient K (both downwelling and upwelling) in certain cases is smaller than the coefficient that is accepted for molecular water.[3-5,10-12] Furthermore recent attempts to parameterize the penetration of clear ocean waters by sunlight by using diffuse attenuation coefficients derived from the surface layers of the clearest ocean waters[13] have not been successful. The results of these parameterizations indicate more photons at depth than would be expected if the solar photons were being absorbed by molecular water.[14,15] Thus in clear ocean waters we have evidence of internal radiant emission, and water Raman scattering has been invoked to explain many of the effects noted above.[1-5] Other sources of internal radiant emission are, to be sure, fluorescence from dissolved organic matter[16-20] and suspended living algae with specific pigment emission peaks.[21-23] However, the water molecule is a fundamental source of internal emission in

clear oceans, and it must be accounted for in addition to other added components in the marine hydrosol. The other components become more significant as we progress from clear ocean waters to coastal and inland waters. Even in coastal waters, however, Carder *et al.*[24,25] have reported what appear to be water Raman emission effects at 650 nm.

We therefore propose continuing with the results that are generated from the National Oceanographic and Atmospheric Research Laboratory (NOARL) optical model, a Monte Carlo solution of the radiative transfer equation, which is applied to clear ocean waters. These simulations of the light field in clear ocean water will then be compared with the field data collected by NOARL on the cruise of the R/V Endeavor (EN-166) as part of the Biowatt–NOARL cruise to the Sargasso Sea. We then describe a method to assess quantitatively the amount of internally emitted radiation at any point in the marine hydrosol.

Theory

The proposed explanation of the anomalous optical properties reported in the literature is the presence of internal radiant emission. In clear ocean waters with a minimum of dissolved and suspended material the primary source of internal radiant emission is water Raman scattering. The effect of this emission on the inherent absorption coefficient calculated from the irradiance field is simple and quantitative. In this discussion we assume that the irradiance field is a function of wavelength without an explicit statement in the equations. The calculation of the absorption coefficient from the ambient irradiance field is based on Gershun's equation,[26] and the potential of internal radiant emission in producing an anomalous determination of this coefficient was pointed out by Højerslev.[27] The three-parameter model,[28] which is an exact

R. Stavn is with the Department of Biology, University of North Carolina at Greensboro, Greensboro, North Carolina 27412. A. Wiedemann is with the National Oceanographic and Atmospheric Research Laboratory, Code 331, Stennis Space Center, Mississippi 39529.

solution to the radiative transfer equation, allows the calculation of the absorption coefficient from the ambient irradiance field even in the presence of multiple scattering. This is the calculation that we use to determine the absorption coefficient from field irradiance data and as a check on the output of the Monte Carlo simulations. This light field formulation requires the scalar irradiance E_0, the downwelling irradiance E_d, and the upwelling irradiance E_u. From this we obtain the net downwelling irradiance or downwelling vector irradiance $E_z = E_d - E_u$ and also determine the average cosine of the mean photon path of the light field.[29] The average cosine parameter proves to be important in assessing the nature of the light field, i.e., whether the light field seems to be dominated by the penetration of solar photons only or are there significant effects caused by internal radiant emission? The average cosine is determined by the simple ratio

$$\bar{\mu} = \frac{\mathbf{E}_z}{E_0}. \tag{1}$$

This light field parameter[30] (also termed by Preisendorfer[31] an apparent optical parameter) varies in absolute value from 0.0 to 1.0, a low value indicating nearly equal upwelling and downwelling radiant fluxes, while a value approaching 1.0 indicates that nearly all the radiant flux is propagated in a vertically downward direction. Therefore the average cosine is a sensitive indicator of the radiance distribution and structure of the submarine light field.

The fundamental Gershun equation that is used for determining the absorption coefficient from the ambient irradiance field is defined as

$$\nabla \cdot \mathbf{E}(z) = -a(z)E_0(z), \tag{2}$$

where $\mathbf{E}$ is the vector irradiance of the light field and z is the geometric depth in meters. Preisendorfer[31] pointed out that, when there is no horizontal divergence of the light field, the left-hand side of Eq. (2) becomes a function of only the irradiant flux of the vertical axis (z axis). This vertical component of the vector irradiance is the downwelling vector irradiance, also termed the net downwelling irradiance with reference to its being the difference between the downwelling irradiance and the upwelling irradiance, and

$$\frac{\mathrm{d}E_z(z)}{\mathrm{d}z} = -a(z)E_0(z). \tag{3}$$

Solving Eq. (3) by substituting Eq. (1) into it, we obtain a general radiative transfer equation[32] that can be recast in several forms:

$$E_0(z) = E_0(0) \frac{\bar{\mu}(0)}{\bar{\mu}(z)} \exp -\left[\int_0^z \frac{a(z)}{\bar{\mu}(z)} \, \mathrm{d}z \right]. \tag{4}$$

From this equation comes a general relationship for calculating the absorption coefficient for a depth interval assuming that a is constant over the interval, as is common practice. We calculate the absorption coefficient in Eq. (5) where the integral in the denominator accounts for changes in the photon path (as measured by the average cosine) that are caused by multiple scattering:

$$a(z) = -\frac{\ln [\mathbf{E}_z(z_2) - \ln \mathbf{E}_z(z_1)]}{\int_{z_1}^{z_2} \frac{1}{\overline{\mu}(z)} \, \mathrm{d}z}. \tag{5}$$

For the quantitative assessment of the effects of internally emitted radiation we take advantage of the fact that this calculation requires a conservative light field.

When the irradiance field is not conservative, i.e., internal radiant emission (water Raman scattering, fluorescence, or bioluminescence) is taking place at the wavelength of interest, we must add new terms to Eq. (3):

$$\tilde{a}(z) = -\frac{1}{[E_0(z) + E_0{}^*(z)]} \frac{\mathrm{d}[E_z(z) + E_z{}^*(z)]}{\mathrm{d}z}, \tag{6}$$

where $E_z{}^*(z)$ is the net irradiant flux caused by the internal radiant emission, $E_0{}^*(z)$ is the scalar irradiance caused by internal radiant emission, and $\tilde{a}(z)$ is the absorption coefficient at depth z calculated from the nonconservative irradiance field. In clear ocean water we assume that the major source of internal radiant emission is water Raman scattering. With an algebraic rearrangement of Eq. (6) and timely substitution of Eq. (3),

$$[E_0(z) + E_0{}^*(z)]\tilde{a}(z) + \frac{\mathrm{d}E_z{}^*(z)}{\mathrm{d}z} = -\frac{\mathrm{d}E_z(z)}{\mathrm{d}z},$$

$$E_0(z)a(z) = [E_0(z) + E_0{}^*(z)]\tilde{a}(z) + \frac{\mathrm{d}E_z{}^*(z)}{\mathrm{d}z},$$

$$\Delta a(z) = a(z) - \tilde{a}(z),$$

where $a(z)$ is the inherent absorption coefficient of the hydrosol measured spectrophotometrically and

$$\Delta a(z) = a(z) - \left\{ \frac{E_0(z)}{[E_0(z) + E_0{}^*(z)]} a(z) \right.$$

$$\left. + \frac{1}{[E_0(z) + E_0{}^*(z)]} \frac{\mathrm{d}E_z{}^*(z)}{\mathrm{d}z} \right\}. \tag{7}$$

The $E_z{}^*(z)$ term, the difference between the upwelling and downwelling fluxes from internal emission, is relatively small because the two fluxes are nearly equal. If there were no contribution of flux from depths above and below depth z, the $E_z{}^*(z)$ term would be exactly zero. The relative effects of multiple scattering and differential absorption, which are greater at shorter wavelengths, will alter this relationship somewhat. The derivative of $E_z{}^*(z)$ with depth will be an even smaller number. Thus we assume that the last term inside the braces on the right-hand side

of Eq. (7) is approximately zero. Then

$$\frac{\Delta a(z)}{a(z)} \cong 1 - \frac{E_0(z)}{[E_0(z) + E_0{}^*(z)]},$$

$$\frac{\Delta a(z)}{a(z)} \cong \frac{E_0{}^*(z)}{[E_0(z) + E_0{}^*(z)]}. \qquad (8)$$

The output of the Monte Carlo simulations of both direct solar and Raman photon fluxes permits us to calculate Δa by using both the exact relation from Eq. (7) and the approximate relation from Eq. (8) as a check on this approximation. The deviation between the two estimates varies from 0.01 to 0.1%. Our derivation involves an absorption coefficient $\tilde{a}(z)$, which is determined from the ambient nonconservative light field, and the inherent absorption coefficient of the hydrosol $a(z)$, which is determined spectrophotometrically. The ratio of the deviation of the nonconservative absorption coefficient $[\tilde{a}(z)]$ from the inherent absorption coefficient $[a(z)]$ to the inherent absorption coefficient is a quantitative estimate of the percentile composition of the emission photons in the light field. Therefore we propose that this ratio be used in the decomposition of the ambient light field into directly penetrating solar photons and internally emitted photons. This determination includes emission from all sources, such as fluorescence. This ratio, which is illustrated on the left-hand sides of approximations (8), may be called the relative absorption anomaly.

Methods

The NOARL optical model is a Monte Carlo simulation of the radiative transfer equation that describes the penetration of solar photons into ocean waters and accounts for the transpectral water Raman scattering. The Monte Carlo simulation is derived from the methods of Plass and Kattawar,[33] Gordon and Brown,[34] and Kirk.[35] The required inputs for simulating the penetration and fate of solar photons in ocean waters are the absorption coefficient, the total-scattering coefficient, and the volume-scattering function. The volume-scattering functions of each scattering component (molecular water, quartzlike particulates, algae, organic detritus) are treated separately rather than being used as an average volume-scattering function. The NOARL Blue Water model used in this simulation contains the absorption coefficients for molecular water of up to 570 nm reported by Smith and Baker[13]; the coefficients reported by Tam and Patel[36] are used for coefficients at wavelengths that are >570 nm. Recent investigations of the backscattered upwelling radiance from ocean waters indicate that this is the most efficient combination of absorption coefficients.[37] The total-scattering coefficient and the volume-scattering function of pure seawater are incorporated from Morel,[38] and the total-scattering coefficient and volume-scattering function for quartzlike material are incorporated from Kullenberg[39] and Gordon et al.[40] The Raman-scattering coefficient for molecular water was determined from the molecular Raman-scattering cross section reported by Chang and Young.[41] The Raman-scattering coefficient was then truncated to generate only emissions in the 10-nm wave band of the emission wavelength studied, as described earlier.[2] The simulations were performed at 520, 550, and 589 nm to correspond with the wavelengths that are available for study on the NOARL instrument called the particle–optical sampling system.

For a simulation run photons are transported through a clear marine aerosol for both a Raman source wavelength and a Raman emission wavelength, the determination being made on the basis of a 3357-cm⁻¹ frequency shift from the source wavelength to the emission wavelength. The relative numbers of photons propagated at the two wavelengths are determined from the extraterrestrial solar irradiance spectrum reported by Iqbal.[42] The atmospheric model of Iqbal is then used to propagate solar and skylight photons through the marine aerosol to sea level. The angle of entry of a skylight photon is determined from the skylight radiance distribution of Harrison and Coombes,[43] while the entry angle of a solar photon is at 11° from the zenith. The sea surface is flat. At the air–water interface the photon either enters the ocean and is refracted or is reflected back into the air based on the laws of Fresnel and Snell. These laws are used to determine the probabilities of these events that are chosen by a random number generator. On entry into the ocean a photon can be absorbed, scattered, or transpectrally scattered. The probabilities of these events are determined from the respective coefficients of the model, and the individual events are chosen by a random number generator. When a photon is finally absorbed, a new one is generated and propagated through the system until 2.5×10^6 photons have been propagated. Duplicate runs are made for the wavelength that is studied.

The downwelling and upwelling irradiances and scalar irradiances collected during the Endeavor cruise were measured with a Biospherical Instruments, Inc. (San Diego, Calif.) Model MER 1048 attached to the particle–optical sampling system. This instrument was equipped with thirteen downwelling irradiance channels, eight upwelling irradiance channels, four downwelling hemispherical scalar irradiance channels, and four upwelling hemispherical scalar irradiance channels. The instrument package was attached to a rosette to permit the collection of water samples at selected depths, and the sensors for transmittance, conductivity, temperature, pressure, and fluorescence were also attached to the rosette. The dark current for the irradiance sensors was determined periodically by lowering the instrument until random fluctuations in output were observed (usually below 200 m). The downcast rate vaired from 0.2 to 0.8 m/s.

Ship motion and wave focusing resulted in large fluctuations for downwelling irradiances and downwelling hemispherical scalar irradiances that required some filtering for the estimation of the irradiances used in the optical calculations. After

Table I. Optical Coefficients Determined for the R/V Endeavor Cruise

Depth (m)	Yellow Substance a_y (520) m^{-1}	Particulates a_p (520) m^{-1}	Molecular Water a_w (520) m^{-1}	Total a(520) m^{-1}
		Station 6		
27	<0.001[a] ± 0.0006	0.003 ± 0.0006	0.0477	0.0507 ± 0.0009
80	0.004 ± 0.0022	0.009 ± 0.0018	0.0477	0.0607 ± 0.0028
		Station 8		
34	0.006 ± 0.003	0.003 ± 0.0006	0.0477	0.0567 ± 0.003
100	0.007 ± 0.004	0.008 ± 0.0016	0.0477	0.0627 ± 0.0043

[a]Error calculated by assuming that the absorption coefficient is 0.001 m^{-1}.

normalizing to surface irradiance, exponential regression was performed on 2-m bins with a 1-m increment for Station 6, while Station 8 required this procedure plus two passes of a smoothing filter.

The absorption coefficients determined directly for water samples collected by the particle–optical sampling system were obtained by the following methods:

Water absorption: The absorption coefficient of pure seawater at 520 nm was determined from the tables of Smith and Baker.[13]

Gelbstoff absorption: We define dissolved substances as those that pass through a 0.22-μm Nucleopore filter.[44] The absorption was measured on the filtrate in 10-cm cuvettes from 320 to 420 nm. The spectra showed an exponential rate of decline with increasing wavelength, the rate constants varying from 0.014 to 0.024 with a mean of 0.017. These rates are in line with those reported by other investigators.[7,30,45] Absorption at wavelengths that are >420 nm was determined by extrapolation of the exponential curve. The variation in the rate constant was used to estimate the error in the absorption coefficients reported in Table I.

Particulate absorption: The contribution by particulates was determined spectrophotometrically following the procedures of Mitchell and Kiefer.[22] Two to four liters of water were filtered through GF/C (Whatman) filters, and the spectral absorption was measured from 400 to 750 nm on a Kontron dual-beam (model Uvikon 860) spectrophotometer with a blank saturated GF/C filter. Absorption between 740 and 750 nm was used to correct the spectrum for backscattered light. The absorption coefficient was determined by employing the equation of Mitchell and Kiefer.[22] This procedure may underestimate particulate absorption between the size classes of 0.22 μm (dissolved substance limit) and 0.8 μm (GF/C nominal retention). Recently Mitchell[46] reported on the precision and accuracy of this absorption measurement technique. The use of GF/C filters may result in an underestimate of particulate absorption by as much as 25%. Extensive experimental tests of the Mitchell/Kiefer algorithm indicated an overall precision of ±10%. The variation between filter lots can add another error of ±10%. We therefore estimate an error of ±20% for the particulate absorptions reported in Table I. It should also be kept in mind that the values in Table I are likely to be underestimates of the particulate absorption. The total laboratory absorption coefficient was calculated as the sum of the contributions from water, gelbstoff, and particulates.

Results

The simulation from the NOARL Blue Water model yielded the following results for clear ocean water irradiated by a clear sky composed of a marine aerosol; the coefficients used for the simulation are reported in Table II. The average cosines for the separate Raman and solar photon streams are plotted

Table II Optical Coefficients Used in Monte Carlo Simulation

| Coefficients (m^{-2})	Source Wavelengths (nm)			Emission Wavelength (nm)
	433	443	453	520
Absorption	0.0145	0.0145	0.0147	0.0477
Scattering	0.0402	0.0389	0.0377	0.0314
Raman scattering	0.0000967	0.000400	0.000060	—
	454	464	474	550
Absorption	0.015	0.0156	0.0165	0.0638
Scattering	0.0375	0.0364	0.0354	0.0293
Raman scattering	0.0000909	0.000312	0.0000508	—
	482	492	502	589
Absorption	0.0180	0.0207	0.0275	0.1250
Scattering	0.0346	0.0337	0.0328	0.0271
Raman scattering	0.0000896	0.000232	0.0000411	—
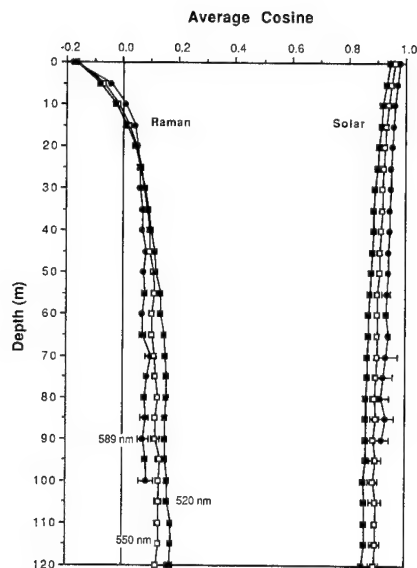
Fig. 1. Average cosine of the separate photon streams: directly transmitted solar photons and Raman emission photons at various wavelengths. The standard errors of the estimates are indicated by either vertical bars or the width of the dot.

Fig. 3. Absorption coefficients at 520 nm. The inherent absorption coefficient for water molecules is indicated by a straight line, and the nonconservative absorption coefficient is indicated by the curve and data points. The standard errors are indicated by either vertical bars or the width of the dot.

in Fig. 1. The average cosine for the solar photons varies from 0.94 to 0.98 at the surface to 0.86–0.91 at the maximum depth for all wavelengths considered. By contrast the Raman photons have an average cosine of (-0.2) at the surface, 0.0 in the region of 10–15-m depth, and 0.09–0.14 at the greatest depths. In Fig. 2 the average cosine of the combined streams is plotted for each wavelength. In Figs. 3–5 are plotted the nonconservative absorption coefficients of the Raman-influenced irradiance fields at 520, 550, and 589 nm, respectively. The nonconservative absorption coefficients deviate increasingly with depth from the inherent absorption coefficients and then deviate markedly from the inherent absorption coefficients at

140, 100, and 60 m, respectively. The relative absorption anomalies that are determined from the model output are plotted against the actual ratios of Raman photons to the total photons of the model output (Figs. 6–8). There is a 1–1 correspondence between the two ratios for all the wavelengths that were investigated.

Figures 9–12 show plots of the data that were collected during the Biowatt–NOARL cruise of Aug. 1987 to the Sargasso Sea. The stations were located in the region of 34°N, 69–70°W. The field results provide
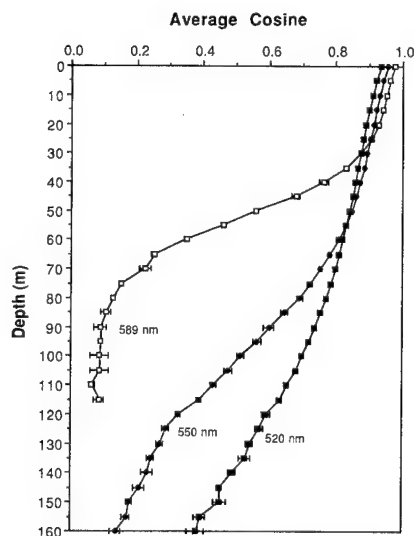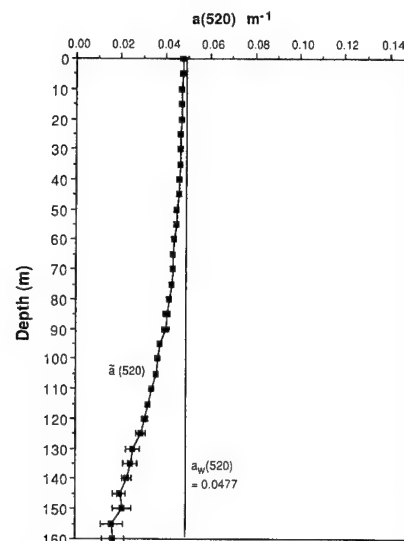

Fig. 2. Average cosine of the combined solar and Raman photon streams as would be measured in the ocean. The standard errors are indicated by either vertical bars or the width of the dot.
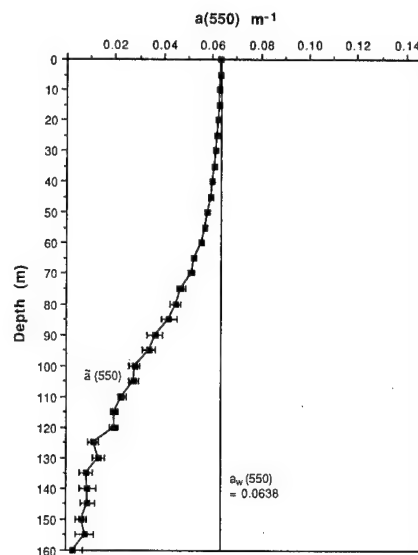

Fig. 4. Absorption coefficients at 550 nm. The inherent absorption coefficient for the water molecules is indicated by a straight line, and the nonconservative absorption coefficient is indicated by a curve and data points. The standard errors are indicated by either vertical bars or the width of the dot.
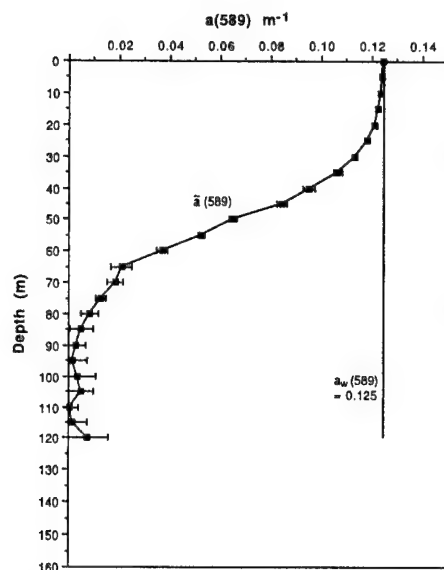
Fig. 5. Absorption coefficients at 589 nm. The inherent absorption coefficient for water molecules is indicated by a straight line, and the nonconservative absorption coefficient is indicated by a curve and data points. Standard errors are indicated by either vertical bars or the width of the dot.

Fig. 7. Fraction of Raman emission photons in total scalar irradiance at 550 nm compared to the relative absorption anomaly from the NOARL Blue Water model output.

further evidence of water Raman emission at the three wavelengths studied in the green-yellow region of the visible spectrum. The stations chosen for further analysis were the ones in which there were data on both the ambient light field and on the inherent absorption coefficients of the water samples collected at the stations. A complete suite of irradiance measurements was possible at 520 nm to allow for the determination of the average cosine parameter and the calculation of the absorption coefficient from the irradiance field.

Upwelling and downwelling irradiances were measured at 550 nm, and only the downwelling irradiance was measured at 589 nm. The average cosine for the light field at 520 nm from Station 4 is plotted in Fig. 9 along with the average cosine generated by the NOARL Monte Carlo simulation. The values of the average cosine near the surface indicate probable
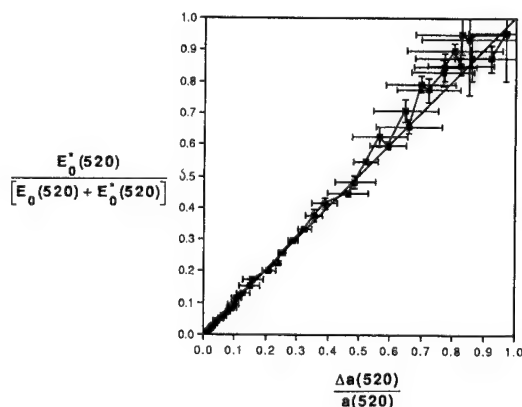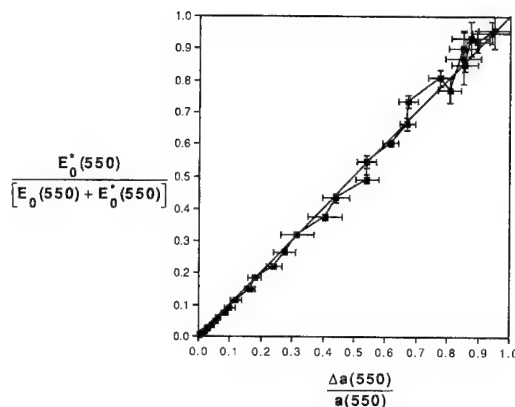
wave-focusing effects, which increases the mean photon path and thus decreases the average cosine. At greater depths agreement is within 8% down to ~80 m where a sharp decrease in the average cosine at 75–80 m from the prediction based on water Raman scattering may indicate particulate fluorescent activity. In Fig. 10 is plotted the irradiance ratio (E_u/E_d) for 550 nm at Station 6. The trend of the ratio follows that predicted by the NOARL Monte Carlo simulation. The logarithm of the downwelling irradiance E_d at 589 nm for Station 6 is plotted in Fig. 11 along with the predicted penetration of solar photons at this wavelength and the predicted solar plus Raman photons at this wavelength. At a 40-m depth the photons start to deviate from the level predicted only for solar photons; i.e., there are more photons present below these depths than can be accounted for by the transmission of solar photons through a medium consisting of only molecular water. The ocean contains dissolved and suspended materials in addition to molecular water that would also absorb photons.

The nonconservative absorption coefficients and the spectrophotometrically determined absorption coefficients for Endeavor Stations 6 and 8 are plotted in Fig. 12. The individual components of the spectropho-
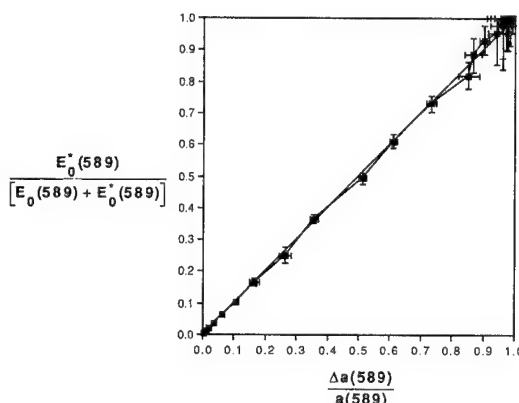

Fig. 6. Fraction of Raman emission photons in total scalar irradiance at 520 nm compared to the relative absorption anomaly from the NOARL Blue Water model output.

Fig. 8. Fraction of Raman emission photons in the total scalar irradiance at 589 nm compared to the relative absorption anomaly from the NOARL Blue Water model output.
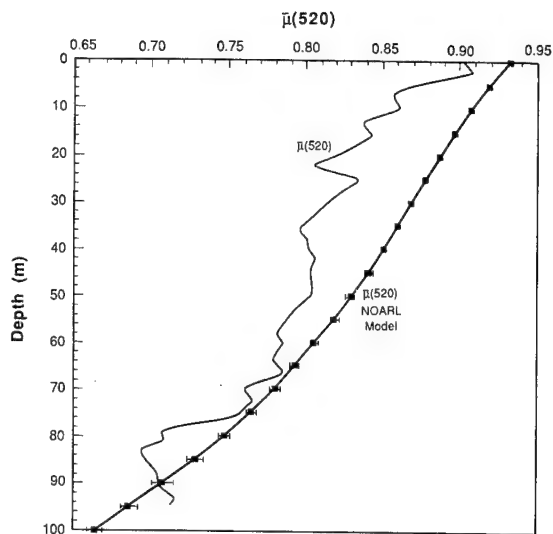
Fig. 9. Average cosine at 520 nm for Station 4, Endeavor cruise EN-166 and from the output of the NOARL Blue Water model.

Fig. 11. Natural logarithm of the downwelling irradiance at 589 nm. The solid curves with a low variance represent the output from the NOARL Blue Water model normalized to the mean irradiance measured at Station 6 at the surface. The solid curve with a relatively high variance is a natural logarithm of measured downwelling irradiance in $\mu W/cm^2/nm$.

tometrically determined absorption coefficients at those stations are in Table I. The tendency for the absorption coefficient anomaly to increase with depth is evident at the two stations; there is also the possibility that the layering of absorbent or fluorescent material at Station 6 is superimposed on the depth trend.

Oceanic Radiant Flux Field: Quantitative Characterization

We have demonstrated that various troublesome and anomalous phenomena associated with measured clear ocean irradiance fields and the optical parameters calculated from them can be attributed to water Raman scattering. The average cosine that was recorded from the data of the Biowatt–NOARL cruise collected at 520 nm indicates the presence of water
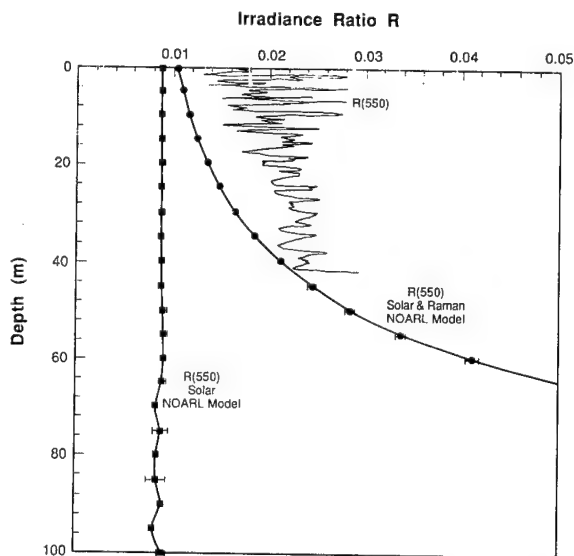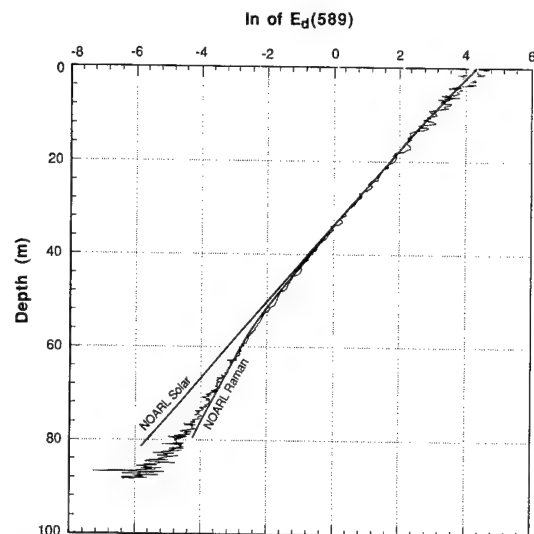
Raman scattering when compared with the results of the NOARL Blue Water model simulation (Fig. 9). This was reported earlier,[2] and we confirm those results here with the data from a different station. The irradiance ratio that is plotted for 550 nm in Fig. 10 shows an increase in this ratio over that expected for clear ocean waters, as is predicted from the NOARL Monte Carlo simulation.

The effects of water Raman scattering on downwelling irradiance, which is the most common irradi-

Fig. 10. Irradiance ratio at 550 nm for Station 6, Endeavor cruise EN-166, and from the output of NOARL Blue Water model.
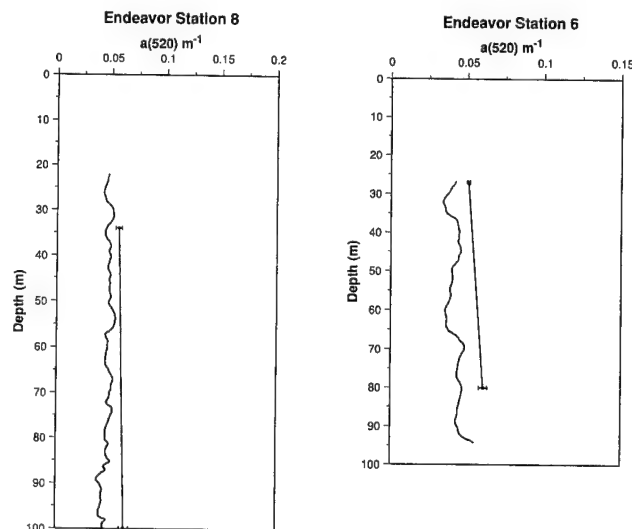

Fig. 12. Absorption coefficients for two stations. The straight lines represent inherent absorption coefficients of hydrosol collected at depths that are indicated by black dots. The experimental errors of inherent absorption coefficients are indicated by error bars. The curves represent the nonconservative absorption coefficient calculated from the ambient irradiance field.

ance measurement, are subtle at shorter wavelengths and in the predominantly green region of the irradiance spectrum. The effects begin to show up strongly in the downwelling irradiance as we progress toward the longer yellow wavelengths (589 nm) as shown in Fig. 11 and confirmed by Marshall and Smith.[4] Thus the effects of water Raman scattering tended to go unnoticed in previous field investigations, especially those that were limited to downwelling irradiance measurements. The effects that were noticed were often attributed to light leakage or spectral cross talk,[4,10,14] a relatively wide filter bandwidth,[4] or similar instrumentation effects. The average cosine parameter accounts for the possibility of light leakage and similar problems, because if the anomalies in the irradiance readings and average cosines etc. are due to instrumentation problems, the average cosine would be identical to that of the source wavelength for leakage or spectral cross talk. The average cosine recorded at depth from the Sargasso Sea at 520 nm is less than that of the possible source wavelengths. We do not have data on the average cosine at other wavelengths, but we do have the predictions for the pattern of the average cosine at other wavelengths with the presence of water Raman scattering (Fig. 2). Marshall and Smith[4] have pointed out that the 589-nm region is one where the absorption coefficient of the water molecule is changing rapidly, and the fact that the light filters for the MER 1048 instrument have a finite bandwith (10 nm) will cause problems with the estimation of photons at the nominal 589-nm wavelength. The Gaussian-type shape of the filter's transmission curve will allow photons that are adjacent to the nominal passband to be recorded as photons of 589 nm. This phenomenon could explain the apparent increase in photons at 589 nm with the penetration of the solar light field as recorded in Fig. 11. However, Marshall and Smith[4] have calculated the probable effect of the finite bandwidth of the MER filter at 589 nm on the apparent number of photons of 589 nm that were recorded at various depths in clear ocean water. At a depth of 60 m the effect of Raman emission, an increase in photons over those predicted by transmission of solar photons, is easily detectable. The calculated $K_d(589)$ coefficient is less than the $K_d(589)$ coefficient that was predicted by Marshall and Smith for the penetration of photons at 589 nm supplemented by photons not excluded by the optical filter. Thus the curve for the downwelling irradiance at 589 nm in Fig. 11 cannot be explained as an effect of the finite optical filter bandwidth, although it may be making a contribution.

Recent attempts to parameterize the penetration of solar photons into clear ocean waters by using diffuse attenuation coefficients measured over the visible spectrum in the surface layers are possibly hampered by the effects of internal radiant emission. Tests of these parameterizations in clear ocean waters indicate that the models consistently underestimate the total photons present at depths that are >80 m by 50% or more.[14,15] The absorption coefficient anomalies derived from the NOARL Monte Carlo output indicate that a significant admixture of water Raman photons to the longer (green-yellow) wavelengths of the clear ocean irradiance occurs at depths of 60–100 m (Figs. 3–5). The assumption that all the photons that are lost at a given wavelength are converted to heat does not allow for accurate predictions as one goes deeper into clear ocean waters. Internal radiant emission, in the form of water Raman scattering and possibly fluorescence at certain wave bands, allows for the conversion of shorter-wavelength photons into longer-wavelength photons on penetration of the solar beam. Thus a percentage of the photons that are presumed removed from the downward photon stream in these parameterizations is not removed from the stream but is simply changed in the wavelength. Since this percentage of photons remains in the photon stream, the anomaly associated with the two attempted parameterizations is easily explained. These excess photons at depth then explain the anomalously low absorption and diffuse attenuation coefficients reported at longer wavelengths (in the green-yellow region) in clear ocean waters.

The presence of water Raman scattering in clear ocean waters alters the submarine light field to the point that quantitative estimations of the penetration and fate of the total solar photons have not been possible heretofore. It is necessary to assess the proportion of a measured light field that is due to internal emission and the proportion that comes from directly transmitted, unaltered solar photons. Then we will be able to construct energy-photon budgets for the study of the penetration and fate of solar radiant energy in the world ocean. We have reported two parameters that help in the quantitative estimation of water Raman emission: the average cosine and the absorption coefficient anomaly.

The quantitative estimation of the percentage of photons due to internal radiant emission at any point of the marine hydrosol requires two different measurements: the irradiance field (the net downwelling irradiance and the scalar irradiance) and a spectrophotometric measurement of the inherent absorption coefficient of a water sample that is taken from the depth of interest. This was done on the R/V Endeavor with the spectrophotometry performed on board ship soon after the samples were collected. Many investigators are now working on improved instruments for directly determining the inherent absorption coefficient more accurately on board ship and *in situ*.[47-50] The use of approximation (8) permits a simple determination of the percentage of photons caused by internal radiant emission at any point in the marine hydrosol; the equation is an approximation, and the assumptions that are used to derive it were demonstrated to be robust in Figs. 6–8. The relative absorption anomaly that is used in approximation (8) was shown to be an accurate predictor of the percentile composition of emission photons in the ambient photon field. The reason we are able to indirectly tag the ambient photons in this method is the fact that

the solar photon stream and the Raman photon stream each have different mean photon paths as measured by the average cosine parameter (see Fig. 1). Thus the contributions of the two photon streams to the terms of Eq. (6) are not equivalent because internal emission makes almost no contribution to the net downwelling irradiance of the total photon stream. The upwelling and downwelling irradiances that originate from internal emission are nearly equal, and the net downwelling irradiance, the difference between the two photon streams, becomes very small, approaching zero as a limit. The contribution of internally emitted photons to the total scalar irradiance is relatively small near the surface compared with the solar photon stream but increases with depth as the solar photons are removed by absorption. The discrepancy between the two contributions of internal emission to the terms of Eq. (6) creates the absorption coefficient anomaly, which is the difference between the calculated nonconservative absorption coefficient and the inherent absorption coefficient of the hydrosol. When we compare the absorption coefficient anomaly that is predicted for water Raman scattering alone in Fig. 3 with the anomalies that are determined for Stations 6 and 8 in Fig. 11, we begin to gain insights into the radiant energy dynamics of the two stations. Both near the surface (at a 30-m depth) and at greater depths (80 m or more) the absorption anomalies are somewhat greater than that predicted for water Raman scattering alone. Small amounts of yellow substance and algal-type particles are present (Table I) and can thus be contributing fluorescence to the basic water Raman scattering. The layering of the absorption anomaly for Station 6 is evidence for fluorescence from algal-type particles. Both stations show an overall tendency to have the absorption anomaly increase with depth as would be expected for a fundamental background of water Raman scattering for the internal radiant emission. With greater knowledge of quantum yields for the fluorescence of dissolved organics[51] and the algal component,[22,52,53] it will be possible to partition the internal emission among its components. For the present we have a method for assessing the quantitative contribution of all internal radiant emission sources to the submarine light field.

References

1. R. H. Stavn and A. D. Weidemann, "Raman scattering effects in ocean optics," in Ocean Optics IX, M. A. Blizard, ed., Proc. Soc. Photo-Opt. Instrum. Eng. **925,** 131–139 (1988).
2. R. H. Stavn and A. D. Weidemann, "Optical modeling of clear ocean light fields: Raman scattering effects," Appl. Opt. **27,** 4002–4010 (1988).
3. B. R. Marshall, "Raman scattering in ocean water," M.S. thesis. Department of Geography, University of California (Santa Barbara, Santa Barbara, Calif., 1989).
4. B. R. Marshall and R. C. Smith, "Raman scattering and in-water optical properties," Appl. Opt. **29,** 71–84 (1990).
5. S. Sugihara, M. Kishino, and M. Okami, "Contribution of Raman scattering to upward irradiance in the sea," J. Oceanogr. Soc. J. **40,** 397–404 (1984).
6. E. Aas, "The absorption coefficient of clear ocean water," Rep. 67 (December Institutt for Geofysikk, University of Oslo, 1987).
7. L. Prieur and S. Sathyendranath, "An optical classification of coastal and oceanic waters based on the specific spectral absorption curves of phytoplankton pigments, dissolved organic matter, and other particulate materials," Limnol. Oceanogr. **26,** 671–689 (1981).
8. D. Spitzer and M. R. Wernand, "In situ measurements of absorption spectra in the sea," Deep Sea Res. **28A,** 165–174 (1981).
9. D. Spitzer, M. R. Wernand, and G. C. Cadée, "Optical measurements in the Gulf of Guinea. Some aspects of remote sensing," Oceanol. Acta **5,** 41–47 (1982).
10. D. A. Siegel and T. D. Dickey, "Observations of the vertical structure of the diffuse attenuation coefficient spectrum," Deep Sea Res. **34A,** 547–563 (1987).
11. J. C. Kitchen and H. Pak, "Observations of natural fluorescence with an underwater radiometer," J. Oceanogr. Soc. Jpn. **43,** 356–362 (1987).
12. B. J. Topliss, "Optical measurements in the Sargasso Sea: solar stimulated chlorophyll fluorescence," Oceanol. Acta **8,** 263–270 (1985).
13. R. C. Smith and K. S. Baker, "Optical properties of the clearest natural waters (200–800 nm)," Appl. Opt. **20,** 177–184 (1981).
14. D. A. Siegel and T. D. Dickey, "On the parameterization of irradiance for open ocean photoprocesses," J. Geophys. Res. **92,** 14,648–14,662 (1987).
15. S. Sathyendranath and T. Platt, "The spectral irradiance field at the surface and in the interior of the ocean: a model for applications in oceanography and remote sensing," J. Geophys. Res. **93,** 9270–9280 (1988).
16. D. Spitzer and R. W. J. Dirks, "Contamination of the reflectance of natural waters by solar-induced fluorescence of dissolved organic matter," Appl. Opt. **24,** 444–445 (1985).
17. M. Bristow, D. Nielsen, D. Bundy, and R. Furtek, "Use of water Raman emission to correct airborne laser fluorosensor data for effects of water optical attenuation," Appl. Opt. **20,** 2889–2906 (1981).
18. F. E. Hoge and R. N. Swift, "Delineation of estuarine fronts in the German bight using airborne laser-induced water Raman backscatter and fluorescence of water column constituents," Int. J. Remote Sensing **3,** 475–495 (1982).
19. E. D. Traganza, "Fluorescence excitation and emission spectra

of dissolved organic matter in sea water," Bull. Mar. Sci. **19**, 897–904 (1969).

20. K. Carder, R. G. Steward, G. R. Harvey, and P. B. Ortner, "Marine humic and fulvic acids: their effects on remote sensing of ocean chlorophyll," Limnol. Oceanogr. **34**, 68–81 (1989).

21. C. M. Yentsch and C. S. Yentsch, "Emergence of optical instrumentation for measuring biological properties," Oceanogr. Mar. Biol. Ann. Rev. **22**, 55–98 (1984).

22. B. G. Mitchell and D. A. Kiefer, "Determination of absorption and fluorescence excitation spectra for phytoplankton," in *Fixation and Cycling of Carbon in the Marine Environment,* O. Holm-Hansen, ed. (Springer-Verlag, Berlin, 1984).

23. H. R. Gordon, "Diffuse reflectance of the ocean: the theory of its augmentation of chlorophyll *a* fluorescence at 685 nm," Appl. Opt. **18**, 1161–1166 (1979).

24. K. L. Carder, R. G. Steward, and T. G. Peacock, "Spectral transmissometer and radiometer (STAR): preliminary results," Eos Trans. Am. Geophys. Union **68**, 1683 (1987).

25. K. L. Carder, R. G. Steward, T. G. Peacock, P. R. Payne, and W. Peck, "Spectral transmissometer and radiometer: design and initial results," in *Ocean Optics IX,* M. A. Blizard, ed., Proc. Soc. Photo-Opt. Instrum. Eng. **925**, 189–195 (1988).

26. A. Gershun, "The light field," J. Math. Phys. **18**, 51–151 (1939).

27. N. K. Højerslev, "A spectral light absorption meter for measurements in the sea," Limnol. Oceanogr. **20**, 1024–1034 (1975).

28. R. H. Stavn, "The three-parameter model of the submarine light field: radiant energy absorption and trapping in nepheloid layers recalculated," J. Geophys. Res. **92**, 1934–1936 (1987).

29. G. Schellenberger, "Über Zusammenhänge zwischen optischen Parametern von Gerässern," Acta Hydrophys. **10**, 79–105 (1965).

30. J. T. O. Kirk, *Light and Photosynthesis in Aquatic Ecosystems* (Cambridge U. Press, Cambridge, 1983).

31. R. W. Preisendorfer, *Hydrologic Optics* (U.S. Government Printing Office, Washington, D.C., 1976).

32. R. H. Stavn, "Light attenuation in natural waters: Gershun's law. Lambert–Beer law, and the mean light path," Appl. Opt. **20**, 2326–2327 (1981).

33. G. N. Plass and G. W. Kattawar, "Monte Carlo calculations of radiative transfer in the Earth's atmosphere–ocean system: 1. Flux in the atmosphere and ocean," J. Phys. Oceanogr. **2**, 139–145 (1972).

34. H. R. Gordon and O. B. Brown, "Irradiance reflectivity of a flat ocean as a function of its optical properties," Appl. Opt. **12**, 1549–1551 (1973).

35. J. T. O. Kirk, "Monte Carlo procedure for simulating the penetration of light into natural waters," Division of Plant Industry Tech. Paper 36 (Commonwealth Scientific and Industrial Research Organization, Canberra, Australia, 1981).

36. A. C. Tam and C. K. N. Patel, "Optical absorption of light and heavy water by laser optoacoustic spectroscopy," Appl. Opt. **18**, 3348–3358 (1979).

37. T. G. Peacock, K. L. Carder, C. O. Davis, and R. G. Steward, "Effects of fluorescence and water Raman scattering on models of remote sensing reflectance," in *Ocean Optics X,* R. W.

Spinrad, ed., Proc. Soc. Photo-Opt. Instrum. Eng. **1302**, 303–319 (1990).

38. A. Morel, "Optical properties of pure water and pure sea water," in *Optical Aspects of Oceanography,* N. G. Jerlov and E. S. Steemann Nielsen, eds. (Academic, London, 1974).

39. G. Kullenberg, "Scattering of light by Sargasso Sea water," Deep Sea Res. **15**, 423–432 (1968).

40. H. R. Gordon, O. B. Brown, and M. M. Jacobs, "Computed relationships between the inherent and apparent optical properties of a flat homogeneous ocean," Appl. Opt. **14**, 417–427 (1975).

41. C. H. Chang and L. A. Young, "Seawater temperature measurement from Raman spectra," Research Note 920, N62269-72-0204, ARPA Order 1911 (Advanced Research Projects Agency, Washington, D.C., July 1972).

42. M. Iqbal, *Solar Radiation* (Academic, New York, 1984).

43. A. W. Harrison and C. A. Coombes, "Angular distribution of clear sky short wavelength radiance," Sol. Energy **40**, 57–63 (1988).

44. J. T. O. Kirk, "Yellow substance (gelbstoff) and its contribution to the attenuation of photosynthetically active radiation in some inland and coastal south-eastern Australian waters," Aust. J. Mar. Freshwater Res. **27**, 61–71 (1976).

45. O. V. Kopelevich and V. I. Burenkov, "Relation between the spectral values of the light absorption coefficients of sea water, phytoplanktonic pigments, and the yellow substance," Oceanology **17**, 278–282 (1977).

46. B. G. Mitchell, "Algorithms for determining the absorption coefficient of aquatic particulates using the quantitative filter technique (QFT)," in *Ocean Optics X,* R. W. Spinrad, ed., Proc. Soc. Photo-Opt. Instrum. Eng. **1302**, 137–148 (1990).

47. R. M. Pope, E. S. Fry, R. L. Montgomery, and F. M. Sogandares, "Integrating cavity absorption meter: measurement results, in *Ocean Optics X,* R. W. Spinrad, ed., Proc. Soc. Photo-Opt. Instrum. Eng. **1302**, 165–175 (1990).

48. C. C. Trees and K. J. Voss, "Optoacoustic spectroscopy and its application to molecular and particle absorption," in *Ocean Optics X,* R. W. Spinrad, ed., Proc. Soc. Photo-Opt. Instrum. Eng. **1302**, 149–156 (1990).

49. J. R. V. Zaneveld, R. Bartz, and J. C. Kitchen, "Calibration and error correction for a reflective tube absorption meter," in *Ocean Optics X,* R. W. Spinard, ed., Proc. Soc. Photo-Opt. Instrum. Eng. **1302**, 124–136 (1990).

50. J. S. Cleveland, "Spectral absorption coefficients measured with an integrating cavity absorption meter," in *Ocean Optics X,* R. W. Spinrad, ed., Proc. Soc. Photo-Opt. Instrum. Eng. **1302**, 176–186 (1990).

51. S. K. Hawes and K. L. Carder, "Fluorescence quantum yields of marine humic and fulvic acids: application for *in situ* determination," Eos Trans. Am. Geophys. Union **71**, 136 (1990).

52. C. H. Mazel, "Spectral transformation of downwelling radiation by autofluorescent organisms in the sea," in *Ocean Optics X,* R. W. Spinrad, ed., Proc. Soc. Photo-Opt. Instrum. Eng. **1302**, 302–327 (1990).

53. L. P. Shapiro, E. M. Haugen, and E. J. Carpenter, "Occurrence and abundance of green-fluorescing dinoflagellates in surface waters of the Northwest Atlantic and Northeast Pacific Oceans," J. Phycol. **25**, 189–191 (1989).

Effects of Raman scattering across the visible spectrum in clear ocean water: a Monte Carlo study

Robert Hans Stavn

Raman-scattering activity in clear ocean waters is documented for the visible spectrum from Monte Carlo simulations. The Raman-scattering activity has a significant effect on the upwelling irradiance value in air and on the submarine light field at the water surface across the visible spectrum. A reduction in Raman-scattering activity at 440 nm that is due to Fraunhofer lines at the Raman source wavelengths is also demonstrated. At wavelengths greater than 500 nm, Raman scattering makes a significant contribution to the in-water light field at depth.

Key words: Raman scattering, ocean optics, remote-sensing reflectance, in-water optical properties, Fraunhofer lines.

Introduction

The reality of the occurrence of water Raman scattering in clear ocean waters has been established by Stavn and Weidemann[1,2] and Marshall and Smith[3,4] after the strong implications of its presence were reported by Sugihara *et al.*[5] Stavn and Weidemann used field results and Monte Carlo simulations of the radiative-transfer equation to establish the water Raman-scattering phenomenon at 520 nm, and Marshall and Smith used field results and a modified two-flow model to establish it at 589 nm. Thus there is now a need developing for accurate information on the transpectral scattering properties of the water molecule for studies of ocean optics. This Raman-scattering phenomenon results from the thermal vibrational properties of the water molecule, in which energy can be abstracted from a photon to put the molecule into a specific vibrational mode of OH stretching and bending.[6] The photon is then emitted at a longer wavelength in this Stokes-shifted mode. Anti-Stokes-shifted modes are also possible but of low probability at the ambient temperatures of the world's oceans.

Is the water Raman-scattering phenomenon significant for the shorter (blue) and longer (red) wavelengths of the visible spectrum? Certainly the inso-

The author is with the Department of Biology, University of North Carolina, Greensboro, North Carolina 27412.

lation of the sea surface is rich in the blue and ultraviolet (UV) wavelengths, and thus the surface layers at least are rich in these wavelengths. Indeed there is concern about possible increases in the UV portion of the insolation as a result of reduction in the ozone layer[7] and about the effects of these increases on biological productivity, etc., in the surface layers. Water Raman scattering follows a λ^{-4} law, and thus there would be relatively greater production of water Raman photons at shorter wavelengths. We have at least the potential of significant effects at the shorter wavelengths. This same law would imply relatively fewer water Raman photons at longer wavelengths, and we want to see if the phenomenon can still be significant at those wavelengths. Many remote-sensing algorithms require a region in the red (approximately 670 nm) where the water-leaving radiance or irradiance is essentially zero.[8] The possibility of water Raman-scattering activity here is certainly relevant. Furthermore, a water Raman baseline is needed for the eventual evaluation in passive remote sensing of the contribution to the upwelling irradiant flux of fluorescence from the chlorophyll a,[9] intracellular pigments,[10] and dissolved organic matter[11,12] at various points in the visible waveband. Certainly the Raman-scattering phenomenon has been used for a long time to normalize the fluorescence signals received from active remote sensing by lidar.[13] Therefore fundamental baselines of Raman-scattering activity across the entire visible spectrum are needed for evaluation and interpretation of remote-

sensing algorithms, models of photon penetration, etc.

The present paper uses the Monte Carlo simulation of the radiative-transfer equation as a controlled experiment in observing the photon penetration of the clear, oligotrophic ocean, as has been stated by Gordon.[14] The validity of the simulation method has been established from comparison of the Naval Research Laboratory (NRL) Monte Carlo output with actual ocean data.[1,2] With the input of the recognized optical parameters of the marine hydrosol, the NRL optical model can generate separate solar and water Raman photon streams for analysis. Combining the separate photon streams then gives us insight into the effects of water Raman scattering on the submarine light field and may allow a more accurate series of algorithms for inverting the inherent optical properties of the marine hydrosol from the irradiance field.

Method

The NRL optical model is a Monte Carlo simulation of the radiative-transfer equation that describes the penetration of solar photons into ocean waters. This model also accounts for the transpectral water Raman scattering. The Monte Carlo simulation is derived from the methods of Plass and Kattawar,[15] Gordon and Brown,[16] and Kirk.[17] Required inputs for simulating the penetration and fate of solar photons in ocean waters are the absorption coefficient, the total scattering coefficient, and the volume scattering function of the marine hydrosol. The volume scattering functions of each scattering component (molecular water, quartzlike particulates, algae, organic detritus) are treated separately rather than using an average volume scattering function. The NRL blue water model used in this simulation contains the absorption coefficients for molecular water reported by Smith and Baker[18] up to 570 nm; the coefficients reported by Tam and Patel[18] are used at wavelengths greater than 570 nm. Recent investigations of the backscattered upwelling radiance from ocean waters indicate that this is the most efficient combination of absorption coefficients.[20] The total scattering coefficient and the volume scattering function of pure seawater are incorporated from Morel,[21] the total scattering coefficient for quartzlike material is from Kullenberg,[22] and the volume scattering function is incorporated from the Petzold[23] "Tongue of the Ocean," Bahamas distribution corrected for molecular water.[21] There are no other hydrosol components assumed in the blue water model.

To simulate the genesis and fate of the photons transpectrally scattered from the water molecule, its Raman-scattering coefficient was calculated from the molecular Raman-scattering cross section reported by Marshall and Smith[4] and from the depolarization ratios reported by Murphy and Bernstein.[24] The Raman-scattering coefficient was then truncated to generate only emissions in the 10-nm waveband surrounding the emission wavelength studied, as described earlier.[1] Because the frequency shift of water Raman emission from a line source at any wavelength occurs approximately in the range from 2900 to 3700 cm^{-1}, it is practical and convenient to divide the relatively broad Raman emission band into three bands of 10-nm bandwidth: a midband, an upper band, and a lower band. The emission in the midband will dominate at shorter wavelengths, and more emission is distributed among the upper and lower bands at longer wavelengths. The midband represents a frequency shift centered at approximately 3357 cm^{-1},[5] the upper band represents a frequency shift centered at approximately 3500 cm^{-1}, and the lower band represents a frequency shift centered at approximately 3150 cm^{-1}. The different frequency shifts involved with the varying sources to the reference emission waveband require different Raman-scattering coefficients for each waveband. These calculations were done separately for each waveband investigated here.

The primary source waveband for the water Raman emissions at a given waveband is determined by calculation based on the 3357-cm^{-1} frequency shift. The other sources for the 10-nm Raman emission band come from two 10-nm wavebands, one above and one below the main source waveband. Water Raman-scattering coefficients appropriate to the frequency shift from the upper and lower source wavelengths are then applied to determine the contributions of these wavebands to the emission waveband being studied. A new feature incorporated into the NRL optical model is the variations in the phase function for Raman scattering. The depolarization ratio varies across the Raman emission band. A high depolarization ratio, as found for the 3500-cm^{-1} frequency shift, yields a higher water Raman-scattering coefficient with a phase function approaching the spherical in shape. A low depolarization ratio, as found for the 3150-cm^{-1} frequency shift, yields a lower water Raman-scattering coefficient with a phase function approaching the classic dumbbell shape.[3] Each source wavelength feeding into the defined water Raman emission band therefore generated a different phase function at the emission band depending on the average depolarization ratio for that Raman emission band. The phase functions were determined with the relations reported by Marshall[3] and Schrötter and Klöckner.[25] This attention to what is happening in narrowly defined wavebands allows an accurate assessment of the generation of water Raman emission from a spectrally varying solar source interacting with a marine hydrosol of spectrally varying optical properties.

The simulations for Raman emission wavelengths were performed at 430, 440, 470, 490, 510, 520, 550, 589, 620, 640, and 660 nm. These wavelengths were chosen to span most of the regions of greatest optical activity, etc., of the marine hydrosol and to correspond with wavelengths actively being studied by many groups, including NRL. For each emission wavelength three Raman source wavelengths were

calculated by methods described below. At greater wavelengths we encounter the regions known to be strongly affected by chlorophyll fluorescence.

For a simulation run, photons are transported through a clear atmosphere containing a marine aerosol for both a Raman emission wavelength and the three Raman source wavelengths. The determination of the Raman source wavelengths for the emission wavelength is made on the basis of the frequency shifts discussed previously. The relative numbers of photons propagated at the three source wavebands and the one emission waveband are determined from the extraterrestrial solar irradiance spectrum reported by Iqbal.[26] The atmospheric model of Iqbal is then used to propagate solar and sky-light photons through the marine aerosol to sea level. The parameters assumed for these calculations were Ångström's wavelength exponent and turbidity coefficient $\alpha = 0.7$ and $\beta = 0.206$, ozone concentration of 0.33 cm atm, aerosol single-scattering albedo of $\omega_0 = 0.9$, and the effective forward-scattering function of the aerosol $F_a = 0.923$. Iqbal's model allows the calculation of the irradiance at sea level that is due to propagation through the solar beam and propagation through sky light. Once the percentile of the sea-level irradiance propagated through sky light is known, the sky-light radiance distribution of Harrison and Coombes[27] can be applied. This sky-light radiance distribution is normalized to the irradiance at the earth's surface that is due to sky light. The angle of entry of a sky-light photon is determined from the Harrison and Coombes distribution, whereas the entry angle of a solar photon is at $11°$ from the zenith. The sea surface is flat. At the air–water interface the photon will either enter the ocean and be refracted or be reflected back into the air based on the laws of Fresnel and Snell. These laws determine the probabilities of these events that are chosen by a random number generator. On entry into the ocean a photon can be absorbed, scattered, or transpectrally scattered. The probabilities of these events are determined from the respective coefficients of the model, the individual events are chosen by a random number generator. The absorption of a photon automatically generates a new one that propagates through the system until 2.5×10^6 photons have been propagated. Counters set up at regular depth intervals sum up the photons passing through that interval, and thus their sums are directly proportional to radiances and irradiances as they would be measured by a photometer. Duplicate runs are made for the wavelength studied. All values of simulated irradiant flux reported here are averages over the duplicate runs, and the standard error of the mean values is also reported.

From the simulated irradiant-flux values it is possible to calculate the standard apparent optical properties of the submarine light field such as the irradiance ratio, R. In addition, it is possible to estimate the water Raman percentile of the scalar-irradiance field by applying the method of the absorption coeffi-

cient anomaly, which is applicable to field data, as proposed by Stavn and Weidemann[2]

$$\frac{\Delta a(z)}{a(z)} \cong \frac{E_o{}^*(z)}{[E_o(z) + E_o{}^*(z)]}, \tag{1}$$

where $\Delta a(z)/a(z)$ is the absorption coefficient anomaly at depth z, $E_o{}^*(z)$ is the scalar irradiance that is due to water Raman photons at that depth, and $E_o(z)$ is the scalar irradiance that is due to solar photons at that depth. The numerator of the absorption coefficient anomaly is the difference between the absorption coefficient calculated from a nonconservative photic field [Eq. (2), below] and the actual absorption coefficient of the hydrosol. Either we know the actual absorption coefficient already (as in the case of this simulation) or we would measure it in a properly designed spectrophotometer. The nonconservative absorption coefficient is calculated from the nonconservative irradiance field by Gershun's equation,[2]

$$\tilde{a}(z) = -\frac{1}{[E_o(z) + E_o{}^*(z)]} \frac{d[E_z(z) + E_z{}^*(z)]}{dz}, \tag{2}$$

where $E_z = E_d - E_u$ is the net downwelling irradiance or downwelling vector irradiance for solar photons, $E_z{}^*(z)$ is the net downwelling irradiance from water Raman photons, and $\tilde{a}(z)$ is the nonconservative absorption coefficient. The numerator in this calculation approaches zero as the photic field becomes dominated by internal photon emission, and thus the calculation of Eq. (1) then approaches 1.0.

Results

First we examine the results from the portion of the simulated irradiance field that is most sensitive to the effects of water Raman scattering: the upwelling irradiance field, E_u. Figure 1 shows the logarithm of the upwelling irradiances, at selected wavelengths, derived from the separate streams of solar photons and water Raman photons, and the combined stream as an irradiance meter would read them. Two major points emerge. The absolute number of upwelling Raman photons increases with a decrease in wavelength. The apparent decay rate of water Raman photons with depth remains nearly constant across the spectrum, whereas that of the solar photons increases markedly with wavelength. In the region 430–490 nm there is either a small Raman contribution to the total upwelling photons at the surface only or a relatively small and constant Raman contribution with depth [see Figs. 1(a) and 1(b)]. In the region 510–589 nm, the upwelling irradiance field is composed of 50% Raman photons (i.e., the Raman and solar curves intersect) at depths ranging from 105 to 19 m with increase in wavelength (Fig. 2). In the region 620–660 nm, the upwelling irradiance field is composed of 50% Raman photons at depths ranging from 8.5 to 6.5 m with increase of wavelength (Fig. 2).

The contribution of Raman photons to the total photic field is also significant. Consider the percen-
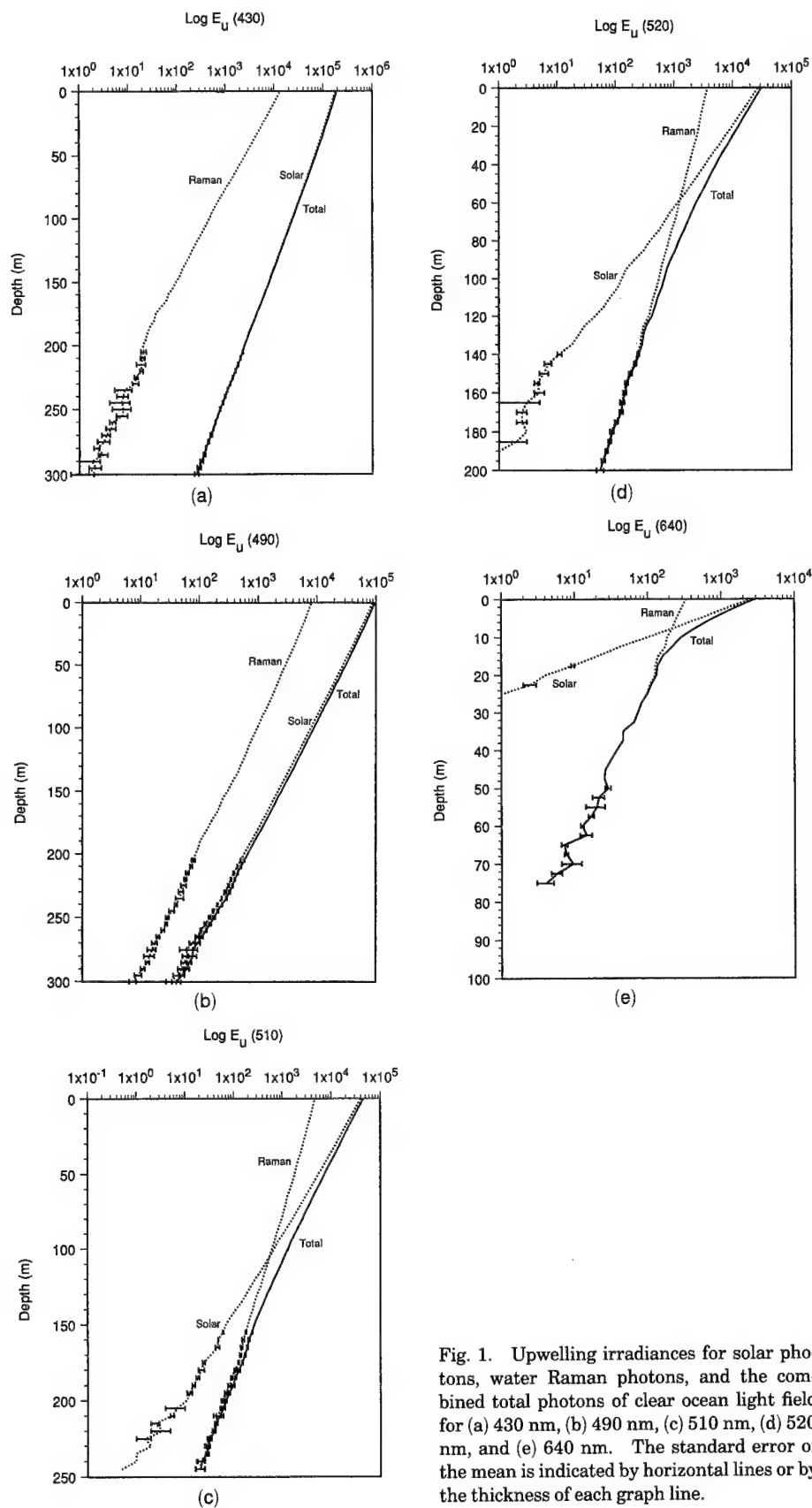
Fig. 1. Upwelling irradiances for solar photons, water Raman photons, and the combined total photons of clear ocean light field for (a) 430 nm, (b) 490 nm, (c) 510 nm, (d) 520 nm, and (e) 640 nm. The standard error of the mean is indicated by horizontal lines or by the thickness of each graph line.
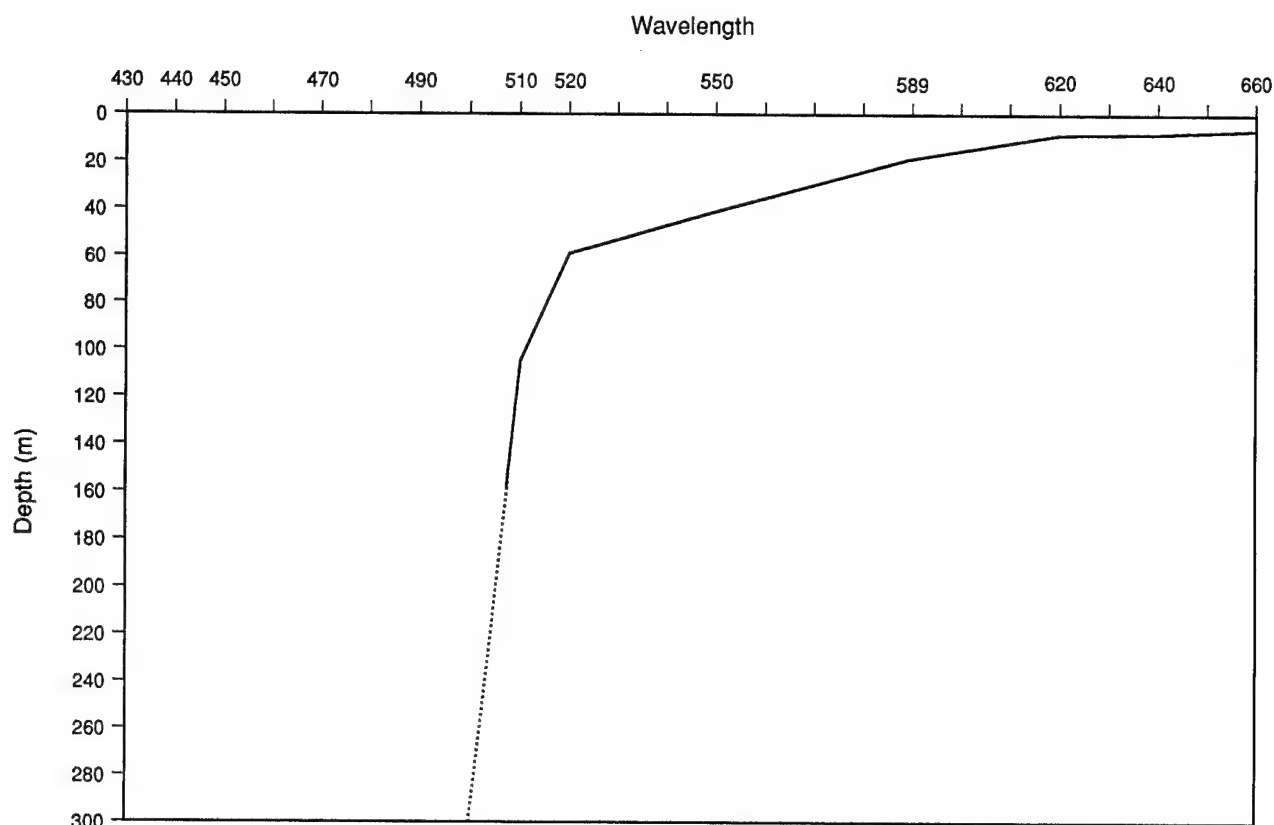
Wavelength

Fig. 2. Depth at which the upwelling irradiance field is composed of 50% Raman photons across the visible spectrum. Extrapolation of data at 490 nm (dotted line) would indicate that this condition may occur at 600 m. Wavelengths less than 490 nm would apparently never reach this condition.

tile of the scalar irradiance, E_o, that is contributed by Raman photons across the spectrum. Table 1 indicates the percentile contribution of Raman photons just beneath the surface at 0 m depth, which is a good index of the total water Raman-scattering activity for a given wavelength. The maximum contribution from water Raman scattering comes at 430 nm, where it amounts to 1.7% of the scalar irradiance. The percentile contribution drops steadily with wavelength to 660 nm, where it amounts to 0.043% of the scalar irradiance. The only exception is at 440 nm, where the percentile contribution from water Raman-scattering is less than at 470 nm. The percentile contribution of water Raman photons to the spectral scalar irradiance with depth is in Fig. 3, where the pattern is decidedly different. At 430 nm the contribution of water Raman scattering to the total photic field at depth is nearly inconsequential [Fig. 3(a)], whereas at 490 nm there is a small and nearly constant contribution of water Raman photons with depth [Fig. 3(b)]. A transition occurs as we continue to 510 nm, where the Raman percentile eventually

increases to 33% of the scalar-irradiance field at 200 m [Fig. 3(c)]. At 520 nm the Raman contribution to the total photic field is 50% at approximately 140 m [Fig. 3(d)]. Around 600 nm we have another transition region where the Raman contribution becomes important in the near-surface layers. Thus at 640 nm the depth of the 50% contribution of Raman photons to the scalar irradiance decreases to approximately 28 m [Fig. 3(e)].

The light-field property in these simulations that is of greatest interest to remote sensing and many light-field parameterizations is the spectral-irradiance ratio, R, which is the ratio of the upwelling irradiance to the downwelling irradiance, E_u/E_d. Figure 4 plots the spectral R values for the backscattered portion of the directly transmitted solar photons and also the spectral R values for the total photons, backscattered solar plus upwelling Raman. At 430 nm the R value for total upwelling photons is significantly affected by the water Raman component only in the surface layers; the effect decreases with depth to inconsequential levels [Fig. 4(a)]. At 490

Table 1. Percentile Raman Contribution to Scalar Irradiance: Just Beneath Surface

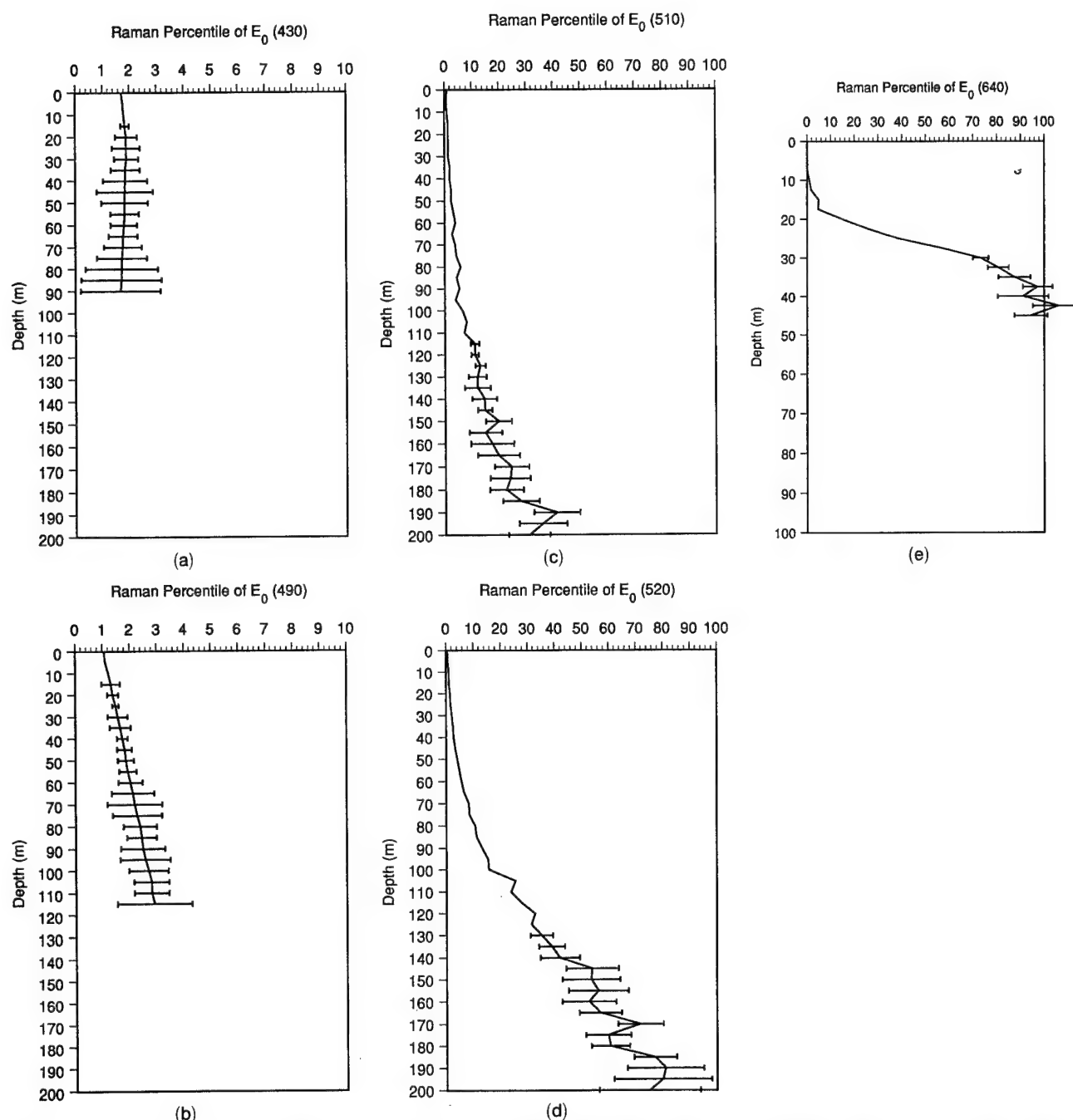| Emission Wavelength (nm)										
430	440	470	490	510	520	550	589	620	640	660
1.7084	1.0991	1.2247	1.0767	0.5727	0.5471	0.3765	0.1890	0.0757	0.0661	0.0437

Fig. 3. Percentile contribution of water Raman photons to total light field (scalar irradiance) with depth in clear ocean water at (a) 430 nm, (b) 490 nm, (c) 510 nm, (d) 520 nm, and (e) 640 nm. Note that the percentile scale goes to a maximum of 10% for (a) and (b) and a maximum of 100% for (c)–(e). The smaller percentile is necessary for the shorter wavelengths to make their Raman contributions discernible.

nm the Raman contribution to R for total upwelling photons becomes noticeable at greater depths [Fig. 4(b)]. In this general region of blue to blue–green, the R value for total photons appears to be nearly constant with depth, whereas the R value for solar photons alone tends to increase with depth. In the region 510–520 nm the R value starts to show a tendency to increase beyond the accepted values for R in a conservative system with small backscattering coefficients [Figs. 4(c) and 4(d)]. At 640 nm the dramatic increase in R for total photons occurs at

very shallow depths [Fig. 4(e)]. In general, the effects of water Raman scattering on the in-water R value are significant only in the surface layers at wavelengths below 470 nm, whereas the effects become dramatic with depth for wavelengths greater than 510 nm.

To illuminate the possibilities for the effects of water Raman scattering on the remotely detected (by satellite or aircraft) spectral upwelling irradiance in air, the spectral R_{o+} values (Morel's definition[28]) are plotted in Fig. 5. At 430 nm the Raman contribution
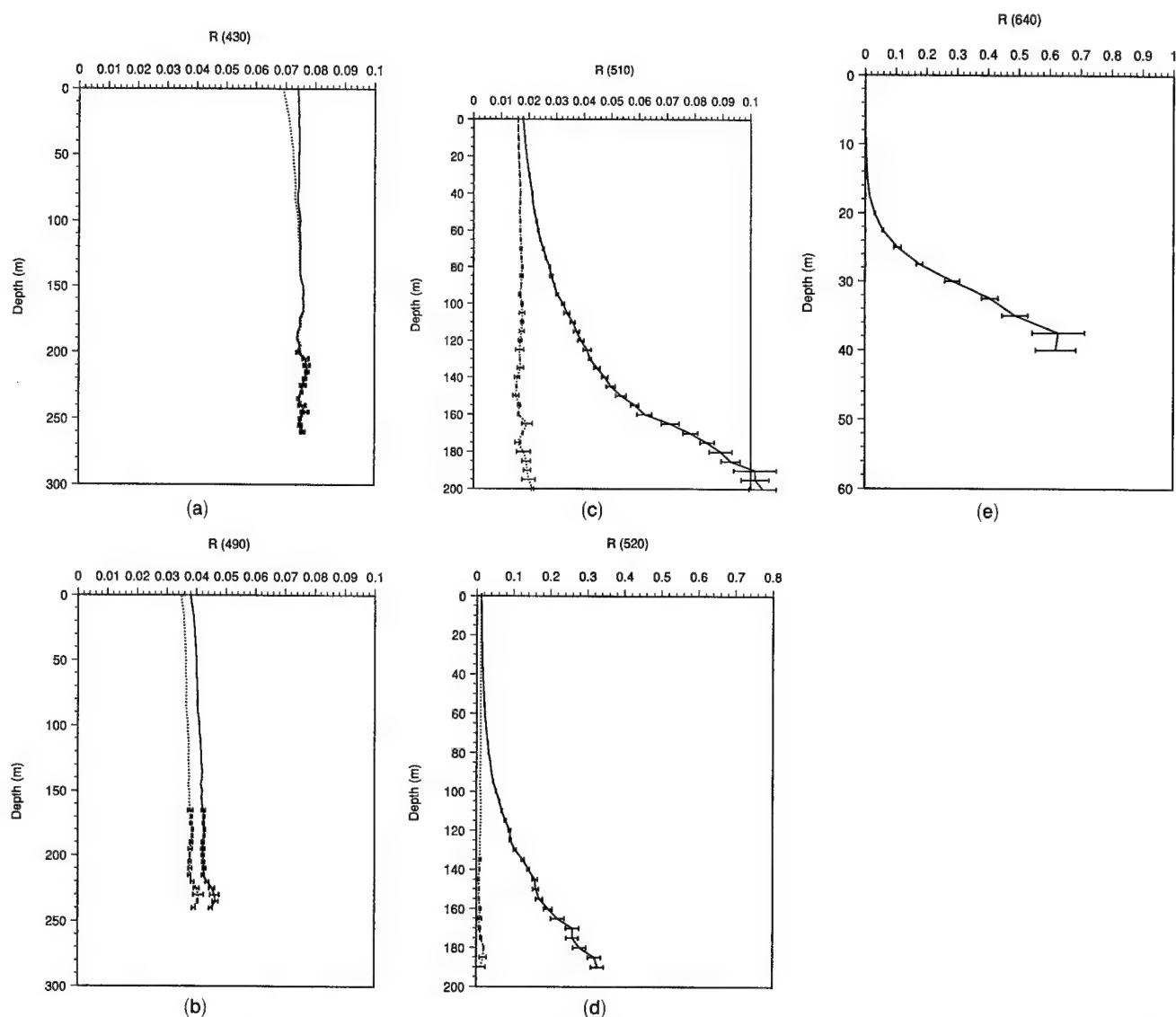
Fig. 4.   Irradiance ratios of clear ocean light field with depth for solar photons alone and total (solar + Raman) photons at (a) 430 nm, (b) 490 nm, (c) 510 nm, (d) 520 nm, and (e) 640 nm.   Note that the R value has a maximum of 0.1 for (a)–(c), 0.8 for (d), and 1.0 for (e).

to the R_{o+} value in air is 6% with approximately a 1% drop in Raman contribution at 440 nm.   The Raman contribution steadily increases to 550 nm, where it is approximately 15% of the total R_{o+} value.   Beyond 550 nm the Raman contribution to the R_{o+} value drops slightly and holds more or less steadily to 660 nm, where it is approximately 13% of the R_{o+} value.

Clear Ocean Radiant Flux Field: Raman Contributions across the Spectrum

Consider now the mechanisms behind the observations from the Monte Carlo output and the implications of these mechanisms for future research and algorithms in ocean optics.

We have amassed considerable evidence for the contribution of water Raman scattering to the photic field of clear ocean waters.   For example, the percentile contributions of water Raman photons to the scalar irradiance at 0 m depth, just beneath the surface, are documented in Table 1.   The scalar irradiance at zero depth is a good indicator of the water Raman-scattering activity in the photic field. Here we are receiving the transpectrally scattered photons from the maximum possible source at the surface plus the water Raman photons integrated from all depths below the surface.   The greatest absolute contribution of water Raman photons is at 430 nm, and this decreases regularly with an increase in wavelength.   Given the nearly constant or at least comparable numbers of solar photons across the spectrum that are present in the surface layers,[29] and the λ^{-4} relation for the generation of water Raman photons, this result is not surprising.   However, the spectral trend in the percentage of water Raman photons at the surface does not follow this power law but rather exhibits a smaller slope at the shorter wavelengths and a greater slope at the longer wavelengths.   This result indicates that multiple elastic
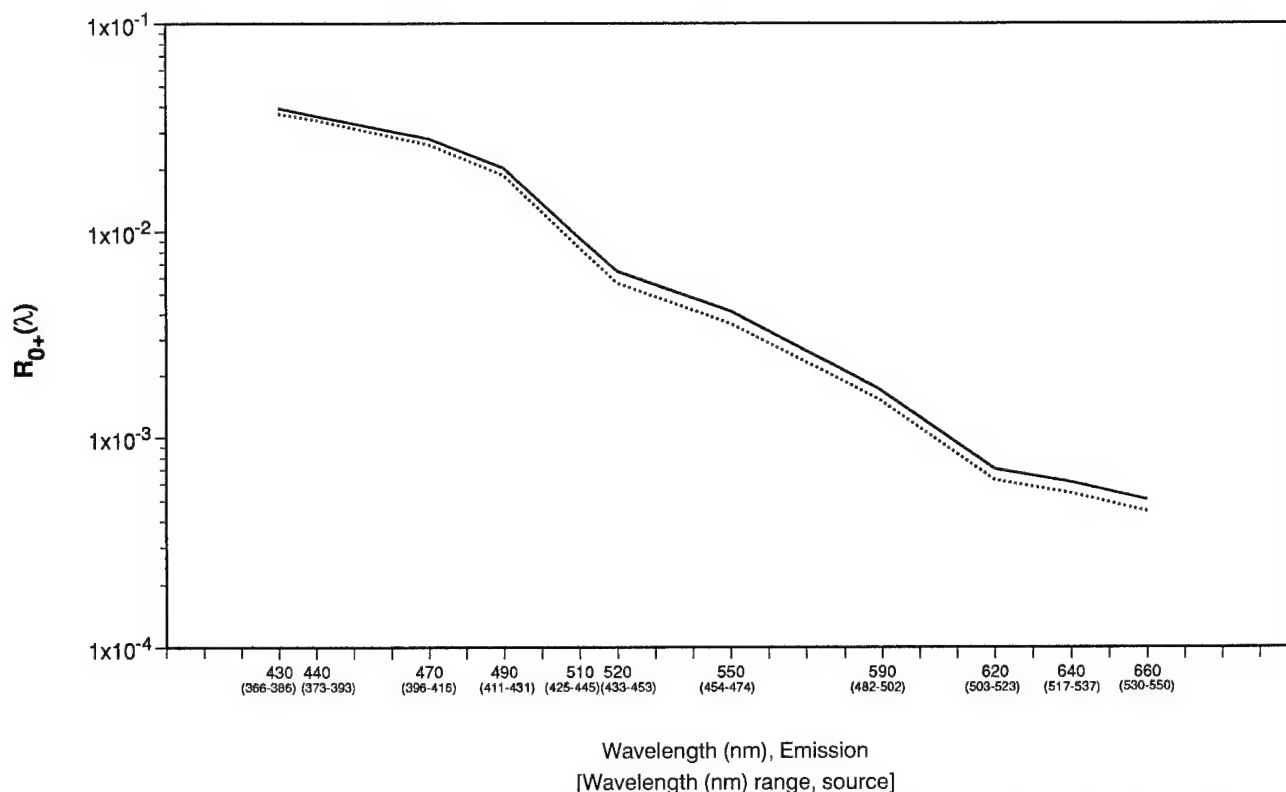
Fig. 5. Irradiance ratios in air caused by emergent radiant flux from clear ocean water, flat surface: solar photons alone (dotted curve) and total (solar + Raman) photons (solid curve).

scattering and multiple interreflections off the interface are concentrating the water Raman photons, at the shorter wavelengths, in the process called optical energy trapping.[30,31] In addition, there is a slight drop in the percentage of water Raman photons at 440 nm that can be explained as a result of Fraunhofer line effects in the insolation. The major source of Raman photons emitted at 440 nm is the solar photons in the wavelength region of approximately 368 to 398 nm. There are significant decreases in the flux of solar photons in this region relative to adjacent wavebands because strong Fraunhofer lines: the N, M, and L lines for Fe, and the K and H lines for Ca. This Fraunhofer line effect shows up for other photic field properties at 440 nm.

Obviously the significance of the effect of water Raman photons on the irradiances, etc., of the submarine light field is not just a function of the absolute production of Raman photons. Also we have to consider that the absorption coefficient of the marine hydrosol varies spectrally: at longer wavelengths the absorption is relatively high and is due essentially to the water molecule. That is, we cannot consider just the production of water Raman photons; we must also consider their differential removal relative to the more-or-less overwhelming stream of solar photons. The water Raman-scattering coefficient is approximately one tenth the magnitude of the elastic-fluctuation scattering coefficient of the water molecule[4] and thus has the potential to contribute photons to the field at the emission wavelength. However, if the hydrosol absorption coefficient is relatively large at the emission wavelength and a significant amount of solar photons is removed, the potential contribution of water Raman photons to the photic field at the emission wavelength could be considerable. Assuming again that the number of photons from insolation is comparable across most of the visible spectrum, we can analyze a simple ratio of the absorption coefficients for the hydrosol to predict the probable significance of water Raman scattering. Table 2 lists, as the Raman emission wavelengths, the ratio of the hydrosol absorption coefficient at the Raman emission wavelength to the hydrosol absorption coefficient at the source wavelength. The absorption coefficient at the source wavelength is a weighted average

Table 2. Absorption Coefficient Ratio[a]

Emission Wavelength (nm)										
430	440	470	490	510	520	550	589	620	640	660
0.5437	0.6619	0.9322	1.2829	2.4585	3.2860	4.1041	6.0579	7.6966	6.4383	6.7544

[a][absorption coefficient (emission λ)/weighted absorption coefficient (source λs)].

of the absorption coefficients of the hydrosol at the three wavebands contributing Raman photons to the emission waveband. The weighting function for the three source absorption coefficients is the Raman-scattering coefficient operating at that source waveband to produce Raman photons at the given emission waveband. The hydrosol of the oligotrophic ocean has an absorption coefficient that is due mostly to water. Thus the minimum of this absorption coefficient is at 430–450 nm, with increases in the coefficient both toward the blue end and the red end of the spectrum.

Thus there are three general regions of Raman effects in the open ocean based on both the increase of hydrosol absorption, relative to blue, toward the blue–UV and red regions, and the 55–100 nm wavelength shift for transpectrally scattered photons (see Table 2). In the region of 380–460 nm the absorption coefficient at the Raman source wavelength is greater than the absorption coefficient at the Raman emission wavelength; this greatly reduces the effects of water Raman scattering with depth. The absorption coefficient ratio of less than 1.0 in this region implies that the decay rate of the large flux of solar photons at the emission wavelength will be less than the net production rate of Raman photons. This large flux of solar photons at the emission wavelength will penetrate to great depths, whereas potential source photons for Raman scattering will decay at a greater rate and not penetrate deeply. The net production of Raman photons for the photic field at the emission wavelength will be less and less with depth. Thus the Raman photons will be a decreasing percentage of the total light field with depth and will have their strongest effect, if any, in the surface layers. In the region of 470–490 nm the hydrosol absorption coefficient at the Raman source wavelength is approximately equal to the absorption coefficient at the Raman emission wavelength, and the production of Raman photons should make a nearly constant, and small, proportion of the light field with depth at the emission wavelength. In the region of 490–660 nm the absorption coefficient at the source wavelength for Raman scattering is less than the absorption coefficient at the emission wavelength. This implies that the decay rate of the solar photons at the emission wavelength for Raman scattering will be much greater than the net production rate of Raman photons, because there will be a relatively large flux of potential source photons with depth. In this case we expect that the in-water effects of Raman scattering will be a dominant influence with depth as the solar photons are strongly removed and only Raman photons are left behind. The transition from predominantly surface effects of Raman scattering to a strong influence with depth occurs in the region of 490–510 nm. This trend should continue throughout the longer wavelengths of the visible spectrum.

How is the photic field affected at increasing depth by water Raman scattering, relative to the predictions made above? At wavelengths less than 470 nm, approaching the blue–violet end of the visible spectrum, the penetrating solar photons at the Raman source wavelengths are removed more rapidly than solar photons at the emission wavelengths. Thus from Figs. 1–3 it is apparent that the Raman emission effects are then masked by the relatively large amount of solar photons with depth at the emission wavelength. The Raman percentage of the total photons is small to inconsequential with depth, and the total upwelling irradiance field is dominated by solar photons. At 470–490 nm we have a transition region where the absorption coefficient ratio is approximately 1.0 (see Table 2), and the Raman emission has a small but steady effect as the light field penetrates the clear ocean hydrosol. Here the absorption of both potential Raman source photons and the solar photons at the emission wavelength is approximately equal. In the region greater than the 500-nm wavelength the Raman contributions to the total photic field and the upwelling irradiance increase rapidly with depth, the magnitude of the effect increasing with increasing wavelength. The upwelling irradiance is influenced more rapidly by Raman emission with depth than the scalar irradiance because the source of upwelling solar photons is the relatively small backscattering coefficient. As the wavelength increases the high hydrosol absorption at the emission wavelength (Table 2) rapidly removes solar photons, and the remaining Raman photons dominate the upwelling irradiance and the total photic field with increasing depth.

Certainly the irradiance ratio is the light-field parameter detectable by remote sensing of the upwelling irradiance transmitted through the water–air interface and is thereby worthy of consideration. Many algorithms attempt an inversion of the irradiance ratio, R, to determine the spatial distribution and concentration of the components of the hydrosol (e.g., chlorophyll). One empirical mode of inversion involves determining the irradiance ratios for different wavelengths and calculating the ratio of the different R values. Thus it is important to see if water Raman scattering will affect the R ratio. The irradiance ratio of solar photons at the blue end of the spectrum from Fig. 4 increases steadily with depth, whereas the addition of water Raman photons primarily at the surface causes the total in-water irradiance ratio to be nearly constant with depth. At wavelengths greater than 500 nm the relatively fast disappearance of solar photons with depth (predicted from Table 2) causes the irradiance ratio to increase with depth to values beyond the usual maxima for a system dominated by elastic scattering (approximately 10–15% for the open ocean). Morel[29] points out that this upwelling irradiance from the oceanic interactions represents approximately half of the total spectral updwelling-irradiance ratio detected remotely in the air, the rest of the upwelling-irradiance ratio in air coming from specularly reflected sun and sky light. The portion of the irradi-

ance ratios in air derived from the in-water upwelling flux, R_{o+}, (see Fig. 5) shows an augmentation by Raman photons at 430 nm that increases to a maximum at 550 nm. There is also a slight dip at 440 nm that is attributable to Fraunhofer line effects. Beyond 550 nm the augmentation is slightly less but remains nearly constant out to 660 nm. From Table 2 we see that the ratio of absorption coefficients for the hydrosol increases steeply up to the region of 550–589 nm, then tends to level off. Between 500 and 600 nm the hydrosol absorption coefficient at the Raman emission wavelength causes the rate of decay of the solar photons at that wavelength to increase faster than the drop-off of Raman photon production from the λ^{-4} relationship. Thus the increase in R_{o+} is attributable to upwelling Raman photons in this region of the visible spectrum. Beyond 600 nm the decay rate of solar photons appears to balance the decrease in Raman photon production for a given emission wavelength. The Raman photon production can also be augmented by multiple scattering and optical energy trapping of solar photons at the Raman source wavelength. The increase in the absorption coefficient with increase in wavelength is accompanied by a decrease in the scattering coefficient of the hydrosol, which implies less opportunity for multiple-scattering effects to occur at the emission wavelength. Thus a slightly reduced augmentation of R_{o+} beyond 600 nm.

In summary two major trends are at work in clear ocean water. There is a greater production of Raman photons at the blue end of the visible spectrum and a greater absorption of solar photons at the red end of the visible spectrum—how do these trends translate into the typical optical events of the oligotrophic ocean? At the shortwave end of the spectrum the production of Raman photons affects the submarine light field primarily at the surface. As depth increases, the production of Raman photons is masked by the relatively powerful solar photon stream at the Raman emission wavelength. As we approach the longwave end of the spectrum, Raman photons are produced in a region of relatively low marine hydrosol absorption, which allows significant production of Raman photons for relatively great depths of penetration. The wavelength shift of the Raman photons places them at a wavelength where the hydrosol removes solar photons quickly and the solar photon stream diminishes rapidly with depth. Under these conditions, the light field can become dominated by Raman photons at greater and greater depths. This occurs even though the absolute production of Raman photons decreases with increase in wavelength. The backscatter of downward-penetrating solar photons also diminishes with wavelength because it is primarily fluctuation theory (Rayleigh-type) scattering, whereas the increased absorption of solar photons diminishes further the magnitude of the backscattering and associated optical processes. Thus the upwelling irradiance in air has a significant Raman component that increases with wavelength.

The balance between the decrease in solar photons, the decrease in backscattering, and the lesser decrease in Raman photon production causes the Raman component to increase in its contribution to the irradiance ratio R until it peaks at 500 nm. These processes tend to be in balance to the extreme wavelength of this study, 660 nm, and the Raman contribution to R remains constant in this region.

These results have many important implications. It has often been reported that the in-water irradiance ratio R is constant for the wavelength region of 430–490 nm. It is evident here that this apparent constancy of R is probably an artifact resulting from water Raman-scattering effects at the surface. Multiple scattering of solar photons clearly dictates an increase in R with depth, and the augmentation of the upwelling irradiance by water Raman scattering at the surface creates this apparent constancy. Many remote-sensing algorithms rely on ratios of R at various key wavelengths for inverting concentrations of chlorophyll, etc., from these ratios. The contribution of water Raman scattering to the value of R in air will be variable depending on the absorption spectrum of these materials, and it is also variable itself across the visible spectrum, peaking at 550 nm. Additionally, the Raman contribution at 440 nm is reduced because the photon flux at the source wavelengths is reduced as a result of the presence of Fraunhofer lines at the source wavelengths. This spectral variation of the Raman contribution to R renders suspect the various ratioing schemes for remote sensing with R. The corruption of the upwelling signal by Raman scattering will dictate continual calibration of these algorithms with sea-truth data and restriction of certain algorithms to specific regions of the ocean until properly factoring in processes like Raman scattering. Thus far we have delineated major factors to consider in the effects of water Raman scattering on the optical properties of the oligotrophic ocean. Much remains to be done. The indications that optical energy trapping off the air–water interface may be of significance in concentrating Raman photons require simulations with a wave-disturbed interface. The interactions of sky light and solar zenith are also required. The possibility of water Raman windows in the water types up through the green coastal waters also remain to be explored.

References

1. R. H. Stavn and A. D. Weidemann, "Optical modeling of clear ocean light fields: Raman scattering effects," Appl. Opt. **27,** 4002–4010 (1988).

2. R. H. Stavn and A. D. Weidemann, "Raman scattering in ocean optics: quantitative assessment of internal radiant emission," Appl. Opt. **31,** 1294–1303 (1992).

3. B. R. Marshall, "Raman scattering in ocean water," M.S. thesis (Department of Geography, University of California, Santa Barbara, Santa Barbara, Calif., 1989).

4. B. R. Marshall and R. C. Smith, "Raman scattering and in-water optical properties," Appl. Opt. **29,** 71–84 (1990).

5. S. Sugihara, M. Kishino, and M. Okami, "Contribution of Raman scattering to upward irradiance in the sea," J. Oceanogr. Soc. Jpn. **40,** 397–404 (1984).

6. D. A. Long, *Raman Spectroscopy* (McGraw-Hill, New York, 1977), p. 276.

7. R. C. Smith and K. S. Baker, "Stratospheric ozone, middle ultraviolet radiation and phytoplankton productivity," Oceanography **2,** 4–10 (1989).

8. H. R. Gordon, "Diffuse reflectance of the ocean: influence of nonuniform phytoplankton pigment profile," Appl. Opt. **31,** 2116–2129 (1992).

9. H. R. Gordon, "Diffuse reflectance of the ocean: the theory of its augmentation by chlorophyll *a* fluorescence at 685 nm," Appl. Opt. **18,** 1161–1166 (1979).

10. C. H. Mazel, "Spectral transformation of downwelling radiation by autofluorescent organisms in the sea," in *Ocean Optics X,* R. W. Spinrad, ed., Proc. Soc. Photo-Opt. Instrum. Eng. **1302,** 320–327 (1990).

11. E. D. Traganza, "Fluorescence excitation and emission spectra of dissolved organic matter in sea water," Bull. Mar. Sci. **19,** 897–904 (1969).

12. K. Carder, R. G. Steward, G. R. Harvey, and P. B. Ortner, "Marine humic and fulvic acids: their effects on remote sensing of ocean chlorophyll," Limnol. Oceanogr. **34,** 68–81 (1989).

13. F. E. Hoge and R. N. Swift, "Delineation of estuarine fronts in the German Bight using airborne laser-induced water Raman backscatter and fluorescence of water column constituents," Int. J. Remote Sensing **3,** 475–495 (1982).

14. H. R. Gordon and A. Y. Morel, *Remote Assessment of Ocean Color for Interpretation of Satellite Visible Imagery: A Review* (Springer-Verlag, New York, 1983), p. 114.

15. G. N. Plass and G. W. Kattawar, "Monte Carlo calculations of radiative transfer in the earth's atmosphere–ocean system: 1. Flux in the atmosphere and ocean," J. Phys. Oceanogr. **2,** 139–145 (1972).

16. H. R. Gordon and O. B. Brown, "Irradiance reflectivity of a flat ocean as a function of its optical properties," Appl. Opt. **12,** 1549–1551 (1973).

17. J. T. O. Kirk, "Monte Carlo procedure for simulating the penetration of light into natural waters," CSIRO Div. Plant Ind. Technol. Paper 36 (Commonwealth Scientific and Industrial Research Organization, Canberra, Australia, 1981).

18. R. C. Smith and K. S. Baker, "Optical properties of the clearest natural waters (200–800 nm)," Appl. Opt. **20,** 177–184 (1981).

19. A. C. Tam and C. K. N. Patel, "Optical absorption of light and heavy water by laser optoacoustic spectroscopy," Appl. Opt. **18,** 3348–3358 (1979).

20. T. G. Peacock, K. L. Carder, C. O. Davis, and R. G. Steward, "Effects of fluorescence and water Raman scattering on models of remote sensing reflectance," in *Ocean Optics X,* R. W. Spinrad, ed., Proc. Soc. Photo-Opt. Instrum. Eng. **1302,** 303–319 (1990).

21. A. Morel, "Optical properties of pure water and pure sea water," in *Optical Aspects of Oceanography,* N. G. Jerlov and E. S. Steemann Nielsen, eds. (Academic, London, 1974) p. 494.

22. G. Kullenberg, "Scattering of light by Sargasso Sea water," Deep-Sea Res. **15,** 423–432 (1968).

23. T. J. Petzold, "Volume scattering functions for selected ocean waters," Slo Ref. 72–78 (Scripps Institute of Oceanography, University of California, San Diego, La Jolla, Calif., 1972).

24. W. F. Murphy and H. J. Bernstein, "Raman spectra and an assignment of the vibrational stretching region of water," J. Phys. Chem. **76,** 1147–1152 (1972).

25. H. W. Schrötter and H. W. Klöckner, "Raman scattering cross sections in gases and liquids," in *Raman Scattering of Gases and Liquids,* A. Weber, ed., Vol. 11 of Topics in Current Physics (Springer-Verlag, Berlin, 1979), pp. 123–166.

26. M. Iqbal, *Solar Radiation* (Academic, New York, 1984).

27. A. W. Harrison and C. A. Coombes, "Angular distribution of clear sky short wavelength radiance," Solar Energy **40,** 57–63 (1988).

28. A. Morel, "In-water and remote measurements of ocean color," Boundary-Layer Meteorol. **18,** 177–201 (1980).

29. D. A. Siegel and T. D. Dickey, "On the parameterization of irradiance for open ocean photoprocesses," J. Geophys. Res. **92,** 14,648–14,662 (1987).

30. R. H. Stavn, F. R. Schiebe, and C. L. Gallegos, "Optical controls on the radiant energy dynamics of the air/water interface: the average cosine and the absorption coefficient," in *Ocean Optics VII,* M. A. Blizard, ed., Proc. Soc. Photo-Opt. Instrum. Eng. **489,** 62–67 (1984).

31. R. H. Stavn, "The three-parameter model of the submarine light field: radiant energy absorption and trapping in nephelooid layers recalculated," J. Geophys. Res. **92,** 1934–1936 (1987).

Comparison of numerical models for computing underwater light fields

Curtis D. Mobley, Bernard Gentili, Howard R. Gordon, Zhonghai Jin, George W. Kattawar, André Morel, Phillip Reinersman, Knut Stamnes, and Robert H. Stavn

Seven models for computing underwater radiances and irradiances by numerical solution of the radiative transfer equation are compared. The models are applied to the solution of several problems drawn from optical oceanography. The problems include highly absorbing and highly scattering waters, scattering by molecules and by particulates, stratified water, atmospheric effects, surface-wave effects, bottom effects, and Raman scattering. The models provide consistent output, with errors (resulting from Monte Carlo statistical fluctuations) in computed irradiances that are seldom larger, and are usually smaller, than the experimental errors made in measuring irradiances when using current oceanographic instrumentation. Computed radiances display somewhat larger errors.

1. Introduction

Various numerical models are now in use for computing underwater irradiances and radiance distributions. These models were designed to address a wide range of oceanographic problems. The models are based on various simplifying assumptions, have differing levels of sophistication in their representation of physical processes, and use several different numerical solution techniques.

In spite of the increasingly important roles these numerical models are playing in optical oceanography, the models remain incompletely validated in the sense that their outputs have not been extensively compared with measured values of the quantities they predict. This desirable model–data comparison

C. D. Mobley is with the Jet Propulsion Laboratory, California Institute of Technology, Mail Stop 300-323, 4800 Oak Grove Drive, Pasadena, California 91109; B. Gentili and A. Morel are with the Laboratoire de Physique et Chimie Marines, Université Pierre et Marie Curie, F06230 Villefranche-sur-Mer, France; H. R. Gordon is with the Department of Physics, University of Miami, Coral Gables, Florida 33124; Z. Jin and K. Stamnes are with the Geophysical Institute, University of Alaska, Fairbanks, Alaska 99701; G. W. Kattawar is with the Department of Physics, Texas A & M University, College Station, Texas 77843; P. Reinersman is with the Department of Marine Science, University of South Florida, St. Petersburg, Florida 33701; and R. H. Stavn is with the Department of Biology, University of North Carolina, Greensboro, North Carolina 27412.

is not presently possible because the requisite comprehensive oceanic optical data sets are not available. Such data sets must contain simultaneous measurements of the inherent optical properties of the sea water (e.g., the absorption and scattering coefficients and the scattering phase function), environmental parameters (e.g., the sky radiance distribution and sea state), and radiometric quantities (e.g., the complete radiance distribution or various irradiances). The inherent optical properties and the environmental parameters are needed as input to the numerical models; the radiometric variables are the quantities predicted by the models. Current developments in oceanic optical instrumentation and measurement methodologies give cause for hope that data sets that are adequate for comprehensive model–data comparisons will become available within the next few years.

Meanwhile, our faith in these models' predictions rests on careful debugging of computer codes, internal checks such as conservation of energy or known relations between inherent and apparent optical properties, simulation of a few grossly simplified situations for which analytical solutions of the radiative transfer equation are available, and comparison (sometimes indirect) with incomplete data sets. An additional worthwhile check on the various models can be made by applying them to a common set of realistic problems. Such model–model comparisons help to identify errors in coding or weaknesses in the mathematical representation of physical phenomena, quantify numerical errors particular to the various solution algorithms, determine optimum numerical techniques for simulation of particular physical phe-

nomena, and determine which models might be appropriate for inclusion in a future library of underwater radiative transfer codes corresponding to those now available for atmospheric radiative transfer modeling (such as LOWTRAN[1]).

In March 1991 the Oceanic Optics Program of the Office of Naval Research sponsored a workshop to foster a close examination of the various models now in use and to begin the process of model–model comparison. This paper reports the results of that comparison. The models being evaluated are described in Section 2. During the workshop the participants defined a set of canonical (standard) problems for use in model comparisons. These problems are documented in Section 3. Section 4 presents selected results obtained when the models of Section 2 are applied to the problems of Section 3.

2. Numerical Models

All the numerical models compared here generate an approximate solution to the time-independent, monochromatic radiative transfer equation in one spatial dimension:

$$\mu \frac{\partial L(\tau; \mu, \phi)}{\partial \tau} = -L(\tau; \mu, \phi) + \omega_0(\tau) \iint\limits_{(\mu', \phi') \in \Xi} L(\tau; \mu', \phi')$$
$$\times \tilde{\beta}(\tau; \mu', \phi' \to \mu, \phi) d\mu' d\phi'$$
$$+ S(\tau; \mu, \phi). \qquad (1)$$

Here $L(\tau; \mu, \phi)$ is the unpolarized spectral radiance (at wavelength λ, omitted for brevity) at optical depth τ and in direction (μ, ϕ), ω_0 is the scattering-to-attenuation ratio, β is the scattering phase function, and S represents any internal source of radiance. The depth τ is measured positive downward from the mean sea surface, and the polar angle $\theta = \cos^{-1} \mu$ is measured from the nadir direction. (See Table 1 for a list of symbols and their units and definitions.) To solve Eq. (1) within a water body, it is necessary to specify (a) the inherent optical properties of the water body, ω_0 and β; (b) the distribution of internal sources S; (c) the radiance distribution that is externally incident upon the boundaries of the water body; and (d) the physical nature of the boundaries themselves.

The models differ primarily in the mathematical techniques used to solve Eq. (1) and in the treatment of boundary conditions at the sea surface. Two of the models described below (models II and DO) use analytical (invariant imbedding and discrete ordinates) techniques for solving Eq. (1), and five of the models (MC1–MC5) use probabilistic (Monte Carlo) techniques. Each of the models, as applied to the solution of the canonical problems defined in Section 3, solves Eq. (1) for a plane-parallel water body that is laterally homogeneous but may be inhomogeneous with depth. The upper boundary of the water body is the windblown, random air–water interface. The lower boundary is either an infinitely thick layer of water below the greatest depth of interest or an

Table 1. Significant Symbols, Units, and Definitions

Symbol	Units	Definition
λ	nm	Wavelength of light
ψ	deg	Scattering angle; $0 \leq \psi \leq 180°$
θ	deg	Polar angle of photon travel, measured from the nadir, $0 \leq \theta \leq 180°$
ϕ	deg	Azimuthal angle of photon travel, measured counterclockwise (looking downward) from the downwind direction, $0 \leq \phi < 360°$
μ	—	$\mu \equiv \cos \theta$; alternate way to specify the polar angle, $-1 \leq \mu \leq 1$
θ_v	deg	Polar viewing angle; $\theta_v = 180° - \theta$
ϕ_v	deg	Azimuthal viewing angle; $\phi_v = 180° + \phi$
Ω	sr	Solid angle; a differential element is $d\Omega = \sin \theta d\theta d\phi = d\mu d\phi$
Ξ_d	—	Set of all downward directions; $\int_{\Xi_d} d\Omega = 2\pi$ sr
Ξ_u	—	Set of all upward directions; $\int_{\Xi_u} d\Omega = 2\pi$ sr
z	m	Geometric depth, measured positive downward
τ	—	Optical depth, measured positive downward: $\tau \equiv \int_0^z c(z) dz$
σ	—	Standard deviation of the surface-wave slope
a_w	m^{-1}	Absorption coefficient for pure sea water
a_p	m^{-1}	Absorption coefficient for suspended particles
a	m^{-1}	Total absorption coefficient: $a \equiv a_w + a_p$
b_w	m^{-1}	Scattering coefficient for pure sea water
b_p	m^{-1}	Scattering coefficient for suspended particles
b	m^{-1}	Total scattering coefficient: $b \equiv b_w + b_p$
c	m^{-1}	Total attenuation coefficient: $c \equiv a + b$
β	m^{-1} sr^{-1}	Volume scattering function
$\tilde{\beta}$	sr^{-1}	Scattering phase function, $\tilde{\beta} \equiv \beta/b$
ω_0	—	Scattering-to-attenuation ratio, $\omega_0 \equiv b/c$
L	W m^{-2} sr^{-1} nm^{-1}	Radiance distribution, $L = L(z, \theta, \phi)$ or $L(\tau, \mu, \phi)$
L_u	W m^{-2} sr^{-1} nm^{-1}	Nadir radiance, $L_u \equiv L_u(\tau) \equiv L(\tau, \theta = 180, \phi = 0)$
L_∞	W m^{-2} sr^{-1} nm^{-1}	Asymptotic radiance distribution
k_∞	—	Asymptotic diffuse attenuation coefficient
S	W m^{-2} sr^{-1} nm^{-1}	Internal source of radiance
$E_\perp$	W m^{-2} nm^{-1}	Irradiance on a surface perpendicular to the sun's rays
E_d	W m^{-2} nm^{-1}	Downwelling plane irradiance: $E_d(\tau) \equiv \int_{\Xi_d} L(\tau, \mu, \phi) \lvert \mu \rvert d\Omega$
E_u	W m^{-2} nm^{-1}	Upwelling plane irradiance: $E_u(\tau) = \int_{\Xi_u} L(\tau, \mu, \phi) \lvert \mu \rvert d\Omega$
E_{ou}	W m^{-2} nm^{-1}	Upwelling scalar irradiance: $E_{ou}(\tau) \equiv \int_{\Xi_u} L(\tau, \mu, \phi) d\Omega$

opaque, reflecting bottom at a finite depth. The models all assume that externally applied radiance is incident downward upon the upper side of the air–water surface. The models are all monochromatic, and there are no internal sources of radiance (such as bioluminescence). However, some of the models can simulate inelastic-scattering processes by sequential solutions of Eq. (1). For example, the model is first

run at the wavelength of excitation, λ_{ex}, to compute the energy shifted by inelastic scattering from λ_{ex} to another wavelength λ, and then the model is run again at λ, with the radiance shifted from λ_{ex} appearing as a source term S at λ. A particular example of S used in this treatment of Raman scattering is given in Appendix A. The models all account for multiple scattering and can use realistic scattering phase functions that are highly peaked in forward directions, as is the case for sea water.

Several of the models have additional capabilities, such as the computation of polarized radiance in the Stokes vector format and the simulation of azimuthally anisotropic random air–water surfaces. These capabilities are not evaluated in this paper.

All but one of the models directionally discretizes Eq. (1) by partitioning the set of all directions, Ξ, into a grid of quadrilateral regions bounded by lines of constant μ and constant ϕ, plus two polar caps (collectively called quads). The fundamental quantity computed by these models is the quad-averaged radiance defined by

$$L(\tau; u, v) \equiv \frac{1}{\Omega_{uv}} \int\!\!\int_{(\mu,\phi)\in Q_{uv}} L(\tau; \mu, \phi)\,d\mu\,d\phi. \qquad (2)$$

$L(\tau; u, v)$ is physically interpreted as the average radiance over the set of directions (μ, ϕ) contained in the uvth quad, Q_{uv} (u labels μ bands and v labels ϕ bands), which subtends a solid angle of size Ω_{uv}. In the model comparison we chose to use 24 ϕ bands of uniform width $\Delta\phi = 15°$ and 20 μ bands of size $\Delta\mu = 0.1$. However, a polar cap with $\Delta\mu = 0.1$ has a half-angle of $\theta = 25.8°$, which is much larger than one would normally use in computing the nadir or zenith radiances. Therefore some models were run with a slightly different μ spacing and smaller polar caps. The remaining model (DO) computes the radiance $L(\tau; \mu, \phi)$ in particular (μ, ϕ) directions.

We now briefly describe the distinguishing features of the various models.

A. Model II [Invariant Imbedding, (Mobley)]

The integral operator of Eq. (2), which averages any quantity over the set of directions $(\mu, \phi) \in Q_{uv}$, can be applied to Eq. (1). The result is a quad-averaged radiative transfer equation in which $L(\tau; \mu, \phi)$ is replaced by $L(\tau; u, v)$, integration over all directions is replaced by summation over all quads, and the phase function $\beta(\tau; \mu', \phi' \to \mu, \phi)$ is replaced by a quad-averaged quantity $\beta(\tau; r, s \to u, v)$ that specifies how much of the radiance initially headed into quad Q_{rs} gets scattered into quad Q_{uv}. By standard techniques of Fourier analysis and invariant imbedding theory, the equations for the $L(\tau; u, v)$ are transformed into a set of Riccati differential equations governing the depth dependence of certain reflectance and transmittance functions within the water body. Depth integration of the Riccati equations (by a high-order Runge–Kutta algorithm) and incorporation of the boundary conditions at the sea surface and

bottom lead eventually to the desired $L(\tau; u, v)$ at all depths. These mathematical operations are outlined in Mobley[2] and are described in full by Mobley and Preisendorfer.[3] The inherent optical properties of the water body can vary arbitrarily with depth. Absorption and scattering are built up as sums of terms representing the contributions by pure water, particles of various types, and dissolved substances.

This model uses a Monte Carlo simulation of the windblown sea surface to evaluate certain quad-averaged, bidirectional reflectance and transmittance functions that describe how the sea surface reflects and transmits radiance that is incident upon the surface from above and below. In this simulation, the sea surface is resolved into a grid of triangular wave facets with vertex elevations that are randomly determined from any chosen wave slope–wind speed spectrum in a manner described by Mobley and Preisendorfer[3] and by Preisendorfer and Mobley.[4] The surface simulation allows for multiple reflections of rays by wave facets and for the possibility of shadowing of one facet by another. The probabilistic ray-tracing calculations for setting up the surface boundary conditions are independent of the analytical computations within the water body. Moreover, because the ray tracing involves only the surface-wave facets, for which it is assumed that there is no absorption, no rays are lost to absorption. It is therefore computationally feasible to trace a sufficient number of rays to reduce the Monte Carlo fluctuations in the computed bidirectional surface functions to a negligible level.

This model does not include an atmosphere per se. The sky radiance that is incident upon the sea surface is obtained either from an analytic model (e.g., a cardioidal distribution or the empirical model of Harrison and Coombes[5]) or from the output of a separately run atmospheric radiative transfer model. In the simulation of problem 4, below, LOWTRAN-7 was run to generate the sky radiance at the center of each of the μ–ϕ quads; that value was then taken as the average sky radiance over the quad.

The bottom boundary can be either an infinitely thick homogeneous layer of water below some depth τ_{max} or an opaque bottom at τ_{max}. In the infinite-depth case, the bidirectional radiance reflectance properties of the infinite layer below τ_{max} are obtained from an eigenmatrix analysis described by Preisendorfer.[6] The same analysis yields the asymptotic diffuse attenuation coefficient, k_∞, and the asymptotic radiance distribution, $L_\infty(\mu)$, that are appropriate for the homogeneous layer. In the opaque-bottom case, the reflectance properties of the bottom are explicitly specified, for example, as a Lambertian surface with a given irradiance reflectance.

The chief advantage of this model is computational efficiency. Solution of the Riccati differential equations for L is an analytic process, and thus there are no Monte Carlo fluctuations in the computed radiances (except for a negligible amount introduced by the simulation of the sea surface). In particular,

both upwelling and downwelling radiances are computed with the same accuracy. Moreover, computation time is a linear function of depth, so that accurate radiance distributions are easily obtained at great depths ($\tau > 10$). Computation time depends only mildly on quantities such as the scattering-to-attenuation ratio, surface boundary conditions, and water stratification. The associated computer code is available and is documented by Mobley.[7]

B. Model DO [Discrete Ordinates (Jin and Stamnes)]

This model solves Eq. (1) directly without applying the quad-averaging defined by Eq. (2). The radiance is expanded into a Fourier cosine series, $L(\tau, \mu, \phi) = \sum_{m=0}^{2N-1} L^m(\tau, \mu)\cos(\phi - \phi_0)$, and the phase function is expanded into a series of $2N$ Legendre polynomials,

$$\tilde{\beta}(\tau; \mu', \phi' \rightarrow \mu, \phi) \equiv \tilde{\beta}(\tau; \cos \psi)$$
$$= \sum_{l=0}^{2N-1} (2l + 1)g_l(\tau)P_l(\cos \psi),$$

where $g_l(\tau)$ is the expansion coefficient and ψ is the scattering angle. The advantage of these expansions is that the azimuthal dependence is isolated, in the sense that $2N$ independent equations for the Fourier coefficients $L^m(\tau, \mu)$ are obtained:

$$\mu \frac{dL^m(\tau, \mu)}{d\tau} = -L^m(\tau, \mu) + \omega_0(\tau) \int_{-1}^{1} L^m(\tau, \mu')$$
$$\times \beta^m(\tau; \mu', \mu)d\mu' + S^m(\tau, \mu),$$

where

$$\beta^m(\tau; \mu', \mu) = \frac{1}{2} \sum_{l=m}^{2N-1} (2l + 1)g_l(\tau)$$
$$\times \frac{(l - m)!}{(l + m)!} P_l^m(\mu)P_l^m(\mu').$$

Here $P_l^m(\mu)$ is the associated Legendre polynomial.

The atmosphere and the ocean are divided into a suitable number of layers to adequately resolve the optical properties of each of the two media. Each layer is taken to be homogeneous, but the optical properties are allowed to vary from layer to layer. For a homogeneous medium, only one layer is required. At the interface between the ocean and the atmosphere (assumed to be flat), Fresnel's formula is used to compute the appropriate reflection and transmission coefficients, and Snell's law is applied to account for the refraction taking place there.

The integral term in each of these azimuth-independent equations is then approximated by a Gaussian quadrature sum with $2N_1$ terms (streams) in the atmosphere and $2N_2$ terms in the ocean, so that there are $2N_1$ streams in the refractive region of ocean that communicate directly with the atmosphere and $2N_2 - 2N_1$ streams in the total reflection region of the ocean. In this way the integro-differential equation is transformed into a system of coupled ordinary differential equations that is solved by the discrete ordinate method, as described in more detail elsewhere,[8] subject to appropriate boundary conditions at the top of the atmosphere and the bottom of the ocean. The basic discrete-ordinate method used here is described and thoroughly documented in previous publications.[9–11] The modifications required to apply the method to a system consisting of two adjacent media with different indices of refraction are described by Jin and Stamnes.[8]

This method has the following unique features: (i) Because the solution is analytic, the computational speed is completely independent of individual layer and total optical thickness, which may be taken to be arbitrarily large. The computational speed is directly proportional to the number of horizontal layers used to resolve the optical properties in the atmosphere and ocean. (ii) Accurate irradiances are obtained with just a few streams, which makes the code very efficient. (iii) Because the solution is analytic, radiances and irradiances can be returned at arbitrary optical depths unrelated to the computational levels. (iv) The DO method is essentially a matrix eigenvalue–eigenvector solution, from which the asymptotic solution is automatically obtained. The smallest eigenvalue is k_∞, and the associated eigenvector is L_∞.

Desirable and possible extensions of the method include (i) the computation of inelastic-scattering effects to treat phenomena such as Raman scattering and (ii) the inclusion of a windblown surface to simulate the basic features of sea-surface roughness. These extensions would require some modifications of the existing computer code.

C. Model MCI [Monte Carlo (Gordon)]

This model simulates radiative transfer in both the ocean and the atmosphere, as coupled across a wind-roughened interface. The code is designed to simulate irradiances as a function of depth for computation of the irradiance reflectance, E_u/E_d, and diffuse attenuation functions such as $K_d = -d(\ln E_d)/dz$. The nadir-viewing radiance, L_u, is also computed as a function of depth for the computation of $Q = E_u/L_u$. The optical properties of the ocean are continuously stratified in the vertical. They can be specified as discrete values as a function of depth (with linear interpolation between the given depths) or determined from formulas as in problem 3, below. Separate scattering phase functions are used for the particles and for the water itself. Variants of this code have been used for a number of studies of radiative transfer in the ocean.[12–17]

The sea-surface roughness is modeled using the Cox and Munk[18] surface slope distribution for a given wind speed. The effect of the surface roughness is not simulated exactly because the possibility of shadowing of one facet by another is ignored. Multiple scattering, however, is included: e.g., if a downward-moving photon in the atmosphere encounters the sea surface and is still moving downward after reflection,

it will undergo a second interaction with the sea surface. One important aspect of this model is the proper use of photon weights to account for the fact that not all facets are oriented in such a manner as to be able to interact with an incident photon, i.e., facets with normals making an angle less than 90° to the direction of the incident photon. The sequence of events during an interaction with the surface follows. From Cox and Munk, the probability that the x and y components of the surface slope, z_x and z_y, respectively, are within $z_x \pm \frac{1}{2}dz_x$ and $z_y \pm \frac{1}{2}dz_y$ is

$$p(z_x, z_y)dz_x dz_y = \frac{1}{\pi\sigma^2} \exp\left(- \frac{z_x^2 + z_y^2}{\sigma^2}\right)dz_x dz_y,$$

or

$$p(\theta_n, \phi_n)d\theta_n d\phi_n = \frac{1}{\pi\sigma^2} \exp\left(- \frac{\tan^2 \phi_n}{\sigma^2}\right)$$
$$\times \tan \phi_n \sec^2 \phi_n d\theta_n d\phi_n.$$

where

$$\sigma^2 = 0.003 + 0.00512U.$$

Here U is the wind speed in meters per second, ϕ_n is the angle between the normal to the facet and the normal to the level surface, and θ_n is the azimuth of the normal. Given random numbers ρ_{θ_n} and ρ_{ϕ_n} on the unit interval $(0, 1)$, the model finds θ_n and ϕ_n from

$$\theta_n = 2\pi\rho_{\theta_n},$$

$$\rho_{\phi_n} = \frac{1}{2\pi^2\sigma^2} \int_0^{\phi_n} \exp\left(- \frac{\tan^2 \phi_n'}{\sigma^2}\right)\tan \phi_n' \sec^2 \phi_n' d\phi_n'.$$

The photon interacting with the surface is given the weight

$$W = \frac{\cos \omega \sec \phi_n}{\iint_{\cos\omega > 0} p(z_x, z_y)\cos \omega \sec \phi_n dz_x dz_y},$$

where ω is the angle of incidence upon the chosen facet. The weight, W, accounts for sampling from $p(z_x, z_y)$ even though all facets are not visible to the photon.

The atmospheric part of the model consists of fifty 1-km layers with both molecular and aerosol scattering. The vertical distribution of the optical properties is taken from Elterman.[19] The aerosol phase function at the given wavelength is determined from Mie theory[20] with Deirmendjian's Haze C size distribution[21]

$$\frac{dn(r)}{dr} \propto \frac{1}{r^{v+1}},$$

where r is the particle radius and $dn(r)$ is the number of particles per unit volume with radius between r

and $r + dr$; $v = 3$ is used in the computations. The aerosol total-scattering coefficient at each altitude is proportional to λ^{-P}, where $P = v - 2$; however, $P \approx 0.75$ fits Elterman's data better. When a photon interacts with the atmosphere, the scattering angle is chosen from either the molecular or aerosol phase functions based on the ratio of their scattering coefficients for the layer in which the interaction takes place.

When inelastic processes are to be included, the above code is operated at the excitation wavelength, λ_{ex}, to determine the excitation radiance distribution. This is used as input to a second Monte Carlo code that computes the light field at the wavelength of interest.[17] As with the elastically scattered radiation, the goal is to determine the irradiances of the inelastically scattered radiation. This is a considerable simplification because the solution can be effected by working with the azimuthally averaged radiance at λ; i.e., only the azimuthally averaged radiative transfer equation need be solved. The details of this formulation are given in Appendix A.

D. Model MC2 (Monte Carlo 2, Kattawar)

This model also simulates a coupled ocean–atmosphere system. The Monte Carlo code relies heavily on several variance-reducing schemes to increase computational efficiency. We give only a brief description of one of the most useful ones. The use of statistical weights allows us to treat each photon history as a packet of photons rather than as a single photon. Photons are never allowed to escape from the ocean–atmosphere system. The method of forced collisions is used, whereby we sample from a biased distribution that ensures a collision along the path, and the weight is then adjusted appropriately to unbias the result. The way this is done is as follows. Suppose one wants to compute the expectation value $\langle f \rangle$ of some function f of a random variable x, using a probability density function $p(x)$. By definition,

$$\langle f \rangle = \int f(x)p(x)dx.$$

However, if we want to sample from the density function, $\tilde{p}(x)$, then

$$\langle f \rangle = \int f(x)\frac{p(x)}{\tilde{p}(x)} \tilde{p}(x)dx = \int f(x)w(x)\tilde{p}(x)dx,$$

where $w(x) \equiv p(x)/\tilde{p}(x)$ is called the statistical weight. The variance σ^2 of $f(x)w(x)$ when sampling from the biased distribution is given by

$$\sigma^2[f(x)w(x)] = \int [f(x)w(x) - \langle f \rangle]^2\tilde{p}(x)dx.$$

Although this method appears straightforward, it does have pitfalls. If the weight can have values that exceed unity, then one can have a variance that far exceeds the variance in the unbiased sampling.

Therefore extreme caution must be used when applying this method. It should be noted that this is a very powerful method for studying perturbation effects, because several processes can be simultaneously emulated with the same set of photon histories.

Now consider the technique of forced collisions, in which photons are never allowed to escape the medium. Let τ_b denote the optical path length to a boundary. To ensure that the photon never escapes, we sample the path length according to the probability density function

$$\bar{p}(\tau)d\tau = \frac{\exp(-\tau)d\tau}{1 - \exp(-\tau_b)}, \qquad 0 \leq \tau \leq \tau_b.$$

The weight now has to be multiplied by $[1 - \exp(-\tau_b)]$ to remove the bias. It should be noticed that this factor is always less than unity and should produce a smaller variance than that produced when using unforced sampling. Histories are terminated only when the statistical weight falls below some specified value.

When an interaction occurs, the packet weight is multiplied by the single-scattering albedo, ω_0, which gives the fraction of photons that can continue to scatter. The level air–water interface is modeled by using the appropriate Fresnel reflection and transmission coefficients. A random number is chosen at this stage to determine whether the photon is transmitted or reflected.

Radiances are obtained over detectors that have finite solid angles. However, statistical estimation can be used to give true continuum radiance values where no directional averaging is done. This model can simulate inelastic scattering; the details are given in Kattawar and Xu.[22] The Monte Carlo method has also been extended to include the full Stokes vector treatment of polarization;[23–26] these papers show that substantial errors can occur if polarization is neglected.

E. Model MC3 [Monte Carlo 3 (Morel and Gentili)]

This Monte Carlo model is similar to those described by Plass and Kattawar[27,28] and by Gordon and Brown.[29] It is designed to simulate the radiance distribution at any level in the atmosphere and in the ocean. Between these two media, a wind-roughened interface is modeled with the isotropic Gaussian distribution of sea-surface slopes, as discussed under model MC1. The probability of occurrence of the various slopes is modified when considering nonvertically incident photons. This photon–facet interaction is modeled as in Plass et al.;[30] it does not account for the possible occultation of a facet by an adjacent one. Transmitted and reflected photon packets resulting from interaction with the air–water surface are weighted according to Fresnel's law (including the possibility of total internal reflection). According to the problem under investigation, photon packets are introduced at the top of the atmosphere, or just above (or below) the ocean surface. For specific problems

involving deep levels, packets can be reintroduced at intermediate depths inside the water body, according to a directional distribution that reproduces the downward radiance field as resulting from a previous Monte Carlo run. The bottom boundary is either an infinitely thick absorbing layer, in which photons are lost from the system, or a Lambertian reflecting bottom of a given albedo, from which weighted photon packets are reflected.

After each collision, the weight of each photon packet is multiplied by the local value of ω_0 that is pertinent to the altitude or the depth, to account for its partial absorption. A packet history is terminated when its weight falls below a predetermined value, typically 1×10^{-6}. For each collision a random number on the unit interval is compared with the local value of the ratio of the molecular scattering coefficient to the total scattering coefficient to determine if the scattering event will be of molecular type (air or water molecules) or is due to an aerosol or hydrosol particle. The appropriate phase function is then used to determine the scattering angle; the orientation of the scattering plane is chosen at random on the interval $(0, 2\pi)$. The number of photons initiated depends on the single-scattering albedo value, so as to control the stochastic noise in the computed radiometric quantities (details can be found in Morel and Gentili[31,32]). The model is operated for its oceanic segment with the optical properties as specified in Section 3. For the atmospheric segment, fifty 1-km-thick layers are considered, with specified values for Rayleigh and aerosol scattering and for ozone absorption as in Elterman.[19] The aerosol phase function (as computed by Mie scattering theory) for the maritime aerosol model defined by the Radiation Commission of the International Association of Meteorology and Atmospheric Physics is used; see the models of Tanré et al.[33] and Baker and Frouin.[34]

F. Model MC4 [Monte Carlo 4 (Reinersman)]

This model is intended primarily for simulation of the radiance distribution above and just below the surface, and for simulation of irradiances with the first five mean free paths of the surface. The model is based on techniques described by Kirk.[35] The model atmosphere is composed of 50 layers, each characterized by separate Rayleigh and particulate scattering coefficients and an albedo of single scattering, as given by Elterman.[19] Weighted photon beams are projected into the atmosphere from the atmosphere–space boundary, and a colllision is forced somewhere in the atmosphere along this original trajectory. The attenuated beam, which is the weight of the original beam less the portion lost to scattering and absorption, strikes the sea surface at the angle of the original trajectory. Beam losses that are due to absorption and scattering take place at the point of collision. There the absorbed portion is lost and the scattered portion exits the collision point in another single, weighted beam. A random number is compared with the ratio of the Rayleigh scattering cross

section to the total scattering cross section to determine the type of volume scattering function governing the scattering event. In the case of an aerosol scattering, a two-term Henyey–Greenstein phase function is used to determine the scattering angle.[36] Otherwise the angle is determined by a Rayleigh phase function.[37] Once the trajectory of the scattered portion of the beam is calculated, the distance from the point of collision to the next encountered interface (air–water or air–space) is determined. A new collision is forced somewhere along this trajectory, and the process is repeated until the weight of the scattered portion of the beam falls below a preset minimum fraction of the original beam weight. This minimum traceable weight is set to 1×10^{-6} of the original beam weight for the simulations presented below.

Some of the scattered trajectories encounter the atmosphere–space boundary and are forgotten; the others impinge on the sea surface. For the latter, the angle of incidence depends on the nadir angle of the ray and the slope of the sea surface. The directions of the reflected and refracted rays are determined geometrically, and the weights of the rays are calculated from the Fresnel formula. Although wave shadowing is neglected, multiple surface interactions may occur. A reflected ray that is still projected downward, or a transmitted ray that is still projected upward, must encounter the sea surface again immediately, without an intervening trajectory. Ray trajectories resulting from reflection are followed in the original manner. Transmitted portions of the beams are followed similarly until encountering the bottom or the sea surface, or until they are diminished to less than the minimum traceable weight. Those beams striking the bottom are lost; those beams that are incident upon the sea surface from below are again subjected to the reflection and transmission calculations.

G. Model MC5 [Monte Carlo 5 (Stavn)]

The Naval Research Laboratory optical model (referred to as the NORDA or NOARL optical model in earlier publications) uses standard Monte Carlo techniques.[13,28,35] At each scattering event, a random number is used to determine if the scattering is due to molecular water, quartzlike particulates, algae, or organic detritus; the volume scattering functions of these components are treated separately, rather than using an average volume scattering function. The model includes the effects of Raman scattering. If a photon collision results in inelastic scattering (as determined by comparing a random number to the appropriate optical properties of the medium), the wavelength is shifted by an amount corresponding to the mean wave-number shift of 3357 cm^{-1}, corresponding to Raman scatter by water molecules. The finite bandwidth of the Raman-shifted light is taken into account by averaging over 10-nm bandwidths (roughly corresponding to current oceanographic instruments); details of this averaging are described in

Stavn and Weidemann.[38,39] For the simulation of problem 7, below, it was assumed that the Raman scattering occurs in a very narrow waveband. The photons are tallied into zonal bands, as is convenient for computation of irradiances and the nadir-viewing radiance.

There is no atmosphere per se implemented in the model. Atmospheric transmittances of solar irradiance needed for simulations are obtained from the nonlayered atmospheric model of Brine and Iqbal.[40] The model determines the skylight radiance pattern from the empirical model of Harrison and Coombes.[5] The present version of the code handles only homogeneous waters.

3. Canonical Problems

We now define several canonical, or standard, problems for solution by underwater radiative transfer models. Models claiming to provide realistic simulations of the oceanic optical environment should be able to solve these problems and provide output that is at least as accurate as the data obtainable by presently available instrumentation. In brief, these problems are

Problem 1: An unrealistically simple problem.
Problem 2: A base problem using realistic inherent optical properties for the sea water.
Problem 3: The base problem but with stratified water.
Problem 4: The base problem but with atmospheric effects.
Problem 5: The base problem but with a wind-blown sea surface.
Problem 6: The base problem but with a finite-depth bottom.
Problem 7: A problem involving Raman scattering.

In each of these problems, the water body is taken to be horizontally homogeneous. The real index of refraction of the water is $n = 1.340$. The depth below the surface can be specified by either the nondimensional optical depth τ or by the geometric depth z in meters. The base problem 2 assumes that (a) the air–water surface is flat; (b) the water is homogeneous and infinitely deep; (c) there is no atmosphere, i.e., the sky is black; (d) the sun is a point light source located at a zenith angle of $\theta_{sun} = 60°$, (e) the sun provides a spectral irradiance just above the sea surface of magnitude $E_\perp = 1$ W m^{-2} nm^{-1} on a surface perpendicular to the sun's rays (which gives $E_d = 0.5$ W m^{-2} nm^{-1} for $\theta_{sun} = 60°$); (f) there is no inelastic scattering or other source of light within the water body; (g) the angular scattering properties of the water are characteristic of natural hydrosols; and (h) the water is either highly scattering ($\omega_0 = 0.9$) or highly absorbing ($\omega_0 = 0.2$). The other problems are defined by exceptions to these assumptions. The specific problem definitions are as follows.

Problem 1. A Rayleigh phase function

$$\tilde{\beta}_w(\mu', \phi' \to \mu, \phi) \equiv \tilde{\beta}_w(\psi) = \frac{3}{16\pi}(1 + \cos^2 \psi) \quad (3)$$

is used to describe the angular scattering properties of the water. The scattering angle, ψ, is related to the incident (μ', ϕ') and scattered (μ, ϕ) directions by

$$\psi = \cos^{-1}[\mu\mu' + (1 - \mu^2)^{1/2}(1 - \mu'^2)^{1/2}\cos(\phi - \phi')].$$

This phase function, which is plotted in Fig. 1(b), is similar to that of pure sea water. The Rayleigh phase function is a well-behaved function of the scattering angle, ψ, and presents no numerical difficulties in its treatment; we therefore consider this an easy problem for numerical modeling. Note that $\tilde{\beta}_w$ satisfies the normalization

$$2\pi \int_0^\pi \tilde{\beta}(\psi)\sin\,\psi d\psi = 1. \quad (4)$$

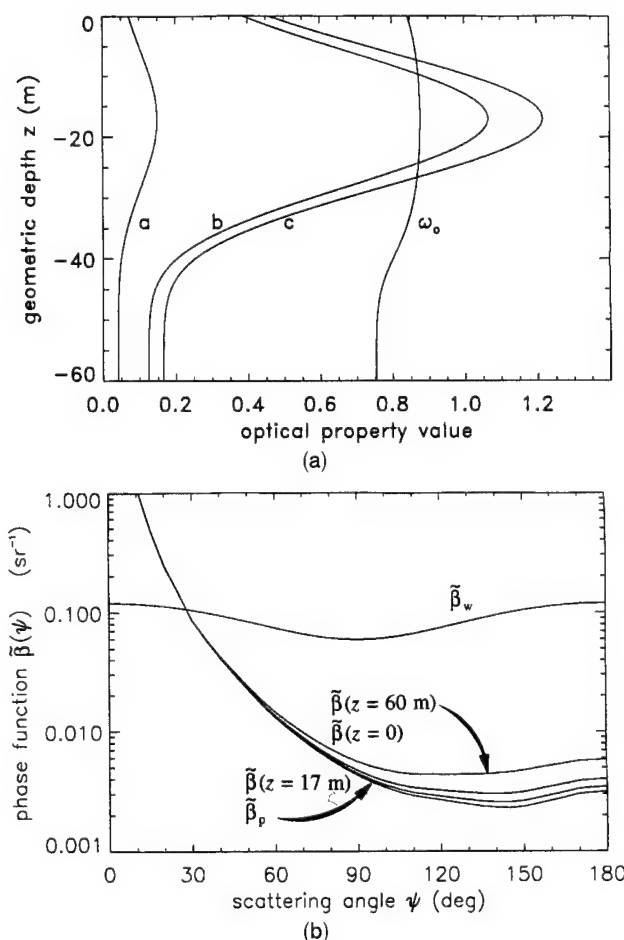Both highly scattering $(\omega_0 = 0.9)$ and highly absorb-

Fig. 1. (a) Inherent optical properties as a function of depth for problem 3. Coefficients $a, b,$ and c have units of inverse meters; ω_0 is dimensionless; (b) scattering-phase function for pure sea water, $\tilde{\beta}_w$; for particles, $\tilde{\beta}_p$; and for problem 3 at depths of $z = 0, 17,$ and 60 m.

ing $(\omega_0 = 0.2)$ cases are considered for the Rayleigh phase function.

Problem 2. This base problem uses a phase function that is typical of oceanic waters. The total volume scattering function (VSF) β is

$$\beta = \beta_w + \beta_p,$$

where subscripts w and p refer to pure sea water and to particles, respectively. The total phase function $\tilde{\beta}$ therefore can be expressed as

$$\tilde{\beta} = \frac{b_w}{b}\tilde{\beta}_w + \frac{b_p}{b}\tilde{\beta}_p. \quad (5)$$

This total $\tilde{\beta}$ must satisfy the normalization (4), which is the case if $\tilde{\beta}_w$ and $\tilde{\beta}_p$ are each normalized.

The particle phase function, $\tilde{\beta}_p$, is defined from three VSF's measured by Petzold[41] in San Diego harbor. The VSF for pure sea water[42] was first subtracted to find the three particle VSF's. Then the scattering coefficient of pure sea water[43] $(b_w = 0.00231$ m^{-1} at $\lambda = 530$ nm, the wavelength of Petzold's data) was subtracted from the respective scattering coefficients computed by Petzold $(b = 1.205, 1.536,$ and 1.824 m^{-1} for the three VSF's) to find the particle-scattering coefficient, b_p, for each VSF. The three particle phase functions were then computed with these b_p's, and the mean value of the three $\tilde{\beta}_p$'s was computed at each scattering angle. This mean $\tilde{\beta}_p(\psi)$ becomes infinite at $\psi = 0$, if it is assumed that $\beta_p(\psi) \sim \psi^{-m}$ as $\psi \to 0$, where $m = 1.346$ is the negative of the slope of $\log \tilde{\beta}_p(\psi)$ versus $\log \psi$ at the two smallest tabulated scattering angles $(\psi = 0.10°$ and $0.12589°)$. When this functional form of $\tilde{\beta}_p$ was used to integrate analytically $2\pi\tilde{\beta}_p(\psi)\sin\,\psi$ from $\psi = 0$ to $\psi = 0.10°$, and the trapezoidal rule was used to integrate from $\psi = 0.10°$ to $\psi = 180°$, the normalization integral (4) gave the value 1.006449. We thus divided the mean $\tilde{\beta}_p$ by 1.006449 to obtain the values shown in Table 2. The particle phase function $\tilde{\beta}_p(\psi)$ is then defined to be the tabulated values, with linear interpolation to be used between the tabulated values and with $\tilde{\beta}_p(\psi) \equiv \tilde{\beta}_p(0.12589°)$ $(0.12589°/\psi)^{1.346}$ for $\psi < 0.12589°$. The resulting $\tilde{\beta}_p(\psi)$ is defined for all ψ and exactly satisfies the normalization condition (4). This $\tilde{\beta}_p$ is plotted in Fig. 1(b).

Moreover, because $b_w = 0.00231$ m^{-1} is much less than $b_p (> 1.2$ m^{-1} for each of the Petzold VSF's), it is reasonable to neglect the contribution of the water, $\tilde{\beta}_w$, to the total phase function of Eq. (5). This omission creates an error of at most a few percent in $\tilde{\beta}$ even at backscattered directions $(\psi > 90°)$. We therefore define the total phase function for problem 2 to be just the particle phase function as defined above: $\tilde{\beta}(\psi) \equiv \tilde{\beta}_p(\psi)$. This $\tilde{\beta}$ is representative of phase functions measured in ocean waters with typical particle concentrations and, because of its highly peaked behavior at small ψ, can be expected to test the

Table 2. Phase Function Values Used in Defining the Particulate Phase Function $\tilde{\beta}_p(\psi)$

Scattering Angle (deg)	Phase Function[a] (sr^{-1})	Scattering Angle (deg)	Phase Function (sr^{-1})
0.10000	1.76661+3	50.0	2.27533−2
0.12589	1.29564+3	55.0	1.69904−2
0.15849	9.50172+2	60.0	1.31254−2
0.19953	6.99092+2	65.0	1.04625−2
0.25119	5.13687+2	70.0	8.48826−3
0.31623	3.76373+2	75.0	6.97601−3
0.39811	2.76318+2	80.0	5.84232−3
0.50119	2.18839+2	85.0	4.95306−3
0.63096	1.44369+2	90.0	4.29232−3
0.79433	1.02241+2	95.0	3.78161−3
1.0000	7.16082+1	100.0	3.40405−3
1.2589	4.95803+1	105.0	3.11591−3
1.5849	3.39511+1	110.0	2.91222−3
1.9953	2.28129+1	115.0	2.79696−3
2.5119	1.51622+1	120.0	2.68568−3
3.1623	1.00154+1	125.0	2.57142−3
3.9811	6.57957	130.0	2.47603−3
5.0119	4.29530	135.0	2.37667−3
6.3096	2.80690	140.0	2.32898−3
7.9433	1.81927	145.0	2.31308−3
10.0	1.15257	150.0	2.36475−3
15.0	4.89344−1	155.0	2.50584−3
20.0	2.44424−1	160.0	2.66183−3
25.0	1.47151−1	165.0	2.83472−3
30.0	8.60848−2	170.0	3.03046−3
35.0	5.93075−2	175.0	3.09206−3
40.0	4.20985−2	180.0	3.15366−3
45.0	3.06722−2		

[a]The notation $n \pm e = n \times 10^{\pm e}$.

numerical models' abilities to handle realistic phase functions. Both highly scattering and highly absorbing cases are considered for this phase function.

Problem 3. This problem is designed to test the models' abilities to compute light fields in highly stratified water. The water stratification is specified as follows. The particulate absorption and scattering coefficients are taken to be

$$a_p = 0.04C^{0.602}, \tag{6a}$$

$$b_p = 0.33C^{0.620}, \tag{6b}$$

respectively, where C is the chlorophyll (pigment) concentration. When C is in milligrams per inverse meters cubed, a_p and b_p are in inverse meters. The absorption representation (6a) is based on Prieur and Sathyendranath[44] at a wavelength of $\lambda = 500$ nm. The scattering representation (6b) is based on Gordon and Morel[45] with $\lambda = 500$ nm and assuming that $b_p(\lambda) \sim \lambda^{-1}$. The pigment profile with depth is based on Lewis *et al.*[46] and consists of a Gaussian plus a constant background:

$$C(z) = C_0 + \frac{h}{s\sqrt{2\pi}} \exp\left[-\frac{1}{2}\left(\frac{z - z_{\max}}{s}\right)^2\right]. \tag{7a}$$

Platt and Sathyendranath[47] show that Eq. (7a) with

the parameter values

$$C_0 = 0.2 \text{ mg m}^{-3}, \tag{7b}$$

$$s = 9 \text{ m}, \tag{7c}$$

$$z_{\max} = 17 \text{ m}, \tag{7d}$$

$$h = 144 \text{ mg m}^{-2}, \tag{7e}$$

fits data from the Celtic Sea in May very well. We therefore adopt Eq. (7) as a reasonable model for $C(z)$. When Eq. (7) is used in Eq. (6), the particulate absorption and scattering coefficients, and hence all inherent optical properties, become functions of depth. The absorption and scattering coefficients for pure sea water at $\lambda = 500$ nm are given by[43]

$$a_w = 0.0257 \text{ m}^{-1} \tag{8a}$$

$$b_w = 0.0029 \text{ m}^{-1}. \tag{8b}$$

When the chlorophyll concentration is low, scattering by pure sea water makes a significant contribution to the total scattering at large scattering angles (almost 1/2 when $C = C_0$ and $\psi = 180°$). Therefore, for this problem it is necessary to use Eq. (5) to determine the total phase function from the phase functions for pure sea water, $\tilde{\beta}_w$, and for particles, $\tilde{\beta}_p$, as were defined in problems 1 and 2. The phase function is now a function of depth, as is the scattering-to-attenuation ratio

$$\omega_0 \equiv \frac{b}{c} = \frac{b_w + b_p(z)}{a_w + a_p(z) + b_w + b_p(z)}.$$

Figure 1(a) shows a, b, c, and ω_0 as functions of depth for problem 3, and Fig. 1(b) shows the phase functions at selected depths.

Problem 4. This problem is the same as problem 2 with $\omega_0 = 0.9$, except that atmospheric effects are included. The sky is no longer black but rather has a radiance distribution that describes the atmosphere's scattering and absorption effects on sunlight. The incident solar irradiance, $E_\perp = 1 \text{ W m}^{-2} \text{ nm}^{-1}$, is now applied at the top of the atmosphere. The atmospheric optical effects are defined by Elterman's[19] aerosol and Rayleigh-scattering optical thicknesses at $\lambda = 500$ nm:

$$\tau_{\text{aerosol}} = 0.264,$$

$$\tau_{\text{Rayleigh}} = 0.145.$$

Because the numerical models incorporate atmospheric effects in various ways, a more detailed specification of the atmosphere is not made.

Problem 5. This problem is the same as problem 2 with $\omega_0 = 0.9$, except that the effects of a windblown sea surface are included. The surface waves are statistically specified as having a wave slope standard deviation of $\sigma = 0.2$ in the Cox–Munk[18] capillary-

wave spectrum

$$\sigma^2 = 0.003 + 0.00512U,$$

where U is the wind speed in meters per second. Thus $\sigma = 0.2$ corresponds to a wind speed of $U = 7.23$ m s^{-1}. The solar zenith angle is taken to be $\theta_{sun} = 80°$.

Problem 6. This problem is the same as problem 2, except that a finite-depth bottom is imposed. The bottom is taken to be an opaque, Lambertian reflecting surface at depth $\tau = 5$. This surface has an irradiance reflectance (E_u/E_d) of 0.5. Such a surface is a reasonable model of a light-colored, sandy bottom.

Problem 7. This problem is for use in comparing models that include the effects of Raman scattering by water molecules. The wavelength of excitation is taken to be $\lambda_{ex} = 417$ nm, and all light that is Raman scattered at 417 nm is assumed to shift to $\lambda = 486$ nm. The Rayleigh phase function, Eq. (3), is used for elastic scattering. The phase function for Raman scattering is[48]

$$\tilde{\beta}_{Ram}(\psi) = \frac{3}{16\pi} \frac{1 + 3\rho}{1 + 2\rho} \left(1 + \frac{1 - \rho}{1 + 3\rho} \cos^2 \psi \right), \quad (9)$$

where ρ is the depolarization ratio. For this problem, we use $\rho = 0.17$ and take the total Raman scattering coefficient b_{Ram} equal to the elastic-scattering coefficient of the water itself, i.e., $b_{Ram} = b_w$. The absorption and elastic-scattering coefficients of pure sea water at the wavelengths in question as taken from Smith and Baker[43] are

$$a_w(417) = 0.0156 \text{ m}^{-1},$$
$$b_w(417) = 0.0063 \text{ m}^{-1},$$
$$a_w(486) = 0.0188 \text{ m}^{-1},$$
$$b_w(486) = 0.0032 \text{ m}^{-1}.$$

Considering the way in which Smith and Baker inferred a_w from irradiance data, it is assumed that b_{Ram} is already included in the value of a_w. Thus the total beam attenuation coefficient at each wavelength is just $a_w + b_w$. A unit irradiance $E_\perp$ is incident at the sea surface upon a plane normal to the solar beam at the excitation wavelength $\lambda_{ex} = 417$ nm. There is no atmosphere and no solar irradiance is incident upon the sea surface at $\lambda = 486$. The resulting irradiances at 486 nm are those that would be solely because of inelastic scattering from 417 nm. The solar zenith angle is 60° and the air–water surface is flat.

Table 3 summarizes the various canonical problems.

4. Model Comparisons

Although the models generally compute the radiance L, the quantities most often used in oceanic optics are various irradiances. These irradiances are defined by weighted integrations of the radiance distribution over the upward and downward hemispheres of directions, as shown in Table 1, and are easily obtained from computed radiances. The nadir-viewing radiance, L_u, is the radiance seen by a sensor pointed straight down (in the nadir direction); L_u is important in remote-sensing studies. The ability of a numerical model to accurately compute the irradiances and nadir radiance is a measure of its utility for many oceanographic studies.

Models II and DO compute all quantities with equal accuracy. However, the Monte Carlo models MC1–MC5 compute upwelling quantities (e.g., E_u, E_{ou}, or L_u) with less accuracy than downwelling quantities (e.g., E_d or E_{od}). This is because most of the simulated photons, all of which are initially heading downward, continue to head downward and thereby contribute to E_d or E_{od}. However, only the relatively few photons that are scattered into upward directions can contribute to E_u, E_{ou}, or L_u; fewer photons means greater statistical fluctuations in the computed values.

Also, for a given initial number of photons, the

Table 3. Summary of the Canonical Problems

| Parameter | Problem | | | | | | |
	1 Easy Problem	2 Base Problem	3 Stratified Water	4 Atmospheric Effects	5 Windblown Surface	6 Bottom Effects	7 Raman Scattering
Albedo, ω_0	0.9, 0.2	0.9, 0.2	Depth dependent	0.9	0.9	0.2	0.29 at 417 nm 0.15 at 486 nm
Phase function	Rayleigh Eq. (3)	Particle Table 2	Depth dependent	Particle Table 2	Particle Table 2	Particle Table 2	Eqs. (3) and (9)
Air–water surface	Flat	Flat	Flat	Flat	Capillary waves	Flat	Flat
Diffuse sky radiance	0	0	0	Various models	0	0	0
Internal sources	0	0	0	0	0	0	Various models
Bottom boundary	Infinitely deep	Infinitely deep	Infinitely deep	Infinitely deep	Infinitely deep	Lambertian at $\tau = 5$	Infinitely deep

Monte Carlo models must settle for less accuracy at a given optical depth τ in highly absorbing waters (small ω_0) than in highly scattering waters (large ω_0). This is because photons absorbed before they reach depth τ are not available to be tallied in the computation of the radiance or irradiance, whereas scattered photons can eventually reach depth τ and be tallied. In practice, the accuracy of the Monte Carlo models is strongly dependent on the number of photon collisions; thus more photons must be processed when ω_0 is small to achieve satisfactory accuracy. The accuracy of models II and DO is independent of ω_0.

With the above comments in mind, we selected E_d, E_{ou}, and L_u for comparison just above the sea surface and at $\tau = 1, 5$, and 10. Problems 1 and 2 have both higly scattering ($\omega_0 = 0.9$) and highly absorbing ($\omega_0 = 0.2$) waters.

Although it is not possible to compare the computa-tional efficiencies of the various models because they were run on a variety of computers, with differing numbers of photons traced in the Monte Carlo codes, Table 4 shows some representative execution times. It should be noted that the long execution times shown for some of the Monte Carlo codes are the times required for accurate radiance simulations at large depths. If only irradiances or near-surface radiances are required for a particular study, these models can be run for much shorter times. For example, in the simulation of problem 3, output from model MC1 was compared for run times of 180 s and 7200 s. The E_d values throughout the euphotic zone (roughly the upper 21 m), as accumulated after 180 s, were within 1.5% of the values obtained after 7200 s. After 180 s, the E_{ou} and L_u values just below the surface (at $z = 0$) were within 1% of their final values. Deeper within the euphotic zone, E_{ou} and L_u differed

Table 4. Representative Execution Times, and Numbers of Simulated Photons for Models MC1–MC5

Problem	Execution Time (s)	Number of Photons Initiated	Number of Photon Collisons
	Model II (Computer: Sun SPARCstation 2, no code optimization)		
1, $\omega_0 = 0.9$	349 for $\tau = 10$; 730 for $\tau = 20$		
1, $\omega_0 = 0.2$	350 for $\tau = 10$; 733 for $\tau = 20$		
2, $\omega_0 = 0.9$	306 for $\tau = 10$; 496 for $\tau = 20$		
2, $\omega_0 = 0.2$	386 for $\tau = 10$; 711 for $\tau = 20$		
3	1180 for $z = 60$ m		
	Model DO (Computer: Decstation 5000/240, no code optimization)		
1, $\omega_0 = 0.9$	5 for irradiances only, 2 layers		
1, $\omega_0 = 0.2$	5 for irradiances only, 2 layers		
2, $\omega_0 = 0.9$	9 for irradiances only, 2 layers; 435 for radiances, 2 layers		
2, $\omega_0 = 0.2$	9 for irradiances only, 2 layers		
3	171 for irradiances only, 25 layers		
	Model MC1 (Computer: Decstation 5000)		
1, $\omega_0 = 0.9$	7200	1.25×10^6	4.98×10^7
1, $\omega_0 = 0.2$	7200	6.63×10^6	3.99×10^7
2, $\omega_0 = 0.9$	7200	9.66×10^6	7.18×10^7
2, $\omega_0 = 0.2$	7200	7.17×10^6	3.77×10^7
3	7200	7.49×10^6	8.74×10^7
	Model MC2 (Computer: Vax 9000)		
1, $\omega_0 = 0.9$	5830	1.0×10^6	9.47×10^7
1, $\omega_0 = 0.2$	530	1.0×10^6	7.54×10^7
2, $\omega_0 = 0.9$	4630	1.0×10^6	9.72×10^7
2, $\omega_0 = 0.2$	410	1.0×10^6	7.85×10^7
	Model MC3 (Computer: Hewlett Packard 9000/730)		
1, $\omega_0 = 0.9$	60000	10.9×10^6	6.72×10^8
1, $\omega_0 = 0.2$	74000	55.7×10^6	7.07×10^8
2, $\omega_0 = 0.9$	45000	8.7×10^6	7.30×10^8
2, $\omega_0 = 0.2$	84000	63.7×10^6	12.10×10^8
3	56000	8.9×10^6	9.02×10^8
	Model MC4 (Computer: Microvax III)		
1, $\omega_0 = 0.9$	15100	5.0×10^4	1.66×10^7
1, $\omega_0 = 0.2$	17700	1.0×10^6	1.44×10^7
2, $\omega_0 = 0.9$	9680	8.0×10^4	1.24×10^7
2, $\omega_0 = 0.2$	10000	1.2×10^6	1.02×10^7
3	24200	1.0×10^5	3.06×10^7
	Model MC5 (Computer: Cray Y-MP, no vectorization)		
1, $\omega_0 = 0.9$	1981 for $\tau = 20$	1.0×10^7	
1, $\omega_0 = 0.2$	416 for $\tau = 10$	1.0×10^7	
2, $\omega_0 = 0.9$	2300 for $\tau = 20$	1.0×10^7	
2, $\omega_0 = 0.2$	389 for $\tau = 10$	1.0×10^7	

by as much as 8% and 20%, respectively, for the two run times. At a depth of $z = 60$ m, the differences in the computed quantities for the two times were 3% for E_d, 19% for E_{ou}, and a factor of six for L_u. Model DO is much more efficient for irradiance and nadir (or zenith) radiance computations, than for full radiance computations, because only the azimuthally averaged equation (i.e., the $m = 0$ component of the radiance) is required to compute irradiances and nadir or zenith radiances. Full off-nadir or off-zenith radiance computations require the evaluation of additional azimuthal components. Strongly anisotropic scattering also requires a large number of streams.

We now briefly discuss the results of the models' simulations of problems 1–7.

Problem 1. Figure 2(a) shows the computed E_d, E_{ou}, and L_u for the Rayleigh phase function of prob-

(a)

(b)

Fig. 2. (a) E_d, E_{ou}, and L_u as computed by the various models for problem 1, $\omega_0 = 0.9$; (b) the same quantities as computed for the case of $\omega_0 = 0.2$. The dotted line represents the air–water surface. Results from models II and DO are plotted with solid lines; models MC1–MC5 are plotted with dashed lines. Depth $\tau = 0$ is in the water, just below the surface, and in air represents a point just above the surface.

lem 1 and $\omega_0 = 0.9$. In this and subsequent figures, we plot the results from the two analytic models, II and DO, with solid lines; the Monte Carlo results are plotted with dashed lines. This makes it easy to see that, in most instances, the Monte Carlo results are distributed to either side of the analytic results, which are usually indistinguishable in the figures.

We first note in Fig. 2(a) that all models predict nearly the same values for a given quantity, although there is a detectable spread in L_u values that is due to Monte Carlo fluctuations. This behavior is expected, based on the preceding discussion. However, we also note that all models predict nearly the same values for E_d and E_{ou}, which is counter to intuition based on oceanographic experience. This result is easily explained if we recall that the Rayleigh phase function is nearly isotropic (independent of the scattering angle) and that the medium is highly scattering. Because of the intense scattering, the incident collimated radiance distribution approaches its asymptotic form very quickly with depth. Preisendorfer[49] shows that for an isotropic phase function the asymptotic radiance distribution, L_∞, has an elliptical shape:

$$L_\infty(\theta) = \frac{L_0}{1 + k_\infty \cos \theta}. \qquad (10)$$

Here L_0 depends only on the inherent optical properties and k_∞ is the eccentricity of the ellipse; k_∞ is numerically equal to the nondimensional asymptotic diffuse attenuation coefficient. The analytic forms of L_∞ for a Rayleigh phase function and a Rayleigh phase matrix are also known.[50] For $\omega_0 = 0.9$ the Rayleigh L_∞ is very close to elliptical, and so we can use the simpler form of Eq. (10) for the following argument. The E_d and E_{ou} corresponding to L_∞ of Eq. (10) are

$$E_d = -\frac{2\pi L_0}{k_\infty^2} [k_\infty + \ln(1 - k_\infty)],$$

$$E_{ou} = \frac{2\pi L_0}{k_\infty} \ln(1 + k_\infty). \qquad (11)$$

Now the value of k_∞ for the problem at hand turns out to be $k_\infty \approx 0.52$ (see Table 7). This value is coincidentally very near to the value $k_\infty = 0.531$, which makes $E_d = E_{ou}$ in Eq. (11), thus explaining the numerical results seen in Fig. 2(a). This peculiar behavior of E_d and E_{ou} depends on both the phase function and the scattering-to-attenuation ratio. Such behavior is not seen in the output for the other problems, nor would it ever be encountered in a natural water body.

Note also that both E_d and E_{ou} are greater just below the water surface than just above it, which may also seem counterintuitive. However, this is just the phenomenon of optical energy trapping in highly scattering waters, as discussed by Stavn et al.[51] and by Plass et al.[52] In the present case of a solar angle of 60°, more than 93% of the incident solar irradiance is transmitted through the level surface into the water. Approximately one half of the highly diffuse
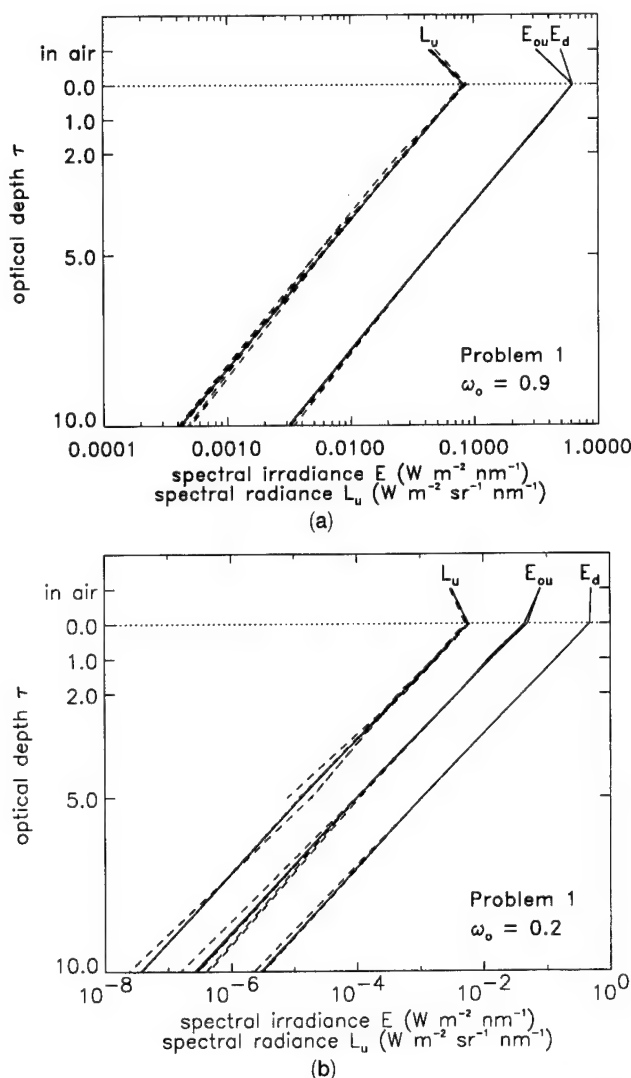
upwelling irradiance just below the surface is reflected back down by the surface. The total E_d just below the surface is the sum of the transmitted solar contribution and the reflected upwelling contribution; this sum is greater than $E_d(\text{air})$. Likewise, $E_{ou}(\text{air})$ consists of the (relatively weak) specularly reflected solar beam plus diffuse light transmitted upward through the water surface; this sum is less than E_{ou} just below the surface.

Figure 2(b) shows the output for the Rayleigh phase function and a highly absorbing medium with $\omega_0 = 0.2$. Now E_{ou} is an order of magnitude less than E_d. There is a spread of almost a factor of 3 in the Monte Carlo estimates of E_{ou} at $\tau = 10$, and three of the Monte Carlo models had too few photons left at $\tau = 10$ to provide an estimate of L_u at that depth. This behavior is expected for this highly absorbing case.

Table 5 displays the average (over all models) values of E_d, E_{ou}, and L_u at selected depths for this and the remaining problems. These data are provided for readers who wish to compare their own models with ours. Such comparisons should be especially worthwhile for simple parameterized models that attempt to compute irradiances without solving the complete radiative transfer equation. Table 5 also displays the ratio of the sample standard deviation s to the sample mean $\bar{x}$,

$$\frac{s}{\bar{x}} = \frac{\left[\dfrac{1}{N-1}\displaystyle\sum_{i=1}^{N}(x_i - \bar{x})^2\right]^{1/2}}{\dfrac{1}{N}\displaystyle\sum_{i=1}^{N}x_i},$$

where x_i is the result predicted by the ith model for the quantity of interest and N is the number of model predictions ($N = 7$ for most quantities). The ratio $s/\bar{x}$ is a quantitative measure of how close together the models' predictions are for a given quantity. Inspection of this ratio for problem 1 shows that the model predictions are usually closer together for the highly scattering case ($\omega_0 = 0.9$) than for the highly absorbing case ($\omega_0 = 0.2$), closer together at shallow depths, and closest together for E_d. The greatest spread in values is for L_u at large depths, because of the small number of photons available for its estimation by the Monte Carlo models.

Problem 2. Figure 3 shows the models' output for problem 2. Figure 3(a) is for the highly scattering case of $\omega_0 = 0.9$. Each of the seven models provides essentially the same values for E_d and for E_{ou} to 10 optical depths (and deeper); some Monte Carlo fluctuation is apparent in the L_u values. Figure 3(b) shows the same computations for the highly absorbing case of $\omega_0 = 0.2$. Once again, all models give nearly the same values for E_d and for E_{ou} to 10 optical depths. Now, however, considerable Monte Carlo fluctuation in the L_u values is seen at even shallow depths; only models II, DO, and MC3 were able to compute L_u below $\tau = 10$.

We emphasize that the large fluctuations seen in some of the estimates in Fig. 3(b) are simply the result of tracing an insufficient number of photons in the simulations, and not of any inadequacies in the models themselves. Tracing additional photons, at a proportional increase in computational expense, can reduce these fluctuations to any desired level. The particular values seen in Fig. 3 are each the result of one simulation. Running the Monte Carlo models with different seeds for their random number generators would generate a noticeably different set of curves for those instances where large fluctuations are seen in Fig. 3. It should be noted that there are certain sampling schemes that can improve the statistics at greater depths. However, this improvement is usually at the expense of larger errors in the radiometric quantities at smaller depths.

The euphotic zone is the region of a water body

Table 5. Average Values of E_d, E_{ou}, and L_u at Selected Depths for Problems 1–6[a]

Optical Depth	Average Value			Corresponding $s/\bar{x}$		
	E_d	E_{ou}	L_u	E_d	E_{ou}	L_u
Problem 1, $\omega_0 = 0.9$ ($N = 7$)						
1	3.66−1	3.72−1	4.85−2	0.002	0.005	0.015
5	4.33−2	4.35−2	5.59−3	0.003	0.007	0.052
10	3.16−3	3.20−3	4.37−4	0.015	0.038	0.091
Problem 1, $\omega_0 = 0.2$ ($N = 7$)						
1	1.41−1	1.34−2	1.72−3	0.001	0.003	0.044
5	1.07−3	1.00−4	1.37−5	0.005	0.039	0.288
10	2.93−6	3.00−7	3.39−8 ($N = 4$)	0.102	0.308	0.197
Problem 2, $\omega_0 = 0.9$ ($N = 7$)						
1	4.13−1	9.31−2	6.99−3	0.001	0.021	0.063
5	1.87−1	4.63−2	3.26−3	0.005	0.017	0.055
10	6.85−2	1.65−2	1.21−3	0.010	0.014	0.109
Problem 2, $\omega_0 = 0.2$ ($N = 7$)						
1	1.62−1	9.66−4	5.47−5	0.000	0.023	0.060
5	2.27−3	1.37−5	6.24−7 ($N = 6$)	0.002	0.063	0.355
10	1.30−5	7.28−8	4.02−9 ($N = 5$)	0.047	0.187	0.248
Problem 3 ($N = 6$)						
5 m	2.30−1	4.34−2	3.13−3	0.006	0.025	0.054
25 m	1.62−3	2.86−4	2.12−5	0.028	0.038	0.061
60 m	5.23−5	5.13−6	3.57−7	0.071	0.036	0.434
Problem 4 ($N = 6$)[b]						
1	3.23−1	7.13−2	5.63−3	0.076	0.091	0.111
5	1.49−1	3.57−2	2.77−3	0.072	0.076	0.141
10	5.56−2	1.31−2	9.60−4	0.070	0.073	0.107
Problem 5 ($N = 4$)						
1	1.14−1	3.55−2	2.09−3	0.012	0.020	0.031
5	4.33−2	1.22−2	7.63−4	0.009	0.028	0.036
10	1.48−2	3.65−3	2.49−4	0.007	0.020	0.025
Problem 6 ($N = 3$)						
1	1.62−1	9.81−4	6.84−5	0.000	0.010	0.020
5	2.28−3	2.28−3	3.60−4	0.003	0.002	0.010

[a]N is the number of models included in the averages. The ratio of the sample standard deviation to the sample mean, $s/\bar{x}$, is also displayed for each average value. The average values are relative to an incident solar irradiance of $E_\perp = 1.0$ W m^{-2} nm^{-1} upon the water surface, except for problem 4, for which $E_\perp$ is applied at the top of the atmosphere. The notation 3.66−1, for example, means 3.66×10^{-1}.

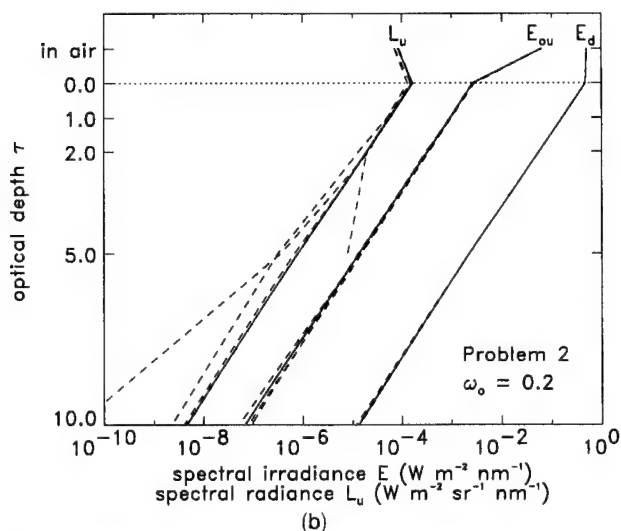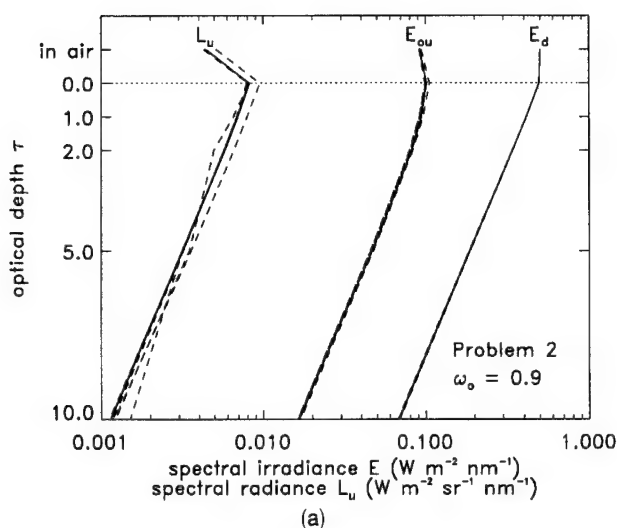[b]$s/\bar{x}$ values determined by systematic offset; see discussion in the text.

(a)

(b)

Fig. 3. Model predictions for problem 2, the base case: (a) $\omega_0 = 0.9$ and (b) $\omega_0 = 0.2$.

where there is sufficient light for photosynthesis to take place. In normal daylight conditions, it extends from the surface to a depth where the irradiance is roughly 1% of its surface value. We see in Fig. 3(b) that E_d and E_{ou} have decreased by 2 orders of magnitude at approximately 4 optical depths. Each of the models produces nearly identical irradiances to depths greater than $\tau = 4$, so that each of the models is perfectly adequate for the purposes of biological oceanography. Likewise, the models produce very nearly the same water-leaving radiances, L_u(air), as would be of interest in remote-sensing studies.

Problem 3. Figure 4 shows the models' output for problem 3, the stratified water case. The 1% irradiance level is now at approximately $z = 21$ m. Once again, the models provide nearly identical output to depths far below the euphotic zone.

Problem 4. Figure 5 shows E_d values near the water surface for the simulation of problem 4, the case with an atmosphere. The different ways in which the models simulate the atmosphere lead to an 18% spread in the values of E_d just above the water
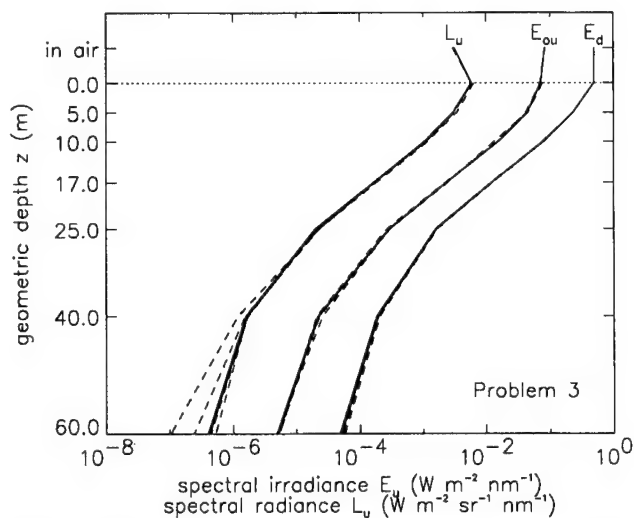
Fig. 4. Model predictions for problem 3, the stratified-water case.

surface. This difference in E_d(air) values is then carried throughout the underwater computations. The $s/\bar{x}$ ratio displayed in Table 5 is uniformly large for this problem because of the systematic offset of the different models' predictions. Note that apparent optical properties, such as reflectances and diffuse attenuation functions, are not affected by this offset, because the apparent properties are defined as ratios of radiometric quantities. For example, the $s/\bar{x}$ ratio for the K_d values computed from the plotted E_d values at depths $z = 0$ and 1 m is 0.009, which is much smaller than the $s/\bar{x} = 0.076$ value tabulated for E_d at $\tau = 1$.

Problem 5. Four of the models (II, MC1, MC3, and MC4) are capable of simulating a windblown air–water surface as defined in problem 5. Figure 6 shows output from these models for a solar zenith angle of $\theta_{sun} = 80°$. The models are nearly identical in their output, even in this case of nearly horizontal incidence, for which any differences in the models should be most noticeable. Note that E_{ou}(air) is
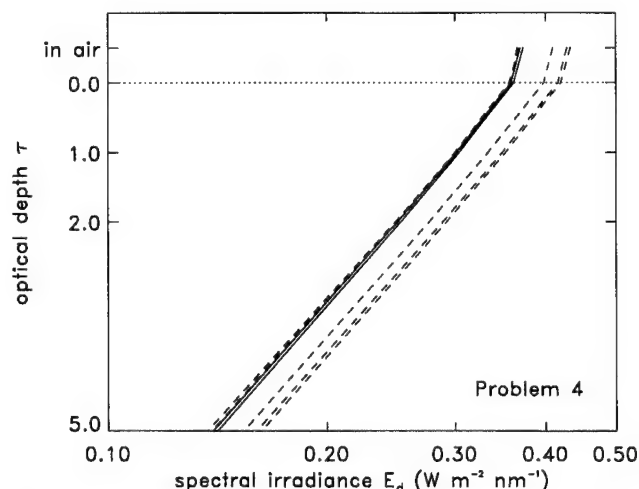

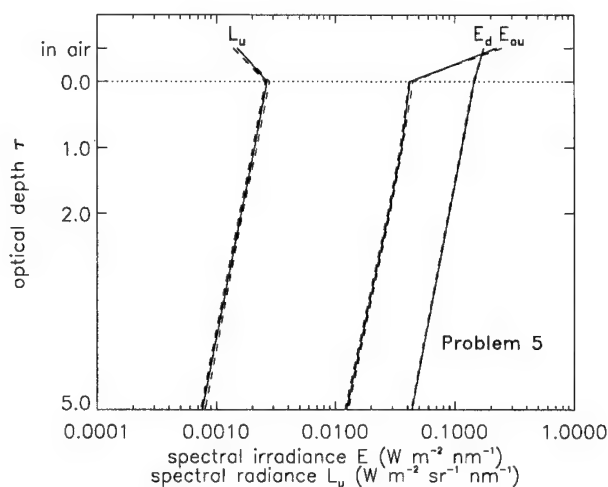Fig. 5. E_d near the surface for problem 4, the base case plus an atmosphere.

Fig. 6. Model predictions near the surface for problem 5, the capillary-wave case. The wind speed is $U = 7.23$ m s^{-1}, and the zenith angle of the sun is $\theta_{sun} = 80°$.

greater than E_d(air). This is because E_{ou}(air) contains a large contribution by the specularly reflected solar beam: simulations by Preisendorfer and Mobley[4] show that the reflectance of a capillary-wave surface is greater than 0.22 for a wind speed of 7.23 m s^{-1} and $\theta_{sun} = 80°$. The solar beam contribution to E_d is weighted by a cos θ_{sun} factor, which is small for $\theta_{sun} = 80°$.

Problem 6. Models II, DO, and MC3 can simulate a finite-depth bottom. Figure 7 shows the output from both models for the case of $\omega_0 = 0.2$; the models are clearly in excellent agreement. It is easy to show that $E_{ou} = E_d$ for a Lambertian surface of reflectance 0.5, and all three models show this expected result at depth $\tau = 5$.

Problem 7. Four of the models (MC1, MC2, MC3, and MC5) can simulate Raman scattering. Table 6 compares the inelastically scattered contributions to the downwelling and upwelling plane irradiances, E_d and E_u, respectively, for the simulation defined in

Table 6. Raman Scattering Contributions to E_d and E_u at $\subseteq$ = 486 nm From an Excitation Wavelength of $\subseteq_{ex}$ = 417 nm[a]

Depth (m)	Model			
	MC1	MC2	MC3	MC5
		E_d values		
0	0.01875	0.01874	0.01739	0.01873
50	0.02489	0.02488	0.02470	0.02490
100	0.01136	0.01136	0.01123	0.01138
		E_u values		
0	0.03532	0.03512	0.03478	0.03523
50	0.01034	0.01042	0.01027	0.01039
100	0.00287	0.00296	0.00292	0.00296

[a]Parameter values are given in the specification of problem 7. Values in the body of the table have units of W m^{-2} nm^{-1} for an incident irradiance of $E_\perp = 1.0$ W m^{-2} nm^{-1} at λ_{ex}.

problem 7. The models are clearly in excellent agreement, even though their respective formulations of inelastic scatter are somewhat different.

Computation of radiance distributions. Five of the models (II, DO, MC2, MC3, and MC4) compute the full radiance distribution, rather than just tallying photons as necessary to compute the irradiances and L_u. Figure 8 illustrates the consistency with which the various models compute the radiance distribution. The figure shows $L(\tau, \theta, \phi)$ in the plane of the sun at depths of $\tau = 0$, 5, and 20 for problem 2, $\omega_0 = 0.9$. Direction (θ_v, ϕ_v) gives the viewing direction, i.e., the direction an instrument points to detect photons traveling in the $(\theta = 180° - \theta_v, \phi = 180° + \phi_v)$ direction. Thus $\theta_v = 180°$ corresponds to looking straight up and seeing photons heading straight down; the nadir radiance, L_u, of Fig. 3(a) is the value plotted at $\theta_v = 0°$. The sun is in the $\phi_v = 0°$ half-plane.

The curves of Fig. 8 are explained as follows. We begin at $\tau = 0$ (in the water just below the surface)

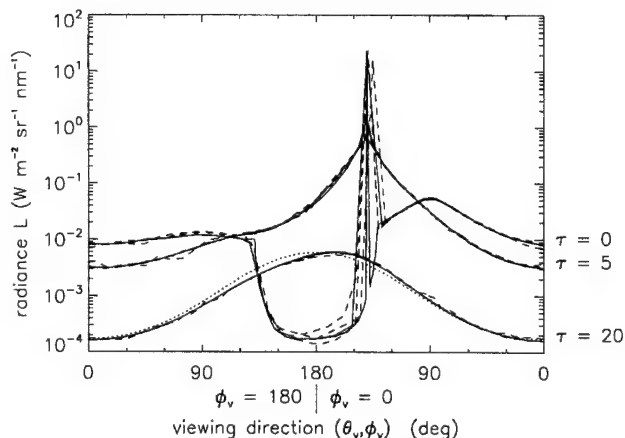Fig. 7. Model predictions for problem 6, the finite-depth case. The bottom reflectance is 0.5.

Fig. 8. Radiance distribution in the plane of the sun for problem 2, $\omega_0 = 0.9$. Angles (θ_v, ϕ_v) are viewing directions: $\theta_v = 180° - \theta$ and $\phi_v = 180° + \phi$, where (θ, ϕ) are the directions of photon travel. The solid curves are $L(\tau, \theta_v, \phi_v)$ at selected depths within the water for models II and DO; models MC2–MC4 are shown by the dashed curves. The dotted curve is the asymptotic distribution $L_\infty(\theta_v)$ normalized to the largest value of L at $\tau = 20$.

with our backs to the sun (looking in the $\phi_v = 180°$ direction). Looking straight down we see the nadir radiance at $(\theta_v, \phi_v) = (0°, 180°)$. Looking up toward the horizontal $(\theta_v = 90°)$, the radiance increases slightly because of total internal reflection of radiance that has been scattered into nearly horizontal directions. The radiance then decreases quickly as our viewing angle passes beyond the critical angle for total internal reflection. In the region around $\theta_v = 180°$ we are looking upward and seeing the upwelling radiance that is reflected downward by the level water surface. Note for example (using the digital output from Model II) that $L(\tau = 0, \theta_v = 180°)/L(\tau = 0, \theta_v = 0°) = 1.737 \times 10^{-4}/8.236 \times 10^{-3} = 0.021$, which is just the Fresnel reflectance of the surface for perpendicular incidence. Recall that in problem 2 the sky is black, so there is no sky radiance transmitted through the surface. In problem 4 (not shown), transmitted sky radiance fills in the large dip in the radiance near $\theta_v = 180°$. As our view passes the zenith we are now facing the sun. The large spike in the radiance near $(\theta_v, \phi_v) = (140°, 0°)$ is the refracted solar beam. The noticeable θ_v offset in the position of the plotted peak radiance occurs because different models choose their quad boundaries differently. The radiance values are plotted at the θ_v values of the quad centers, which range from 135° to 139.7° for the quad containing the refracted solar beam; plotted points are connected by straight lines. Looking beyond the sun, we see a large horizontal radiance, which decreases as we look downward.

Model DO shows a more pronounced spike in the radiance near the solar direction, and more pronounced changes near the critical angle than do the other models. This is because model DO computes radiances in specific directions, rather than quad-averaged radiances. The angular quadrature points in model DO are clustered near the critical angle and near the horizon, to get increased resolution in regions where the radiance varies rapidly with polar angle.

By depth $\tau = 5$, scattering has smeared out the solar beam and increased the downwelling radiance seen when looking upward near the zenith. The radiance distribution at $\tau = 20$ is very similar in shape to the asymptotic distribution, $L_\infty(\theta_v)$. The asymptotic distribution as computed by model II and normalized to the largest value of $L(\tau = 20)$ is shown as a dotted line in Fig. 8. Note that only a small amount of Monte Carlo fluctuation is seen even at $\tau = 20$, for this highly scattering case.

Radiance distributions computed by the various models are in equally close agreement for the other canonical problems (except for Monte Carlo fluctuations in the small ω_0 cases) and will not be discussed.

Computation of asymptotic radiances. The asymptotic radiance regime (also called the diffusion regime) is the region far enough from the boundaries of a homogeneous medium that the radiance is independent of the incident direction of the source and of boundary effects. Radiance in the asymptotic re-
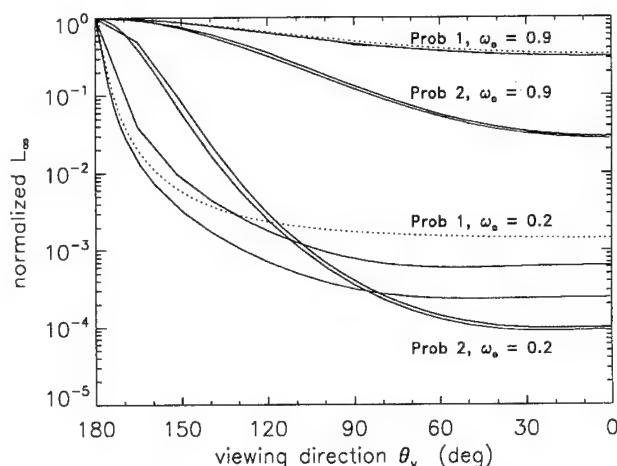

Fig. 9. Asymptotic radiance distributions $L_\infty(\theta_v)$ for problems 1 and 2, as computed by various models (solid curves). The dotted curves give the exact analytic solution[46] for the Rayleigh phase function of problem 1.

gime is independent of the azimuthal angle ϕ, and it decreases exponentially as $\exp(-k_\infty \tau)$. Here $k_\infty = K_\infty/c$, where K_∞ is the dimensional (in inverse meters) asymptotic diffuse attenuation coefficient and c is the beam attenuation coefficient. The shape $L_\infty(\theta)$ of the asymptotic radiance distribution is determined only by the inherent optical properties of the water; it is independent of depth.

Model II computes $L_\infty(\theta)$ and the associated value of the nondimensional asymptotic diffuse attenuation coefficient k_∞ by the solution of a matrix eigenvalue equation.[6] The smallest eigenvalue of the matrix is k_∞, and the associated eigenvector gives L_∞. Model DO obtains the asymptotic solution in a similar fashion. Models MC2 and MC3 obtain L_∞ and k_∞ by solution of the equivalent integral equation[49,53]

$$(1 - k_\infty \mu)L_\infty(\mu) = \omega_0 \int_0^{2\pi} \int_{-1}^{1} L_\infty(\mu')\tilde{\beta}(\psi)d\mu'd\phi'. \quad (12)$$

The exact analytical solution to Eq. (12) for the case of scattering according to a Rayleigh phase function, as well as for a Rayleigh phase matrix, was found by Kattawar and Plass.[50] Numerical solutions for phase functions that are highly peaked in the forward direction have been given in Kattawar and Plass[50] and in Prieur and Morel.[54]

Figure 9 shows the computed $L_\infty(\theta_v)$, normalized to one at $\theta_v = 180°$, for problems 1 and 2. Table 7

Table 7. Computed Values of k_∞

Problem	Model				
	II	DO	MC1[a]	MC2	MC3
1, $\omega_0 = 0.9$	0.5248	0.5232	0.52	0.5232	0.5235
1, $\omega_0 = 0.2$	1.0006	0.9994	—	0.9996	0.9952
2, $\omega_0 = 0.9$	0.1920	0.2068	0.189	0.1835	0.1879
2, $\omega_0 = 0.2$	0.8737	0.8794	—	0.8590	0.8619

[a]Values determined by visual inspection of plotted output.

Table 8. Comparison of Percent Accuracies for Computing and Measuring Radiometric Variables

Variable	2σ Spread of Model Values	Current Measurement Capability	Target Accuracy for SeaWiFS[a]
E_d	1	3–5	2
E_{ou}	5	3–5	—
L_u	12	3–5	3

[a]From Mueller and Austin.[55]

shows the corresponding k_∞ values. The numerical results are in excellent agreement for problem 2 and for the $\omega_0 = 0.9$ case of problem 1, which also agrees with its exact analytic solution. However, the numerical results differ considerably for the $\omega_0 = 0.2$ case of problem 1, and each is considerably off from the analytic solution. The reason for this inaccuracy in the computed L_∞ is as follows. For problem 1, $\omega_0 = 0.2$, the analytic k_∞ value is $k_\infty \approx 0.99937$. However, Eq. (12) becomes singular as $\mu \to 1$ when $k_\infty = 1$. For the nearly singular case at hand, both model II's eigenmatrix routine and the integral equation routines are having a difficult time determining accurate values for k_∞ and L_∞. This is most noticeable in the $k_\infty = 1.0006$ value determined by model II; the theoretical upper limit for k_∞ is exactly one. Even slight errors in k_∞ cause large differences in L_∞ when k_∞ is near one. Kattawar was able to obtain a satisfactory numerical solution of Eq. (12) for this case only after resorting to quadruple-precision arithmetic. The $k_\infty \approx 0.87$ value seen in problem 2, $\omega_0 = 0.2$, is far enough from one that no numerical difficulties arise. Note that the computation of k_∞ and L_∞ is a separate problem from the computation of the radiances and irradiances as discussed above. The inaccuracies in k_∞ and L_∞ just discussed in no way imply inaccuracies in the solution of Eq. (1).

5. Conclusions

Problems 1–3 of Section 3 cover the extreme range of oceanic inherent optical properties: ω_0 from 0.2 to 0.9, phase functions for pure Rayleigh and pure particulate scattering, and strong vertical stratification. In computations of E_d and E_{ou}, the numerical models of Section 2 usually gave results within a few percent of each other throughout the euphotic zone. The spread in L_u values was as large as 12% in highly scattering waters and much larger in highly absorbing waters at the bottom of the euphotic zone.

The statistical fluctuations of the Monte Carlo results from the true values of the predicted quantities are normally distributed. We therefore expect that more than 95% of the Monte Carlo simulations will be within 2 standard deviations (2σ) of the correct value. The data of Table 5 give us a feeling for the size of this 2σ spread of values. Table 8 shows the 2σ spread (expressed as a percentage of the mean) for E_d, E_{ou}, and L_u in near-surface waters (based on $\tau = 1$ for problems 1 and 2 and based on $z = 5$ m for problem 3). Column 2 of Table 8 shows typical errors in these

radiometric quantities when measured by commercial instruments now in wide use. The third column of the table shows the accuracy desired in measurements to be used for ground-truth validation of the SeaWiFS ocean color satellite[55] (to be launched in 1994). Obtaining such accuracies in E_d and L_u measurements requires very careful instrument calibration.

We see from Table 8 that the present numerical models easily compute E_d with greater accuracy than can be obtained with current instruments. Numerical estimates of E_{ou} have approximately the same accuracy as measured values. The computed values of L_u are less accurate than can be measured or than are needed for remote-sensing studies requiring absolute radiometric values of L_u. Thus the Monte Carlo models should trace more photon histories, if very accurate L_u values are required. The standard deviation of the Monte Carlo fluctuations is proportional to $n^{-1/2}$, where n is the number of photons traced. Therefore the 2σ spread seen in Table 8 can be cut in half by tracing four times as many photons, which is computationally practicable. Another possibility is to use the backward Monte Carlo method, as described in Gordon.[56]

Monte Carlo calculations made using statistical estimation techniques can also yield continuum radiances, rather than quad-averaged values. Thus if one is interested in results for a few detectors located at precise angles, this technique can give highly accurate radiance values with only a very few photons being traced.[57–59]

Values predicted by the Monte Carlo models generally fall on both sides of the values predicted by models II and DO, which do not have statistical fluctuations. Thus models II and DO have an advantage in the computation of upwelling quantities or in computations at great depths, which require tracing very large numbers of photons in the Monte Carlo codes.

The systematic differences in the atmospheric models used to simulate problem 4 lead to a 2σ spread of the order of 20% in the computed radiometric quantities. Thus to compute acceptably accurate absolute radiometric values, more careful attention must be paid to how the incident radiance upon the water surface is obtained. However, as noted before, systematic offsets in the absolute radiometric variables do not affect the values of apparent optical properties obtained from the radiometric variables. The present simple atmospheric models therefore all appear to be satisfactory for the computation of apparent optical properties.

Based on the problem solutions presented above, and on such comparisons between models and oceanographic measurements as have been made (not discussed here), we conclude that each of the numerical models discussed here incorporates correct mathematical representations of the relevant radiative processes (absorption and elastic and inelastic scattering) and of the effects of the air–water boundary.

Moreover, the models provide accurate numerical solutions of the associated equations. Each of these models is adequate for most of the needs of optical oceanography and limnology.

Appendix A: Inelastic Source Function for Model MC1

As noted in Section 2, model MC1 incorporates Raman scattering (and other inelastic processes, such as fluorescence) in an azimuthally averaged form suitable for the computation of inelastic-scattering effects on irradiances. The corresponding mathematical form of the source function, which is used in the ϕ-averaged version of Eq. (1), is developed as follows. This formulation is based on expanding both the Raman scattering function and the azimutmultally averaged excitation radiance in a series of Legendre polynomials.[60]

The source function for inelastic processes is given by

$$S_{in}(z, \theta, \lambda)$$

$$= \frac{1}{4\pi} \sum_{l=0}^{N} \int b_{in}^{(l)}(z, \lambda_{ex} \to \lambda) P_l(\cos\theta) E_l(z, \lambda_{ex}) d\lambda_{ex},$$

with

$$E_l(z, \lambda_{ex}) = 2\pi \int_0^\pi P_l(\cos\theta') L^{(0)}(z, \theta', \lambda_{ex})$$

$$\times \sin\theta' d\theta',$$

$$\beta_{in}(z, \psi, \lambda_{ex} \to \lambda) = \frac{1}{4\pi} \sum_{l=0}^{N} b_{in}^{(l)}(z, \lambda_{ex} \to \lambda) P_l(\cos\psi).$$

$$(A1)$$

In these equations, P_l is the Legendre polynomial of order l, $N = 0$ for isotropically emitted fluorescence, and $N = 2$ for Raman scattering. The total inelastic-scattering coefficient $b_{in}^{(0)}$ is

$$b_{in}^{(0)}(z, \lambda_{ex} \to \lambda) \equiv b_{in}(z, \lambda_{ex} \to \lambda)$$

$$= \int_{\Xi'} \beta_{in}(z; \theta', \phi' \to \theta, \phi; \lambda_{ex} \to \lambda) d\Omega'$$

$$= 2\pi \int_0^\pi \beta_{in}(z, \psi, \lambda_{ex} \to \lambda) \sin\psi d\psi.$$

E_l for $l = 0$ is just the scalar irradiance at λ_{ex}, whereas E_l for $l = 1$ is the net irradiance $E_d - E_u$ at λ_{ex}. The inelastic component of the irradiance at λ depends only on the irradiances at the excitation wavelength(s) and on the $b_{in}^{(l)}$ coefficients for the particular process.

For Raman scattering, $\beta_{in} \equiv \beta_{Ram}$, and the angular distribution of β_{Ram} is given by

$$\beta_{Ram}(z, \psi, \lambda_{ex} \to \lambda) = \tilde{\beta}_{Ram}(\psi) b_{Ram}(z, \lambda_{ex} \to \lambda), \quad (A2)$$

where $\tilde{\beta}_{Ram}(\psi)$ is given by Eq. (9). Substituting Eq. (9) into Eq. (A2) and rewriting in terms of the Le-

gendre polynomials and the quantity $\gamma \equiv (1 - \rho)/(1 + 3\rho)$ gives

$$\beta_{Ram} = \frac{3}{16\pi} \left(\frac{1 + 3\rho}{1 + 2\rho}\right) \left[1 + \frac{1}{3}\gamma + \frac{2}{3}\gamma P_2(\cos\psi)\right]$$

$$\times b_{Ram}(z, \lambda_{ex} \to \lambda). \quad (A3)$$

Comparing Eqs. (A1) and (A3) reveals that

$$b_{Ram}^{(0)}(z, \lambda_{ex} \to \lambda) = b_{Ram}(z, \lambda_{ex} \to \lambda),$$

$$b_{Ram}^{(2)} = \frac{1}{2}\left(\frac{1 - \rho}{1 + 2\rho}\right) b_{Ram}(z, \lambda_{ex} \to \lambda),$$

and that all of the other $b_{Ram}^{(l)}$ are zero. Finally, the ϕ-averaged source function for Raman scattering is given by

$$S_{Ram}(z, \theta, \lambda) = \frac{1}{4\pi} \int b_{Ram}(z, \lambda_{ex} \to \lambda) E_0(z, \lambda_{ex})$$

$$\times \left[1 + \frac{1}{2}\left(\frac{1 - \rho}{1 + 2\rho}\right) \frac{E_2(z, \lambda_{ex})}{E_0(z, \lambda_{ex})} P_2(\cos\theta)\right] d\lambda_{ex}.$$

In general, at the emission wavelength λ, the source function resulting from a narrow band of excitation wavelengths $\Delta\lambda_{ex}$ is

$$S_{in}(z, \theta, \lambda) = \frac{1}{4\pi} b_{in}(z, \lambda_{ex} \to \lambda) \Delta\lambda_{ex} E_0(z, \lambda_{ex})$$

$$\times \sum_{l=0}^{N} \frac{b_{in}^{(l)}(z, \lambda_{ex} \to \lambda) E_l(z, \lambda_{ex})}{b_{in}(z, \lambda_{ex} \to \lambda) E_0(z, \lambda_{ex})} P_l(\cos\theta).$$

$$(A4)$$

To simulate the irradiances at λ, the basic Monte Carlo code for elastic scattering only is run at λ_{ex} to determine $E_l(z, \lambda_{ex})$. Then Eq. (A4) is used to inject inelastically scattered photons into the medium with the proper distribution in z and θ. One way to do this is to choose z from the probability density $p(z)$ given by

$$p(z) = \frac{E_0(z, \lambda_{ex})}{\int_0^\infty E_0(z, \lambda_{ex}) dz}.$$

Thus, given a random number ρ_j from the sequence $\ldots \rho_j, \rho_{j+1}, \rho_{j+2}, \ldots$, z is found from

$$\rho_j = \int_0^z p(z') dz'.$$

Given z, we then choose θ from the conditional density $p(\theta|z)$ given by

$$p(\theta|z) = \frac{1}{4\pi} \sum_{l=0}^{N} \frac{b_{in}^{(l)}(z, \lambda_{ex} \to \lambda) E_l(z, \lambda_{ex})}{b_{in}(z, \lambda_{ex} \to \lambda) E_0(z, \lambda_{ex})} P_l(\cos\theta),$$

so that

$$\rho_{j+1} = \int_0^\theta p(\theta'|z)\mathrm{d}\theta'.$$

Finally, the rest of the source function must be incorporated into a photon weight

$$W = b_{\mathrm{in}}(z, \lambda_{\mathrm{ex}} \to \lambda)\Delta\lambda_{\mathrm{ex}} \int_0^\infty E_0(z, \lambda_{\mathrm{ex}})\mathrm{d}z,$$

so that $S_{\mathrm{in}}(z, \theta, \lambda) = Wp(z)p(\theta|z)$ as required. Once a photon is emitted at λ, it is followed in a manner similar to that which would be used in the absence of inelastic scattering, with the exception that inelastic scattering from λ to longer wavelengths is included by increasing the absorption coefficient $a(z, \lambda)$ by the appropriate inelastic-scattering coefficient $b_{\mathrm{in}}(z, \lambda \to \lambda')$ with $\lambda < \lambda'$ (recall, however, the discussion of this point in the definition of problem 7). In the code, $E_0(z, \lambda_{\mathrm{ex}})$ is normalized to unit irradiance at λ_{ex} entering the top of the atmosphere normal to the solar beam, so the computed irradiances at λ (as seen in Table 6) are for unit irradiance at λ_{ex} entering the top of the atmosphere. This simulation technique was in part developed in this manner so that it could be used with experimental measurements of E_l to predict the inelastically scattered irradiances for a given process, e.g., Raman scattering. Such measurements can be obtained using instrumentation developed by Voss.[61,62]

References

1. F. Kneizys, E. Shettle, L. Abreu, J. Chetwynd, G. Anderson, W. Gallery, J. Selby, and S. Clough, "Users guide to LOWTRAN-7," Rep. AFGL-TR-88-0177 (U.S. Air Force Geophysics Laboratory, Hanscom Air Force Base, Mass., 1988).
2. C. Mobley, "A numerical model for the computation of radiance distributions in natural waters with wind-roughened surfaces," Limnol. Oceanogr. **34**, 1473–1483 (1989).
3. C. Mobley and R. Preisendorfer, "A numerical model for the computation of radiance distributions in natural waters with wind-roughened surfaces," NOAA Tech. Memo. ERL PMEL-75 (NTIS PB88-192703) (Pacific Marine Environmental Laboratory, Seattle, Wash., 1988).
4. R. Preisendorfer and C. Mobley, "Albedos and glitter patterns of a wind-roughened sea surface," J. Phys. Oceanogr. **16**, 1293–1316 (1986).
5. A. Harrison and C. Coombes, "Angular distribution of clear sky short wavelength radiance," Sol. Energy **40**, 57–69 (1988).
6. R. Preisendorfer, "Eigenmatrix representations of radiance distributions in layered natural waters with wind-roughened surfaces," NOAA Tech. Memo. ERL PMEL-76 (NTIS PB88-188701) (Pacific Marine Environmental Laboratory, Seattle, Wash., 1988).
7. C. Mobley, "A numerical model for the computation of radiance distributions in natural waters with wind-roughened surfaces, part II: users' guide and code listing," NOAA Tech. Memo. ERL PMEL-81 (NTIS PB88-246871) (Pacific Marine Environmental Laboratory, Seattle, Wash., 1988).
8. Z. Jin and K. Stamnes, "Radiative transfer in nonuniformly refracting layered media such as the atmosphere–ocean system," Appl. Opt. (to be published).
9. K. Stamnes and R. A. Swanson, "A new look at the discrete ordinate method for radiative transfer calculations in anisotropically scattering atmospheres," J. Atmos. Sci. **38**, 387–399 1981.
10. K. Stamnes and H. Dale, "A new look at the discrete ordinate method for radiative transfer calculations in anisotropically scattering atmospheres. II: Intensity computations," J. Atmos. Sci. **38**, 2696–2706 (1981).
11. K. Stamnes, S. C. Tsay, W. Wiscombe, and K. Jayaweera, "Numerically stable algorithm for discrete-ordinate-method radiative transfer in multiple scattering and emitting layered media," Appl. Opt. **27**, 2502–2509 (1988).
12. H. Gordon, O. Brown, and M. Jacobs, "Computed relationships between the inherent and apparent optical properties of a flat homogeneous ocean," Appl. Opt. **14**, 417–427 (1975).
13. H. Gordon, "A bio-optical model describing the distribution of irradiance at the sea surface resulting from a point source embedded in the ocean," Appl. Opt. **26**, 4133–4148 (1987).
14. H. Gordon, "Can the Lambert–Beer law be applied to the diffuse attenuation coefficient of ocean water?" Limnol. Oceanogr. **34**, 1389–1409 (1989).
15. H. Gordon, "Dependence of the diffuse reflectance of natural waters on the sun angle," Limnol. Oceanogr. **34**, 1484–1489 (1989).
16. H. Gordon, "Diffuse reflectance of the ocean: influence of nonuniform phytoplankton pigment profile," Appl. Opt. **31**, 2116–2129 (1992).
17. Y. Ge, H. Gordon, and K. Voss, "Simulation of inelastic-scattering contributions to the irradiance field in the oceanic variation in Fraunhofer line depths," Appl. Opt. **32**, 4028–4036 (1993).

18. C. Cox and M. Munk, "Statistics of the sea surface derived from sun glitter," J. Mar. Res. **13**, 198–227 (1954).

19. L. Elterman, "UV, visible, and IR attenuation for altitudes to 50 km," Rep. AFCRL-68-0153 (U.S. Air Force Cambridge Research Laboratory, Bedford, Mass., 1968).

20. G. Mie, "Beiträge zur Optik trüber Medien, speziell Kolloidalen Metall-Lösungen," Ann. Phys. **25**, 377–445 (1908).

21. D. Deirmendjian, "Scattering and polarization properties of polydisperse suspensions with partial absorption," in *Electromagnetic Scattering,* M. Kerker, ed. (Pergamon, New York, 1963), pp. 171–189.

22. G. Kattawar and X. Xu, "Filling-in of Fraunhofer lines in the ocean by Raman scattering," Appl. Opt. **31**, 1055–1065 (1992).

23. G. Kattawar and C. Adams, "Stokes vector calculations of the submarine light field in an atmosphere–ocean with scattering according to a Rayleigh phase matrix: effect of interface refractive index on radiance and polarization," Limnol. Oceanogr. **34**, 1453–1472 (1989).

24. G. Kattawar and C. Adams, "Errors in radiance calculations induced by using scalar rather than Stokes vector theory in a realistic atmosphere–ocean system," in *Ocean Optics X,* R. W. Spinrad, ed., Proc. Soc. Photo-Opt. Instrum. Eng. **1302,** 2–12 (1990).

25. C. Adams and G. Kattawar, "Effect of volume scattering function on the errors induced when polarization is neglected in radiance calculations in an atmosphere–ocean system," Appl. Opt. **20,** 4610–4617 (1993).

26. G. Kattawar and C. Adams, "Errors induced when polarization is neglected in radiance calculations for an atmosphere–ocean system," in *Optics of the Air–Sea Interface: Theory and Measurement,* L. Estep, ed., Proc. Soc. Photo-Opt. Instrum. Eng. **1749,** 2–22 (1992).

27. G. Plass and G. Kattawar, "Radiative transfer in an atmosphere–ocean system," Appl. Opt. **8,** 455–466 (1969).

28. G. Plass and G. Kattawar, "Monte-Carlo calculations of radiative transfer in the earth's atmosphere ocean system: I. Flux in the atmosphere and ocean," J. Phys. Oceanogr. **2,** 139–145 (1972).

29. H. Gordon and O. Brown, "Irradiance reflectivity of a flat ocean as a function of its optical properties," Appl. Opt. **12,** 1549–1551 (1973).

30. G. Plass, G. Kattawar, and J. Guinn, Jr., "Radiative transfer in the earth's atmosphere and ocean: influence of ocean waves," Appl. Opt. **14,** 1924–1936 (1975).

31. A. Morel and B. Gentili, "Diffuse reflectance of oceanic waters: its dependence on sun angle as influenced by the molecular scattering contribution," Appl. Opt. **30,** 4427–4438 (1991).

32. A. Morel and B. Gentili, "Diffuse reflectance of oceanic waters. II. bidirectional aspects," Appl. Opt. (to be published).

33. D. Tanré, M. Herman, R. Deschamps, and A. deLeffe, "Atmospheric modeling for space measurements of ground reflectances including bi-directional properties," Appl. Opt. **18,** 3587–3594 (1979).

34. K. Baker and R. Frouin, "Relation between photosynthetically available radiation and total insolation at the ocean surface under clear skies," Limnol. Oceanogr. **32,** 1370–1377 (1987).

35. J. Kirk, "Monte Carlo procedure for simulating the penetration of light into natural waters," Div. Plant Industry Tech. Paper 36 (Commonwealth Scientific and Industrial Research Organization, Canberra, Australia, 1981).

36. H. Gordon and D. Castano, "Coastal zone color scanner atmospheric correction algorithm: multiple scattering effects," Appl. Opt. **26,** 2111 (1987).

37. W. Blattern, H. Horak, D. Collins, and M. Wells, "Monte Carlo studies of the sky radiation at twilight," Appl. Opt. **13, 534** (1974).

38. R. Stavn and A. Weidemann, "Optical modeling of clear oceanlight fields: Raman scattering effects," Appl. Opt. **27, 4002–4011** (1988).

39. R. Stavn and A. Weidemann, "Raman scattering in ocean optics: quantitative assessment of internal radiant emission," Appl. Opt. **31,** 1294–1303 (1992).

40. D. Brine and M. Iqbal, "Diffuse and global solar spectral irradiance under cloudless skies," Sol. Energy **30,** 447–453 (1983).

41. T. Petzold, "Volume scattering functions for selected ocean waters," SIO Ref. 72–78 (Scripps Institution of Oceanography, La Jolla, Calif., 1972).

42. A. Morel, "Optical properties of pure water and pure sea water," in *Optical Aspects of Oceanography,* N. G. Jerlov and E. S. Nielsen, eds. (Academic, New York, 1974), pp. 1–24.

43. R. Smith and K. Baker, "Optical properties of the clearest natural waters (200–800 nm)," Appl. Opt. **20,** 177–184 (1981).

44. L. Prieur and S. Sathyendranath, "An optical classification of coastal and oceanic water based on the specific spectral absorption curves of phytoplankton pigments, dissolved organic matter, and other particulate materials," Limnol. Oceanogr. **26,** 671–689 (1981).

45. H. Gordon and A. Morel, "Remote assessment of ocean color for interpretation of satellite visible imagers, a review," in *Lecture Notes on Coastal and Estuarine Studies* (Springer Verlag, Berlin, 1983), Vol. 4.

46. M. Lewis, J. Cullen, and T. Platt, "Phytoplankton and thermal structure in the upper ocean: consequences of nonuniformity in chlorophyll profile," J. Geophys. Res. **88,** 2565–2570 (1983).

47. T. Platt and S. Sathyendranath, "Oceanic primary production: estimation by remote sensing at local and regional scales," Science **241,** 1613–1620 (1988).

48. S. Porto, "Angular dependence and depolarization ratio of the Raman effect," J. Opt. Soc. Am. **56,** 1585–1589 (1966).

49. R. Preisendorfer, *Properties,* Vol. V of Hydrologic Optics (U.S. Department of Commerce, Pacific Marine Environmental Laboratory, Seattle, Wash., 1976).

50. G. Kattawar and G. Plass, "Asymptotic radiance and polarization in optically thick media: ocean and clouds," Appl. Opt. **15,** 3166–3178 (1976).

51. R. Stavn, R. Schiebe, and C. Gallegos, "Optical controls on the radiant energy dynamics of the air/water interface: the average cosine and the absorption coefficient," in *Ocean Optics VII,* M. A. Blizard, ed., Proc. Soc. Photo-Opt. Instrum. Eng. **489,** 62–67 (1984).

52. G. Plass, T. Humphreys, and G. Kattawar, "Ocean–atmosphere interface: its influence on radiation," Appl. Opt. **20,** 917–931 (1981).

53. H. van de Hulst, *Multiple Light Scattering: Tables, Formulas, and Applications* (Academic, New York, 1980), Vol. 1.

54. L. Prieur and A. Morel, "Etude theorique du regime asymptotique: relations entre caracteristiques optiques et coefficient d'extinction relatif a la penetration de la lumiere du jour," Cah. Oceanogr. **23,** 35 (1971).

55. J. Mueller and R. Austin "Ocean optics protocols for SeaWiFS validation," SeaWiFS Project Tech. Rep. Vol. 5, S. B. Hooker and E. R. Firestone, series eds., NASA Tech. Memo. 104566 (National Aeronautics and Space Administration, Washington, D.C., July 1992).

56. H. Gordon, "Ship perturbation of irradiance measurements at sea. I: Monte Carlo simulations," Appl. Opt. **24,** 4172–4182 (1985).

57. C. Adams and G. Kattawar, "Radiative transfer in spherical shell atmospheres: Rayleigh scattering," Icarus **35,** 139–151 (1978).

58. G. Kattawar and C. Adams, "Radiative transfer in spherical shell atmospheres. II. asymmetric phase functions," Icarus **35,** 436–449 (1978).

59. G. Kattawar, "Radiative transfer in spherical shell atmospheres. III. application to Venus," Icarus **40,** 60–66 (1979).

60. S. Chandrasekhar, *Radiative Transfer* (Dover, New York, 1960).

61. K. Voss, "Electro-optic camera system for measurement of the underwater radiance distribution," Opt. Eng. **28,** 241–247 (1989).

62. K. Voss, "Use of the radiance distribution to measure the optical absorption coefficient in the ocean," Limnol. Oceanogr. **34,** 1614–1622 (1989).

Reprinted from

Ocean Optics XII

13–15 June 1994
Bergen, Norway

Geometrical light field parameters for improving remote sensing estimates of the backscattering coefficient for the marine hydrosol

Robert Hans Stavn

Department of Biology
University of North Carolina at Greensboro
Greensboro, NC 27412

Alan Dean Weidemann

Naval Research Laboratory
Code 7331
Coupled Dynamic Processes
Stennis Space Center, MS 39529

ABSTRACT

The backscattering coefficient of the marine hydrosol is recognized as an important optical parameter to extract from the radiance and irradiance data of the hydrosol. One of the more promising algorithms for extracting this parameter, utilizing remotely sensed reflectance, has been proposed by Zaneveld. He arrived at his algorithm by integrating the radiative transfer equation and simplifying the resultant geometrical shape factors of the light field in the algorithm. We have studied the implications of the simplified algorithm with the Naval Research Lab (NRL) optical model, a Monte Carlo simulation of the radiative transfer equation using standard absorption and elastic scattering coefficients for the water molecule, organic matter, and minerogenic matter. The known inputs of inherent optical properties can be used with the radiant flux outputs to check and verify algorithms that invert the measured irradiance streams for inherent optical properties. The results indicate that the inversion of the backscattering coefficient from remoteley sensed reflectance is in error in the range of a 40% overestimate to a 10% underestimate of this parameter. The errors are dependent on both the solar angle and the constituents contributing to backscattering. Knowledge about the general shape of the backscattering function of a given hydrosol will be necessary for the most successful inversion algorithms.

2. INTRODUCTION

The propagation of light through the ocean, it's diversion into biological and physical processes, and it's reemittance into the atmosphere have been primary concerns of hydrologic optics. The algorithms related to ocean color and remote sensing are attempts to account for the various fates of light in the ocean based on the light that is sensed on a remote platform, either aircraft or satellites. A major goal is to invert the optical properties of the marine hydrosol from the properties of the remotely sensed light signal. From these data and relationships many processes can be studied, such as the primary production forced by the penetrating light field. One attempt to construct an algorithm for these purposes came from Zaneveld[1,2], based on radiative transfer theory. An important optical parameter to be inferred from this algorithm is the backscattering coefficient of the hydrosol, a significant factor in the generation of the nadir radiance, the major source of information for remote sensing.

The radiative transfer equation from radiative transfer theory relates the radiances and irradiances of the submarine light field to the inherent optical properties of the marine hydrosol. The inherent optical properties of the hydrosol, i.e. molecular properties, include total absorption $a_T(\lambda,z)$, total scattering $b_T(\lambda,z)$, and the volume scattering function $\beta(\gamma,\lambda,z)$. The wavelength dependence of the inherent optical properties and the light field itself will be implicit for the rest of this report. Zaneveld proposed an algorithm based on the remotely sensed reflectance, $RSR = L(\pi)/E_{od}$, the ratio of the nadir radiance to the downwelling scalar irradiance. He derived from the radiative transfer equation a functional relationship between the RSR, the total absorption coefficient, and the backscattering coefficient. The total scattering coefficient can be divided into forward scattering, b_b, and backward scattering, b_b, components. The total absorption and backscattering properties of the hydrosol are the most important in generating the remotely sensed signal. In this report we analyze Zaneveld's algorithm.

Monte Carlo methods provide the mode for analyzing the Zaneveld algorithm. We apply the NRL blue water model with appropriate extensions to account for biological components of open water and Case 1 type coastal waters of high phytoplankton and upwellings. The input parameters are the various inherent optical properties of the marine hydrosol and the output of the model is the irradiances generated by a particular hydrosol with two separate conditions of solar-skylight irradiation. Since we

know the backscattering coefficient a priori, it is possible to evaluate the Zaneveld algorithm's ability to determine the backscattering coefficient.

3. THEORY

Zaneveld formulated relationships to explain the propagation of the nadir radiance through the hydrosol derived from the radiative transfer equation. The propagation of any radiance through the hydrosol is given by:

$$\cos\theta \, \frac{dL(\theta,\phi,z)}{dz} = -cL(\theta,\phi,z) + L*(\theta,\phi,z) \tag{1}$$

where

$$L*(\theta,\phi,z) = \int_0^{2\pi} \int_0^{\pi} \beta(\gamma) L(\theta',\phi',z) \sin\theta' \, d\theta' \, d\phi' \,, \tag{2}$$

and

$$\cos\gamma = \cos\theta \cos\theta' - \sin\theta \sin\theta' \cos(\phi - \phi') \,, \tag{3}$$

where $L*(\theta,\phi,z)$ is the path function, $\beta(\gamma,z)$ is the volume scattering function for the angle between the θ,ϕ radiance trajectory and the θ',ϕ' trajectory of the radiance contributing a scattering component to the radiance, θ is the zenith angle, ϕ is the azimuth angle, z is the geometrical depth, and c is the beam attenuation coefficient which equals $(a_T + b_T)$, the absorption coefficient plus the total scattering coefficient. The path function represents the flux scattered into the radiance $L(\theta,\phi,z)$ from all other radiances $L(\theta',\phi',z)$ at depth z. Next restrict our consideration to the radiative transfer of the nadir radiance $L(\pi)$, no azimuth information needed

$$-\frac{dL(\pi,z)}{dz} = -cL(\pi,z) + L*(\pi,z) \tag{4}$$

Assuming that the path function is continuous from $0 - \pi$ radians, we can divide Eq. (2) into a component integrated over the downwelling hemisphere and a component integrated over the upwelling hemisphere

$$L*(\pi,z) = \int_0^{2\pi} \int_0^{\pi/2} \beta(\pi - \theta',z) L(\theta',\phi',z) \sin\theta' \, d\theta' \, d\phi' \tag{5}$$

$$+ \int_0^{2\pi} \int_{\pi/2}^{\pi} \beta(\pi - \theta',z) L(\theta',\phi',z) \sin\theta' \, d\theta' \, d\phi' \,,$$

and

$$L*(\pi,z) = f_b(z) \frac{b_b(z)}{2\pi} E_{od}(z) + f_L(z) b_f L(\pi,z) \,, \tag{6}$$

where $(\pi-\theta') = \gamma$, $f_b(z)$ is the backscattering shape factor at depth z, and f_L is the forward scattering shape factor. It is readily seen that backscattering contributes to the nadir radiance from the downwelling hemisphere and forward scattering contributes to the nadir radiance from the upwelling hemisphere. The mean value theorem of calculus allows us to define a function that replaces the volume scattering function under the first integral of Eq. (5) and remove the volume scattering function while the radiances of the downwelling hemisphere are integrated to give the downwelling scalar irradiance, E_{od}. The function that is equivalent to $\beta(\pi-\theta',z)$ is $f_b(z)b_b(z)/2\pi$ where the $f_b(z)$ backscattering shape factor accounts for the difference between the "mean backscattering function" and the volume scattering function in the backward scattering angles. The $f_b(z)$ function can be either greater than or less than one. Furthermore, the nadir radiance, $L(\pi,z)$, is removed from the second integral of Eq. (5) and the $\beta(\pi-\theta',z)$ function is integrated to give b_f. If the upwelling radiance distribution were perfectly uniform, then the nadir radiance multiplied by the forward scattering coefficient would give the forward scattered contribution to the nadir radiance. The forward scattering coefficient f_L accounts for any deviation of the above condition from the actual upwelling radiance distribution. Substituting Eq. (6) into Eq. (4)

$$-\frac{dL(\pi,z)}{dz} = -cL(\pi,z) + f_b(z)\frac{b_b(z)}{2\pi}E_{od}(z) + f_L(z)b_f(z)L(\pi,z) \ ,$$

recalling

$$\frac{dL(\pi,z)}{dz} = -k(\pi,z)L(\pi,z) \ ,$$

and substituting

$$RSR(z) = \frac{L(\pi,z)}{E_{od}(z)} = \frac{f_b(z)\dfrac{b_b(z)}{2\pi}}{k(\pi,z)+c(z)-f_Lb_f(z)} \qquad (7)$$

In order to solve Eq. (7) we are required knowledge of the absorption coefficient and of the shape factors[3]. Zaneveld[1] estimated the range of the shape factors utilizing knowledge of sunny and overcast radiance distributions in the surface layers and Mie calculations estimating volume scattering functions for an assumed range of particle sizes and refractive indices. The reported range for f_b was 0.810 - 1.267 while that for f_L was 1.001 - 1.111. Zaneveld then concluded that, to within 30% error, the total backscattering coefficient could be determined if one assumed $f_b = f_L = 1.0$. The absorption coefficient would be determined by independent methods[3].

Inversion attempts that ignore the geometry of the light field and the shape of the volume scattering function can be hazardous however[4,5]. Thus, the approximation of unity for the two shape factors enumerated above is open to question, and Monte Carlo methods were employed to investigate the utility of these approximations. The NRL optical model, extended from blue water to coastal waters[3], was used with known inputs for water, organic matter, and minerogenic matter. With the radiance output of this model and the known input of inherent optical properties, the f_b and f_L parameters can be calculated directly. The inversions made from Zaneveld's algorithm on the same data can be determined and compared with the known backscattering coefficient and the shape factors. The backscattering coefficient is determined by rearranging Eq. (7) after substituting $(a_T + b_T)$ for c

$$b_b(z) = \frac{L(\pi,z)}{E_{od}(z)} \ \bullet \ \frac{\left[k(\pi,z)+a(z)+b_f(1-f_L)\right]}{\left[f_b/2\pi - L(\pi,z)/E_{od}(z)\right]} \qquad (8)$$

This exact equation is then converted to the following when the shape factors have been assumed equal to unity

$$b_b(z) = \frac{L(\pi,z)}{E_{od}(z)} \cdot \frac{[k(\pi,z)+a(z)]}{[1/2\pi - L(\pi,z)/E_{od}(z)]} \cdot \tag{9}$$

4. METHODS

The NRL Blue Water model[6] has been extended in this study to include events occurring from open ocean to coastal Case 1 waters. Scattering and absorption have been partitioned into the following components: algae, heterotrophic bacteria, detrital (organic), dissolved colored organic material (gelbstoff), quartz-like material, and molecular water. The model is parameterized to chlorophyll concentration and simulations were made in the range from 0.05 mg/m³ - 20.0 mg/m³ . In keeping with an interest in such problems as utilizing remote sensing data to determine chlorophyll levels, the wavelength for all simulations was 440 nm. At this wavelength the effects of internal sources of radiation, water Raman scattering and organic fluorescence, were felt to be minimal so they were not included in the simulation. Internal sources can be included easily if necessary. The power of the Monte Carlo technique is the ability to study the individual effects of each and every component in the processes of absorption and scattering, then to extract which component appears to dominate. The algal component is further subdivided into two parts: a small cell component (Chlorophyll 1.0 mg/m³) and a large cell component (Chlorophyll > 1.0 mg/m³) which taken together are referred to as the "standard model." The two cell components were also used in the total chlorophyll range, however, to study the effects of the model assumptions. The criterion for division between "small" and "large" algal cells was a cellular diameter of 2μm. The small algal/cyanobacterial cell is felt to be typical of open ocean conditions and the larger cell model was felt to be typical of coastal-type conditions[7,8] . The complete array of inherent optical properties and their sources are discussed in Weidemann and Stavn[3] .

The model simulations are carried out at solar zenith angles of 11° (air mass 1) and 60° (air mass 2) with 33.8% (air mass 1) and 52.4% of the global radiation due to skylight[9]. All simulations are for homogeneous conditions with a flat water/air interface.

The output of the Monte Carlo simulations, radiances and irradiances, is combined with the input of inherent optical properties to calculate values of f_b and f_L. Then the Zaneveld algorithm (Eq. 9) is used to estimate b_b for the marine hydrosol of a particular chlorophyll concentration and sky condition. The estimated b_b is then compared with the known b_b that was used in the Monte Carlo model to generate the radiance and irradiance output. The estimate of the error in b_b is made over one attenuation length ($1/K_d$) to conform with results of other studies indicating that 90% of the water-leaving radiance utilized in passive remote sensing studies is the result of interactions within the first attenuation length at the surface[10] . There were from 4 to 7 depth increments in each surface attenuation length in the model runs. At each depth increment b_b was estimated from Eq. (9) and the percent error was defined as

$$\bar{\varepsilon} = \frac{b_b(\text{RSR}) - b_b(\text{actual})}{b_b(\text{actual})} \times 100 \quad . \tag{10}$$

The "mean percent error" was the average of calculations made from Eq. (10) over the depth increments that comprised one attenuation length.

5. RESULTS

Air mass 1 results for the mean percent error calculation and the backscattering shape factor are plotted in Fig. 1. We see that the mean percent error of the b_b estimate, for chlorophyll concentrations less than 1 mg/m³, are in the range of 35 - 48% with the values appearing to vary around the 38% level. The f_b values in the same chlorophyll range are about 1.34 - 1.41. Both the mean percent error and the f_b values drop precipitously as chlorophyll concentration increases beyond 1 mg/m³ . At the maximum concentration of chlorophyll (20 mg/m³), the mean percent error drops to about 12% and the f_b value drops to about 1.02.

The air mass 2 results are plotted in Fig. 2. Here the mean percent error is about 10% at 0.05 mg/m chlorophyll concentration and it drops steadily to about 1% at 2 mg/m³ . The f_b values in the same chlorophyll range are from about 1.04 to 0.98. The increase in chlorophyll concentration up to 20 mg/m³ results in a mean percent error of - 8% and an f_b value of about 0.85.

In Table 1. we have the results of f_b calculations partitioned among the components of the model and for air masses 1 and 2.

Each component makes a consistent contribution to the shape factor no matter what the chlorophyll concentration, so the results at 1 mg/m³ chlorophyll concentration were chosen as a "median" value of chlorophyll concentration with the individual component contributions essentially constant over the entire chlorophyll range.

Table 1. Shape Factors at 1 mg/m³ Chlorophyll, 0 m depth, 440 nm

	$f_{b\ total}$	$f_{b\ water}$	$f_{b\ quartz}$	$f_{b\ bacteria}$	$f_{b\ algae}$
Air Mass 1	1.47	1.39	2.40	0.85	0.57
Air Mass 2	0.998	1.15	0.85	0.13	0.72

The f_b value for the total hydrosol changes, but the individual components do not -- the cause of the variation in the total f_b value is a weighted average of the component f_b values. The water component appears to have the strongest effect on the total f_b value while quartz-like material would be next in effect. This weighting changes with increase in chlorophyll and causes the total f_b to decrease with increase in chlorophyll as is seen in Figs. 1 and 2. The f_b values decrease from air mass 1 to air mass 2 with the exception of the algal component.

6. DISCUSSION AND CONCLUSIONS

The initial prediction of Zaneveld that the error in utilizing his algorithm would be approximately 30% is an adequate first order assertion. We see from the data in Fig. 1 and Fig. 2 however that this error range is not one of random error but rather of systematic error caused by at least two different factors: solar-sky radiance distributions and relative concentration of optically active components of the hydrosol. In open ocean water the error of estimate is consistently high (the backscattering coefficient is consistently overestimated) and greater than was predicted. As chlorophyll concentration increases and the Case 1 water becomes more coastal in quality the error of estimate for the backscattering coefficient decreases under air mass 1 conditions. The error of the backscattering estimate under air mass 2 conditions is lower in the open ocean and decreases with increase in chlorophyll; however the error becomes negative (the backscattering coefficient is underestimated). The variation in the error and the f_b coefficient is hyperbolic in the range 1 mg/m³ to 20 mg/m³ for both air mass conditions but the asymptotes differ. The algorithm based on Eq. (9) systematically overestimates the backscattering coefficient at low chlorophyll values under air mass 1 conditions and systematically underestimates the backscattering coefficient at high chlorophyll values under air mass 2 conditions.

The other pattern that appears in Figs. 1 and 2 is that the systematic error inherent in Eq. (9) can be explained in large part by the assumption that $f_L = 0$. The magnitude of the mean percent error is tracked well by the magnitude of f_b for all chlorophyll concentrations, and the f_b value will often serve to predict the error in the algorithm. At high chlorophyll concentrations the error is not predicted well by the f_b value so that the assumption about f_L is probably coming into play and making a contribution to the overall error of inverting the b_b value.

The changes in the patterns of the backscattering shape factor can be explained in part by the changes in the optically active components of the hydrosol. Quartz-like material especially has an extremely high f_b value under air mass 1 conditions and apparently is instrumental in stimulating high values of the total f_b in the open ocean, the increase in chlorophyll and thus of algae brings the f_b value down with increase of chlorophyll. Under air mass 1 conditions the components average out to an approximate value of 1.0 at 20 mg/m³ chlorophyll concentration. Under air mass 2 conditions the components of the hydrosol have a different backscattering shape factor because the radiance distribution is different and the volume scattering function is thus interacting in a new fashion with the radiance field . We must recall that the assumptions of Eq. (9) are essentially that the radiance distribution is uniform and that the backscattering lobe of all the hydrosol components is uniform. Thus we see the need for detailed examination of interactions of all possible hydrosol components in proposing remote sensing algorithms. The interactions of the hydrosol components with the radiance field are highly individual, and any increase in one component such as from an algal bloom or storm-derived delivery of excess minerogenic material into coastal waters has the potential of significantly altering the upwelling radiance signal in a complex fashion.

7. SUMMARY

1. Errors in estimating the backscattering coefficient occur systematically, not randomly.

2. Separate regimes can be identified: an open ocean high error system (Chlorophyll < 1.5 mg/m³), and a coastal/upwelling low error system (Chlorophyll > 1.5 mg/m³).

3. The geometrical shape factors associated with the submarine light field are strongly correlated with the errors of estimation of the backscattering coefficient.

4. Geometrical shape factors are a function of solar angle and particulate composition; they are required for the most accurate estimates from remote sensing.

8. ACKNOWLEDGEMENTS

REFERENCES

1. J.R.V. Zaneveld, "Remotely sensed reflectance and its dependence on vertical structure: a theoretical derivation," *Apl. Opt.*, 21, 4146-4150, 1982.

2. J.R.V. Zaneveld, "An asymptotic closure theory for irradiance in the sea and its inversion to obtain the inherent optical properties," *Limnol. Oceanogr.*, 34, 1441-1452, 1989.

3. A.D. Weidemann and R.H. Stavn, "Error in predicting hydrosol backscatter from remotely sensed reflectance," submitted to *J. Geophys. Res.*

4. R.H. Stavn and J.R.V. Zaneveld, "Geometrical shape factors in remote sensing algorithms for backscattering: partitioning and estimating," submitted to *J. Geophys. Res.*

5. R.H. Stavn and A.D. Weidemann, "Shape factors, two flow models, and the problem of irradiance inversion in estimating optical parameters," *Limnol. Oceanogr.*, 34, 1426-1441, 1989.

6. R.H. Stavn and A.D. Weidemann, "Optical modeling of ocean light fields: Raman scattering effects," *Appl. Opt.*, 27, 4002-4010, 1988.

7. A. Morel and A. Bricaud, "Inherent optical properties of algal cells including picoplankton: Theoretical and experimental results," *Can. Bull. Fish. Aquatic Sci.*, 214, 521-559, 1986.

8. A. Morel, Y.-H. Ahn, F. Partensky, D. Vaulot, and H. Claustre, "*Prochlorococcus and Synechococcus*: A comparative study of their optical properties in relation. to their size and pigmentation," J. Mar. Res., 51, 617-649, 1993.

9. D.T. Brine and M. Iqbal, "Diffuse and global solar spectral irradiance under cloudless skies," *Solar Energy*, 30, 447-453, 1983.

10. H.R. Gordon and A. Morel, "Remote assessment of ocean color for interpretation of satellite visible imagery," in Lecture Notes on Coastal and Estuarine Studies, R.T. Barber, C.K. Mooers, M.J. Bowman, and B. Zeitschel, eds., pp. 1-113, Springer Verlag, New York, 1983.
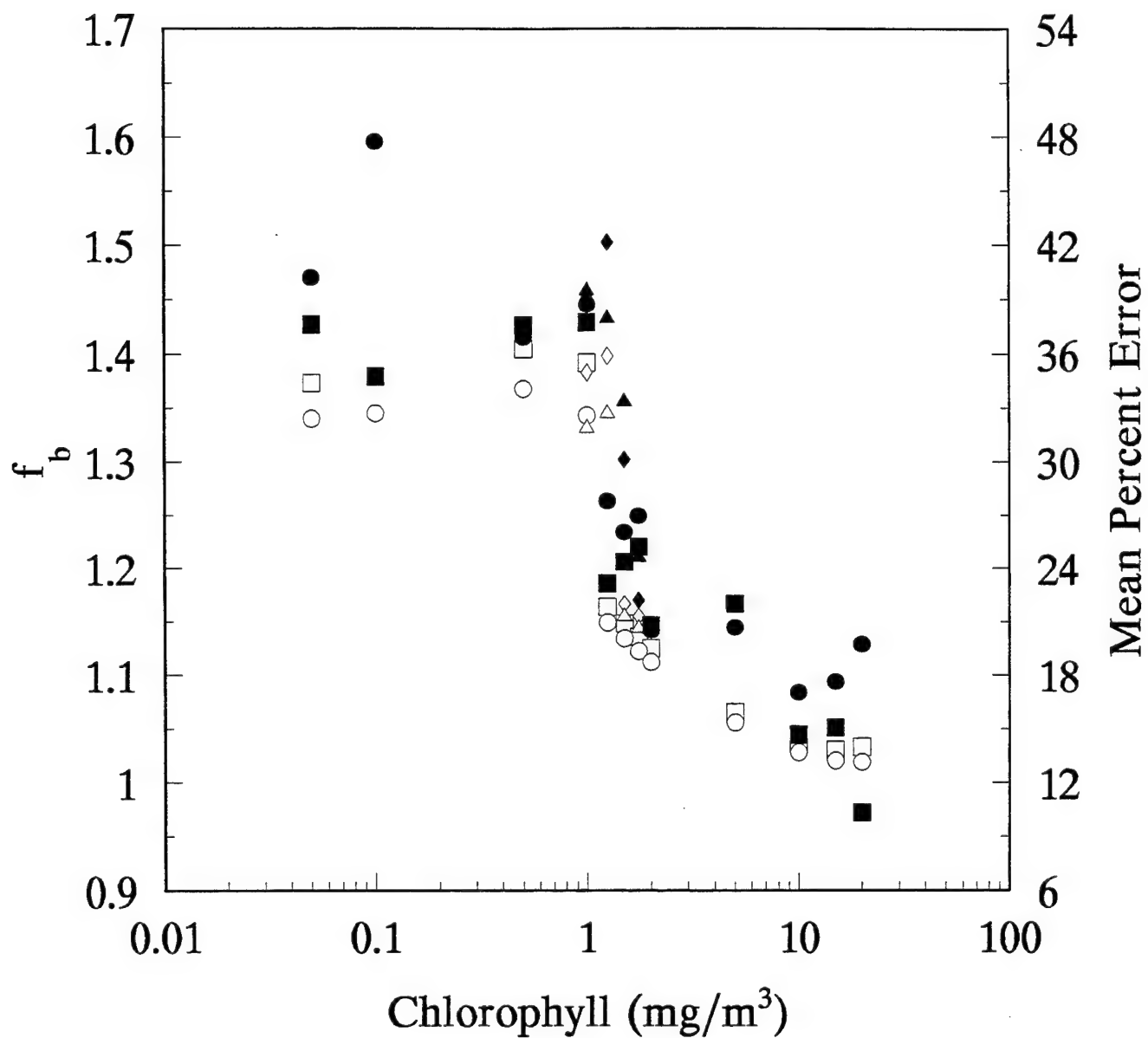
Figure 1. Backscattering shape factor f_b on left vertical axis and mean percent error of backscattering coefficient inversion on right vertical axis, air mass 1, 440 nm. For backscattering shape factor: $\square$ = standard model with bacteria, $\bigcirc$ = standard model without bacteria, $\diamond$ = small cell model with bacteria, $\triangle$ = small cell model without bacteria. For mean percent error: $\bullet$ = standard model with bacteria, $\blacksquare$ = standard model without bacteria, $\blacklozenge$ = small cell model with bacteria, $\blacktriangle$ = small cell model without bacteria.
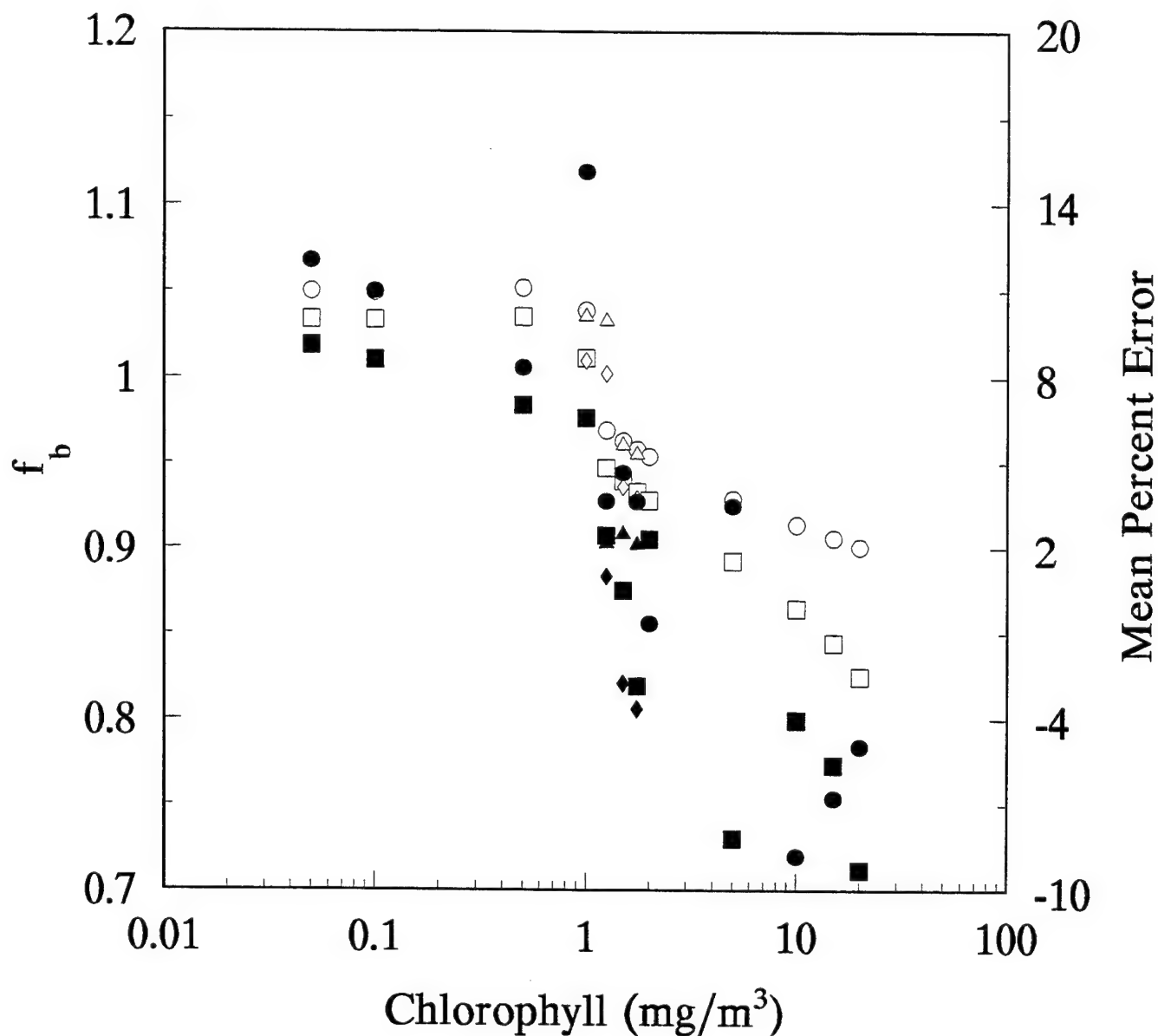
Figure 2. Backscattering shape factor f_b on left vertical axis and mean percent error of backscattering coefficient inversion on right vertical axis, air mass 2, 440 nm. For backscattering shape factor: □ = standard model with bacteria, O = standard model without bacteria, ◇ = small cell model with bacteria, △ = small cell model without bacteria. For mean percent error: ● = standard model with bacteria, ■ = standard model without bacteria, ◆ =small cell model with bacteria, ▲ = small cell model without bacteria.

Error in predicting hydrosol backscattering from remotely sensed reflectance

A. D. Weidemann,[1] R. H. Stavn,[2] J. R. V. Zaneveld,[3] and M. R. Wilcox[4]

Abstract. Monte Carlo simulations are carried out to determine the error in the inversion of backscattering from remotely sensed reflectance when geometrical shape factors of the light field are assumed to be unity. The results show that error in backscattering inversion can vary from a 40% overestimation to a 20% underestimation and is dependent on the solar angle and the hydrosol constituents contributing to backscattering. The simulations also demonstrate that for chlorophyll concentrations ranging from 0.05 to 20 mg m^{-3} the most dramatic change in the geometrical shape factor occurs near 1.0 to 1.5 mg m^{-3} chlorophyll. The potential importance of bacteria in influencing the shape factor and the subsequent effect of bacteria on the retrieval of the backscattering from remote sensing reflectance are shown. Quartzlike material's strong impact on geometrical shape factors and errors of retrieval of backscattering at low chlorophyll concentrations are also demonstrated. Remote sensing reflectance inversion schemes must include information about the backscattering function to be successful.

Introduction

Understanding the fundamental relationships of light propagation through the ocean, as they relate to ocean color or primary production, has been a primary goal for hydrologic optics. Driven by potential remote sensing capabilities, there is an increased interest in potential derivation or inversion of optical properties from ocean color [*Lee et al.*, 1994; *Zaneveld*, 1982, this issue]. Intrinsic to this approach are the relationships between optical properties of the hydrosol and the signal received by a remote sensing platform over defined wavelength intervals.

The transmission of light through the ocean is described by the equation of radiative transfer, which relates the spatially varying light field to the inherent optical properties. *Preisendorfer* [1976] defined inherent optical properties as those properties that are invariant with the local radiance distribution but may vary spatially due to inhomogeneities in the constituents of the water. These properties include the total absorption coefficient $a_T(\lambda, z)$, total scattering coefficient $b_T(\lambda, z)$, and the volume scattering function $\beta(\gamma, \lambda, z)$. Henceforth, the wavelength λ dependency will be implied. Vertical inhomogeneities are caused by the layering of biota or inorganic particulates suspended in a density gradient, while horizontal variability occurs as a result of patchiness from physically driven upwelling, mesoscale features, local winds, coastal discharge, tidal action, or fine-scale turbulence [*Gallegos et al.*, 1990; *Dickey et al.*, 1991; *Marees and Wernand*, 1991]. At a molecular level, as light propagates, its

electromagnetic field interacts with the dielectric interfaces of various material constituents which include water, adsorbed microlayers, and the optical features of organic detritus, inorganic material, phytoplankton, viruses, and bacteria. At larger scales, such as those of most optical measurements, or at still larger scales, such as the ocean color radiance signal received by a satellite, there is integration in space and time, however, which makes inversion difficult in a horizontally varying medium. It is the derivation of the inherent optical properties from the remotely sensed reflectance (RSR) RSR = $L(\pi)/E_{od}$ (the ratio of nadir radiance to scalar downwelling irradiance) that this paper addresses.

The total scattering coefficient b is composed of the forward b_f and backward b_b scattering components. For a remotely sensed signal it is the relationship between the backscattering and total absorption coefficients that is significant for most realistic oceanic conditions. Therefore the hydrosol backscattering and absorption coefficients are often used in modeling light propagation and signal return for both active and passive systems. About 90% of the water-leaving radiance is due to scattering events occurring within the first attenuation length [*Gordon and Clark*, 1980; *Gordon and Morel*, 1983]. Our goal has been to develop and evaluate inversion techniques that permit inherent optical properties, such as the backscattering coefficient, to be derived from remote sensing reflectance.

The use of the more easily measured apparent optical, or even biological, properties has been put forth to circumvent the intrinsic difficulties in measurements of absorption and scattering or backscattering and also to determine the relationship that the apparent optical properties have with the inherent properties. *Morel* [1988] and *Gordon et al.* [1988] presented techniques for estimation of backscattering from chlorophyll derived from the coastal zone color scanner (CZCS) imagery (i.e., the radiances received by the CZCS). *Lee et al.* [1994] have developed a model whereby reflectance ratios measured remotely are used to predict the ratio

---

[1]Naval Research Laboratory, Stennis Space Center, Mississippi.
[2]Department of Biology, University of North Carolina at Greensboro.
[3]College of Oceanic and Atmospheric Sciences, Oregon State University, Corvallis.
[4]Neptune Sciences, Incorporated, Slidell, Louisiana.
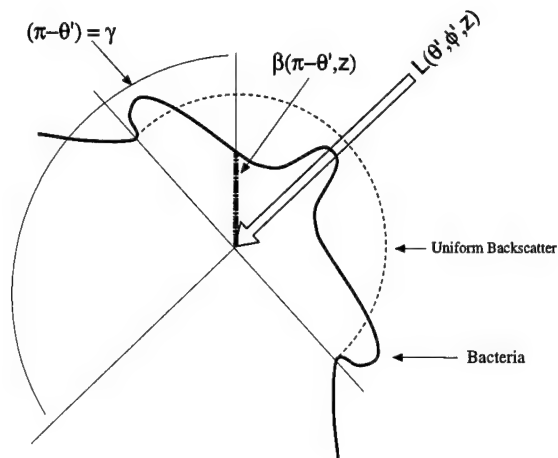
Figure 1. Source of radiant energy scattered into the nadir radiance $L(\pi, z)$ from any other radiance $L(\theta', \phi', z)$ at depth z. Backscattering lobe of the volume scattering function $\beta(\gamma, z)$ for bacteria is compared with uniform backscatter. For a special case of nadir radiance, scattering angle $\gamma = (\pi - \theta')$.

of b_b to Q (where Q is the ratio of upwelling irradiance to the upwelling nadir radiance). However, it has been shown that the value of Q can vary over more than an order of magnitude [*Morel and Gentili*, 1993]. In addition, the reflectance ratio R, defined as the upwelling plane irradiance divided by the downwelling plane irradiance, varies strongly as a function of solar angle and the shape of the hydrosol volume scattering function [*Gordon*, 1989; *Morel and Gentili*, 1993]. Furthermore, while the absorption coefficient is largely a function of the biota, the scattering and backscattering may or may not correlate with the living biomass present [*Kitchen and Zaneveld*, 1990]. Consequently, the estimation of hydrosol backscattering from only biological information or a derived biological parameter is tenuous, and a more analytical approach to derive backscattering is desirable.

An analytic approach for retrieval of the inherent optical properties was put forth by *Zaneveld* [1982, this issue] in which the backscattering and absorption are simple functions of the remotely sensed reflectance. Since remotely sensed reflectance as viewed by a satellite is only measurable on clear days, one can hypothesize that the absorption coefficient used in Zaneveld's approach can be reasonably determined from the refracted solar angle and the attenuation coefficient for the upwelling nadir radiance. Here we present results of Monte Carlo simulations with known absorption and scattering coefficients and phase functions as inputs so that the backscattering is known a priori. The output of the simulations is used to calculate the backscattering coefficient and then compare it with the known input values of b_b. We evaluate the retrieval of backscattering under the assumption that absorption can be reasonably estimated or that at least $(a + b_b)$ is a linear function of $k(\pi)$ (where $k(\pi)$ is the vertical attenuation coefficient for upwelling nadir radiance) over a wide range of conditions. Since the volume scattering functions are also known inputs, we are able to investigate the question of whether the shape of the hydrosol backscattering lobe, usually assumed to be uniform, has any effect on the retrieval of the inherent

optical properties. The geometrical shape factors from *Zaneveld*'s [1982, this issue] formulation allow us to analyze this question quantitatively. We then demonstrate strengths and weaknesses of this formulation and show the importance of water, bacteria, and quartzlike material in determining the remote sensing reflectance signal for chlorophyll concentrations less than 1.0 mg m^{-3}. At higher concentrations of chlorophyll we show the important effects of phytoplankton on the remote sensing reflectance.

Theory

Zaneveld [1982] proposed a formulation of the radiative transfer equation for upwelled nadir radiance (a zenith angle of 180°) which required appropriate geometric shape factors, f_b and f_L, for the interaction of the volume scattering function and the radiance distribution. In its original form the equation for radiative transfer for a horizontally non-varying field in the absence of internal sources is given by

$$\cos \theta \, \frac{dL(\theta, \phi, z)}{dz} = -c(z)L(\theta, \phi, z) + L^*(\theta, \phi, z),$$
(1)

where

$$L^*(\theta, \phi, z)$$
$$= \int_0^{2\pi} \int_0^{\pi} \beta(\gamma, z)L(\theta', \phi', z) \sin \theta' \, d\theta' \, d\phi' \quad (2)$$

is the path radiance, and

$$\cos \gamma = \cos \theta \cos \theta' - \sin \theta \sin \theta' \cos (\phi - \phi'), \quad (3)$$

where L is the radiance in watts per square meter per steradian, θ is the zenith angle, ϕ is the azimuth angle, z is the geometrical depth in meters, c is the beam attenuation coefficient equal to the absorption coefficient plus the total scattering coefficient $(a + b)$, and $\beta(\gamma, z)$ is the volume scattering function at depth z with the scattering angle γ. The path function represents the flux scattered into the radiance $L(\theta, \phi, z)$ from all other radiances of the light field located at zenith angle θ' and azimuth angle ϕ'. Figures 1 and 2 illustrate the geometry of backscattering from a bacterialike particle and a quartzlike particle into the nadir radiance. Considering only the upwelling nadir radiance and assuming that the scattering and radiance distribution functions are continuous in the region $(\pi/2, \pi)$, *Zaneveld* [1982] showed that the remotely sensed reflectance can be rigorously described by (4):

$$\text{RSR} = \frac{L(\pi, z)}{E_{od}(z)} = \frac{f_b \dfrac{b_b(z)}{2\pi}}{k(\pi, z) + c(z) - b_f(z)f_L(z)}, \quad (4)$$

where $k(\pi, z)$ is the attenuation coefficient of the nadir radiance and f_b and f_L are defined by *Zaneveld* [this issue] as

$$f_b(z) = \frac{\displaystyle\int_0^{2\pi} \int_0^{\pi/2} \beta(\pi - \theta', z)L(\theta', \phi', z) \sin \theta' \, d\theta' \, d\phi'}{\dfrac{b_b(z)}{2\pi} E_{od}(z)},$$
(5)

$$f_L(z) = \frac{\int_0^{2\pi} \int_{\pi/2}^{\pi} \beta(\pi - \theta', z) L(\theta', \phi', z) \sin \theta' \, d\theta' \, d\phi'}{b_f(z) L(\pi, z)}$$

(6)

The meaning of the backscattering shape factor f_b becomes clear from (5); it is the ratio of the actual radiant flux backscattered into the nadir radiance to the predicted back-scattered radiant flux. Use of E_{od} and $L(\pi, z)$ in these equations implies uniformity of radiances in the downwelling and upwelling hemispheres, respectively. In addition, the backscattering lobe of the volume scattering function is also assumed to be uniform. The geometrical shape factors f_b and f_L modify this to account for nonuniformity in the radiances in each hemisphere and in the backscattering lobe of the volume scattering function. This parameterization of the radiative transfer equation requires specification of these two factors.

To evaluate the potential errors of (4), the extreme or end-member values of the shape factors were required. Employing radiance distributions representative of diffuse and sunny skies and particle size distributions following Junge-type distribution with slopes of 3 and 5 with refractive indices ranging from 1.02 to 1.25, values for f_b and f_L were calculated. For *Zaneveld*'s [1982] test conditions these ranged from 1.001 to 1.111 for f_L and 0.810 to 1.267 for f_b. With strong arguments that f_L makes only a minor contribution, *Zaneveld* [1982] concluded that, to within 30% error, the total backscattering coefficient could be determined if f_b and f_L were assumed to be unity. This technique requires determination of the absorption coefficient from either *Gershun*'s [1939] equation or the refracted solar zenith angle and $k(\pi)$ (to one attenuation length) calculated from remote sensing. The technique assumes that $k(\pi) = k_\infty$ for extension of the remote sensing reflectance to a determination of the inherent optical properties.

Stavn and Weidemann [1989], however, have shown that inversion attempts neglecting shape parameters are sensitive to the radiance distribution of the light field. The shape of the radiance distribution was shown to significantly alter a generalized value of "hydrosol backscattering." The variability of the shape factor contains influences of forward and backscattering lobes on the upwelled irradiances and radiances. Therefore it became important to investigate the error in backscattering using *Zaneveld*'s [1982] inversion scheme of remotely sensed reflectance even if absorption could be reasonably approximated. At issue was the use of Zaneveld's exact equation (4) versus the approximation that f_b and f_L were unity in the upper one attenuation length of the water column and whether or not single or multiple scattering would dominate the remote sensing signal over this depth range.

To investigate *Zaneveld*'s [1982] relationship, Monte Carlo modeling with known inputs of absorption, scattering, and phase functions for water, organic detritus, quartzlike inorganic material, and phytoplankton is employed. In addition, bacteria are included to investigate the influence of Rayleigh-Gans-type scatterers on the predictability of the backscattering coefficient. It is the goal of this study to use the Monte Carlo simulation to determine the magnitude of error when inverting the backscattering coefficient using Zaneveld's formulation. First we take (4), substitute $(a + b)$
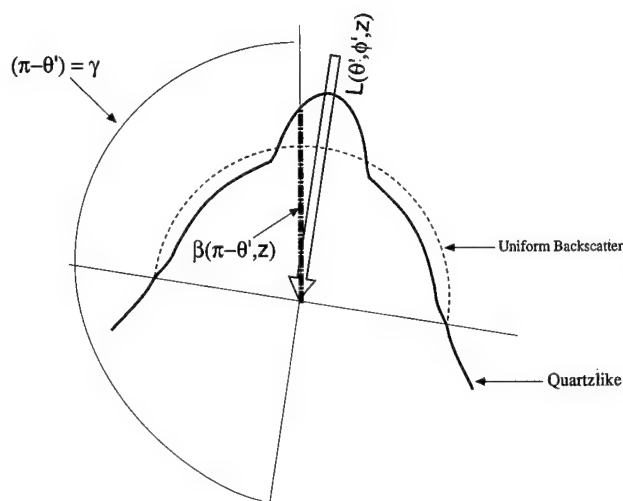

Figure 2. Source of radiant energy scattered into the nadir radiance $L(\pi, z)$ by quartzlike material. Symbols are same as in Figure 1.

for c, then, assuming that f_L and f_b are unity, rearrangement yields an expression for backscattering (equation (7)).

$$b_b(z) = \frac{\frac{L(\pi, z)}{E_{od}(z)} [k(\pi, z) + a(z)]}{\frac{1}{2\pi} - \frac{L(\pi, z)}{E_{od}(z)}}.$$

(7)

Using the irradiance and radiance outputs of the Monte Carlo simulations, we calculate backscattering from (7) as well as the actual values of f_b and f_L using (5) and (6). Once f_b is determined from the radiances and irradiances of the Monte Carlo output and the volume scattering functions in the model, then it is possible to calculate f_L as

$$f_L = \frac{[k(\pi, z) - a(z)]}{b_f(z)} - \frac{b_b(z)}{b_f(z)} \left[\frac{f_b(z) E_{od}(z)}{2\pi L(\pi, z)} - 1 \right] + 1.$$

(8)

The backscattering coefficient retrieved from the simplified RSR relation, equation (9), is then compared with the known backscattering coefficient. Among the relationships investigated is how the error in the retrieval of b_b compares to the f_L and f_b contributions and their deviation from unity. Furthermore, we can partition f_b into components due to molecular water, quartzlike material, etc., and consider which components tend to dominate.

Monte Carlo Model: Parameters and Constraints

The potential errors in the assumptions of the original *Zaneveld* [1982] algorithms stimulated studies to evaluate the effect of these assumptions on the extracted values of b_b. One outcome of these studies was validation of a new method [*Zaneveld*, this issue] for estimating the geometrical shape factor f_b from optical measurements of the shape of the backscattering function in the field.

We use the Monte Carlo method to simulate solutions to the radiative transfer equation under a variety of optical conditions. A series of Monte Carlo simulations at the U.S. Naval Oceanographic Office and the North Carolina Super-

computing Center utilized the Naval Research Laboratory (NRL) blue water model with some logical extensions. The NRL blue water Monte Carlo model is explained in some detail by *Stavn and Weidemann* [1988] and verified by *Mobley et al.* [1993]. The extensions that are applied to the model account for a variety of suspended materials tending to make the blue water model "green." Scattering and absorption are partitioned into components including algae, detritus (organic), dissolved colored organic material (gelbstoff), quartzlike material, and molecular water. The chlorophyll range of previous modeling efforts is extended to higher chlorophyll regimes (20 mg m^{-3}), which are more representative of coastal and upwelling conditions. The range of chlorophyll concentrations used in this study is 0.05 to 20.0 mg m^{-3}. Bacterial contributions to scattering and absorption are made through adjustment in the organic fraction. Therefore, while the total absorption and scattering coefficients do not change, with or without bacteria, their partitioning is altered. The impact of bacteria is particularly important in modifying the angular distribution of the backscattering function toward the nadir. Quartzlike material has a similar impact at low (<1 mg m^{-3}) chlorophyll concentrations.

Briefly, what shall henceforth be referred to as the "standard model" is as follows. The model simulations are carried out at 440 nm, near a chlorophyll absorption peak, with solar zenith angles of 11° (air mass 1) and 60° (air mass 2) with 33.8% (air mass 1) and 52.4% (air mass 2) of the global radiation due to skylight, respectively [*Brine and Iqbal*, 1983]. The parameterization of components of sky radiation to yield aerosol type are derived from *Baker and Frouin* [1987]. Since the model simulations are conducted for the blue region of the spectrum, internal sources, such as fluorescence and Raman scattering, are excluded. All simulations are for flat surface, optically homogeneous oceanic conditions. The absorption and total scattering coefficients are partitioned as

$$a_T = a_w + a_p + a_y + a_d \qquad a_d = a_o + a_{\text{bact}}$$

$$b_T = b_w + b_p + b_d + b_q \qquad b_d = b_o + b_{\text{bact}}$$

where the subscripts T, w, p, y, d, q, o, and bact refer to total, water, phytoplankton, yellow substances (dissolved), detrital, quartzlike material, organic (nonbacteria), and bacteria, respectively. The a_{bact} is assumed negligible and equal to zero so that $a_d = a_o$. The basic working of the Monte Carlo model involves generating photons that penetrate the marine hydrosol at an angle dependent on the solar zenith or the skylight distribution. The absorption and scattering coefficients become probabilities that determine whether a photon will be absorbed or continue but at a new trajectory. All the volume scattering functions of the suspended particles (quartzlike, organic detritus, bacteria, small algal cell, large algal cell) and the water molecule are used separately to generate different probability distributions invoked by separate calls to the random number generator. The penetrating photons in the model have a large range of possible photon-particle interactions which, we feel, allows for an accurate simulation of the photic fields of a series of marine hydrosols from open ocean to coastal-type upwelling type situations of case 1 waters. After 10 million photons have penetrated, their passages at various depths, with a constant

increment between the depths, are summed and radiances and irradiances can be determined. Information on radiances and irradiances can then be used, as they were in this study, to test the efficiency of algorithms that are simplifications of radiative transfer theory.

The absorption and total scattering coefficients for the constituents are extracted from the literature. Absorption and scattering by molecular water are those from *Smith and Baker* [1981] and *Morel* [1974]. The quartzlike material of the marine hydrosol is assumed to be nonabsorbing, while the scattering coefficient for this material is taken from data reported by *Kullenberg* [1968] at depths of 1500 to 2000 m in the Sargasso Sea. This quartzlike material is taken as a constant "background component" of the marine hydrosol. For the phytoplankton component of our marine hydrosol we have taken advantage of the extensive data on absorption and scattering of these cells from *Bricaud and Morel* [1986], *Morel and Bricaud* [1986], and *Bricaud et al.* [1988]. The absorption properties of the bacteria are taken from *Stramski and Kiefer* [1991], but since bacterial absorption was negligible, detrital absorption has been used in the scattering calculations for bacteria. Bacterial optical properties are also taken from *Morel and Ahn* [1990]. The scattering properties for the bacteria are derived from Mie theory [*Bohren and Huffman*, 1983], using a mean spherical diameter of 0.58 μm. The concentration of bacteria in the hydrosol is determined using relationships between bacteria concentration (cells per cubic meter) and chlorophyll concentration [Chl] (milligrams per cubic meter) as follows: 0.63×10^{12} cells m^{-3} for ≤ 0.5 mg m^{-3} chlorophyll and 0.91×10^{12}[Chl]$^{0.52}$ cells m^{-3} for >0.5 mg m^{-3} chlorophyll [*Cho and Azam*, 1990; *Cole et al.*, 1988]. The contributions to absorption from dissolved substances ($0.207a_T$) and organic detritus utilize regression relationships of absorption on the total scattering coefficient at 550 nm developed by *Prieur and Sathyendranath* [1981]. The total scattering coefficient for organic detritus was obtained by difference. That is, for any given chlorophyll concentration the total scattering coefficients for molecular water, quartzlike material, phytoplankton cells, and bacterial cells were summed and subtracted from the total scattering coefficient for the hydrosol at 550 nm, calculated from $b_T = 0.21$[Chl]$^{0.62}$ where [Chl] is the chlorophyll concentration [*Morel*, 1980].

One distinctive feature of the NRL optical model is that the volume scattering function of each constituent of the marine hydrosol is accounted for separately rather than applying a single "average volume scattering function" that remains constant even though chlorophyll concentrations vary. The volume scattering function for molecular water comes from *Morel* [1974], and the volume scattering function for the quartzlike material is taken from *Petzold*'s [1972] data for tongue-of-the-ocean (Atlantic Undersea Test and Evaluation Center (AUTEC)) with water subtracted. Two volume scattering functions are utilized for phytoplankton based on whether we are investigating open ocean water or more coastal-type case 1 water. The detailed criteria applied to these scattering functions will be explicated in our discussion of constraints applied to the optical parameters utilized in the model. The volume scattering functions are from *Bricaud and Morel* [1986], *Bricaud et al.* [1988], and Mie calculations for small (<2-μm diameter) cells with the absorption cross sections reported by Bricaud and Morel in various papers. The volume scattering function for particu-

late organic detritus was estimated from the data reported by *Petzold* [1972] for San Diego Harbor water, with molecular water subtracted.

Extensive constraints have been built into this model to assure compliance with the relationships between the optical parameters of the marine hydrosol as published in the literature. Absorption coefficients of the marine hydrosol and its components are more easily measured and arguably more reliable than the scattering measurements that have been available heretofore. Therefore we use the absorption properties and relationships to establish our hydrosol optical model. We then investigate the relevant scattering properties of the marine hydrosol, constrained by the absorption relationships. A "small-cell model" is utilized for ocean waters of ≤ 1 mg chlorophyll m^{-3} and a "large-cell model" for ocean waters of >1 mg chlorophyll m^{-3}. For chlorophyll concentrations at or below 1 mg m^{-3} the phytoplankton absorption and scattering coefficients are considered to be typical of a "small algal or cyanobacteria cell" with a diameter of <2 μm [*Bricaud and Morel*, 1986; *Morel and Bricaud*, 1986; *Bricaud et al.*, 1988], such as *Platymonas* species. The specific absorption coefficient is 0.0404 m^2 mg^{-1} g^{-1} and the portion of the scattering by phytoplankton in the backward direction b_{bp}/b_p is 0.000332. For chlorophyll concentrations >1.0 mg m^{-3} the model uses optical properties of a large algal cell (*Dunaliella* sp.) with a specific absorption of 0.0158 m^2 mg^{-1} and b_{bp}/b_p ratio of 0.0020. The large cell is believed to be more representative of phytoplankton in coastal and upwelling areas. *Carder et al.* [1986] and *Cleveland* [this issue] have bracketed these specific absorption coefficients for nearshore and open ocean environments. K. L. Carder (unpublished data, 1994) found that the specific absorption coefficient varied in a "hyperbolic" fashion from about 0.07 m^2 mg^{-1} in open water with low chlorophyll, declining rapidly to 0.016 m^2 mg^{-1} in high-chlorophyll regimes. The midpoint of the transition was near the chlorophyll concentration of 1 mg m^{-3}. *Cleveland* [1988] reported specific absorption coefficients of 0.015, 0.040, and 0.060 m^2 mg^{-1} in a series ranging from deep ocean systems to near-coastal systems. We conclude that the values used in our model are representative of those expected in natural conditions. Additionally, there have been reports on the relative concentration of particulate organic matter compared to living cells. The general trend is one of relatively high organic detritus concentration in low-chlorophyll, open ocean systems and relatively low organic detritus concentration in high-chlorophyll, near-coastal systems [*Morel*, 1988]. *Bricaud and Stramski* [1990] have reported quantitative estimates of the ratio of the absorption coefficient of particulate organic detritus to the absorption coefficient of all particulates at 440 nm, $a_o/(a_p + a_d)$, in our notation. They report a range in the detritus to total particulate absorption ratio of 60–80% at chlorophyll concentrations below 0.05 mg m^{-3} and a range of 5–24% at chlorophyll concentrations of 1.5 mg m^{-3}. The organic matter concentrations chosen for this model conform to these absorption ratios established.

The original limits on the scattering by the marine hydrosol at 550 nm were established by *Morel* [1980] and later modified [*Gordon and Morel*, 1983]. The limits for total scattering at 550 nm for case 1 ocean waters were from $b_T = 0.12[\text{Chl}]^{0.62}$ to $b_T = 0.45[\text{Chl}]^{0.62}$. Our estimate of the total scattering coefficient for organic detritus was obtained by difference, i.e., summing up all of the scattering components of the hydrosol except organic detritus and then subtracting this value at 550 nm from the power law for the total scattering coefficient established by Morel. We could have validly chosen any coefficient in this range from 0.12 to 0.45 and have been within the accepted range for total scattering of case 1 waters. After testing many coefficients of this power law, we arrived at the relationship of $b_T = 0.21[\text{Chl}]^{0.62}$. This power law exhibits a coefficient about midway between the limits established by Morel. The organic matter estimated by difference from this power law conforms to the absorption ratio for organic detritus to total particulate established by *Bricaud and Stramski* [1990]. Higher coefficients than 0.21 resulted in organic detritus concentrations that were too high in coastal ocean systems. The optical scattering relationships established at 550 nm were then corrected back to 440 nm by the λ^{-1} relationship for marine particulates when scattering cross sections for 440 nm were not known. Another check on these relations is to consider the backscattering coefficient measured by *Carder et al.* [1986] at various levels of chlorophyll in the Gulf of Mexico. The backscattering coefficient from our model, summed from the backscattering coefficients of the individual hydrosol components, conforms to the backscattering coefficient established by Carder et al. for chlorophyll concentrations at 1 mg m^{-3} or less. At higher chlorophyll concentrations our backscattering coefficient is less than that reported by Carder et al. However, Carder et al. admit that the high-chlorophyll waters they sampled were quite probably case 2 waters. In addition, when we compare our backscattering coefficient with the backscattering formula, parameterized to chlorophyll, proposed by *Morel* [1988], the coefficient now exceeds the predictions of Morel's formula by about 30%. To our knowledge, no other model or parameterization of case 1 waters conforms this well to Morel's backscattering formula. Regions of high chlorophyll may have more organic detritus than previously suspected, or perhaps more inorganic particulate must be accounted for as chlorophyll concentration increases. In addition, the specific scattering coefficient for our optical model varied from 1.23 m^2 mg^{-1} Chl at 0.05 mg Chl m^{-3} to 0.673 m^2 mg^{-1} Chl at 20 mg Chl m^{-3}, decreasing in a "hyperbolic" fashion on the semilog plot in accordance with the data range established by *Morel* [1987]. This model is probably representative of a rapid new growth algal bloom without any large significant inorganic quartzlike contributions above chlorophyll concentrations of 1.0 mg m^{-3}.

To assess the impact of dramatically different optical properties of phytoplankton on the inversion of backscattering from RSR, we made several "nonstandard" model runs. These simulations are carried out in the region of 1.0 mg m^{-3} chlorophyll. It is at this point where the simulations shift from a small-cell to a large-cell model. In the nonstandard simulations the large-cell characteristics are used at chlorophyll concentrations of 1 mg m^{-3} or less, and conversely, the small-cell characteristics are used at larger chlorophyll concentrations. The chlorophyll concentration of 1 mg m^{-3} was an important "hinge point" for many of the observations from these simulations, and it was important to establish what effect, if any, the change in cell models would have on the results.
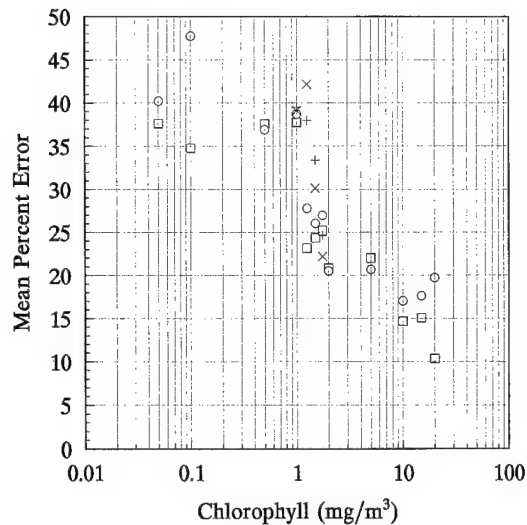
Figure 3. Mean percent error over one attenuation length, 440 nm, for backscattering retrieval as a function of chlorophyll for air mass 1 (11° solar angle), with squares indicating standard simulation with bacteria; circles, standard simulation without bacteria; crosses, nonstandard simulation (see text) with bacteria; and pluses, nonstandard simulation without bacteria.

Error in Retrieval of b_b: Standard Model

In order to conform with previous modeling efforts that have shown that 90% of the water-leaving radiance used in passive remote sensing is propagated from interactions that occur within the first attenuation length [Gordon and Morel, 1983], the retrieval of b_b from RSR via (7) is evaluated over the depth interval of one attenuation length ($1/K_d$). The inversion of b_b from RSR is parameterized as the "mean percent error" $\bar{\varepsilon}$ which is the average deviation between the input b_b and b_b recovered by (7) over all depth increments of the model from the surface to one attenuation length (a minimum of four model depth increments in low chlorophyll to a maximum of seven depth intervals in high-chlorophyll water). For each depth increment the mean percent error in b_b retrieval is defined as

$$\bar{\varepsilon} = \frac{b_b(\text{RSR}) - b_b(\text{actual})}{b_b(\text{actual})} \times 100 \qquad (9)$$

The model simulations suggest that Zaneveld's [1982] original contention that the inherent optical properties can be inverted with a certainty of $\pm 30\%$ is a reasonable first-order estimate (assuming absorption can be recovered independently). However, (7) does not give any indications of the systematic overestimation and underestimation of b_b that the model simulation output clearly indicates. For the Sun near the solar zenith (11°, air mass 1), (7) actually overestimates b_b by about 40% from 0.05 to 1.0 mg m^{-3} chlorophyll (Figure 3). Between 1.0 and 1.25 mg m^{-3} chlorophyll, Figure 3 indicates that the mean percent error in b_b drops to 25%. There is gradual improvement in the recovery of b_b between 1.25 and 20.0 mg m^{-3} chlorophyll. The mean percent error declines from an overestimate of 25% to an overestimate of about 15%. While there is considerable variability in the mean percent error, overall, the simulations

that include bacteria show a slight improvement in recovery of b_b.

The simulations demonstrate a strong dependency of solar angle on the retrieval of b_b using remote sensing reflectance (Figures 3 and 4). The error in retrieval of b_b for the air mass 2 (60° solar zenith) condition shows a "hyperbolic" shape similar to that from air mass 1, but with a downward displaced asymptote for low-chlorophyll concentrations. At low chlorophyll concentrations the mean percent error is only about 10%. There is then rapid improvement in b_b inversion between 1.0 and 2.0 mg m^{-3} similar to the air mass 1 case; the mean percent error at 2 mg m^{-3} is about 1%. However, at even higher chlorophyll concentrations the simulations show that (9) will underestimate b_b by about 6–9%. In addition, simulations at low chlorophyll concentrations with bacteria differ significantly from simulations using organic detritus to replace the bacterial component. There is much more scatter over the entire range of chlorophyll concentrations for air mass 2 over what is evident in the output for air mass 1. This variability is ascribed to the low solar angle and the low number of photons being backscattered into the nadir. We conclude from these results that (7) requires modification. Clearly, the retrieval of b_b is dependent on the solar angle and on the partitioning of the scattering into organic and bacterial components. The results furthermore suggest that f_b and f_L cannot be assumed to be unity as initially suggested, but rather, there is a systematic change in one if not both of these shape factors. The "random" assumption in the variability of f_b and f_L implied by Zaneveld [1982] is not present. The results also demonstrate a sudden change in the accuracy of the retrieval of b_b between 1.0 and 1.5 mg m^{-3} chlorophyll.

Analysis of f_L and f_b

We proceed to determine if either shape factor f_b or f_L or their combination is the cause of the systematic discrepancy between the recovered b_b and the input b_b. The values for f_L and f_b were calculated from (8) and (5). The effect of neglecting variance in the shape factors is manifested
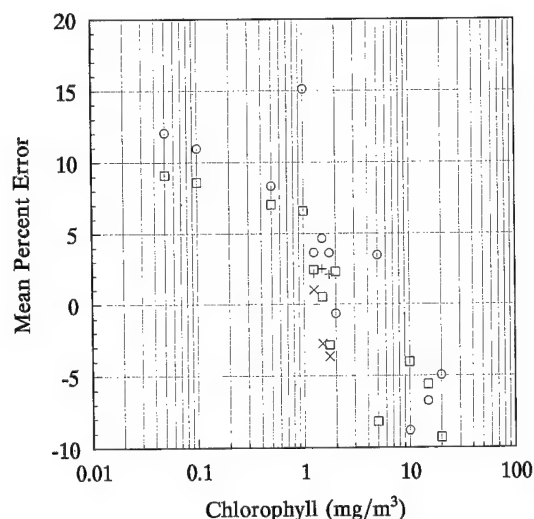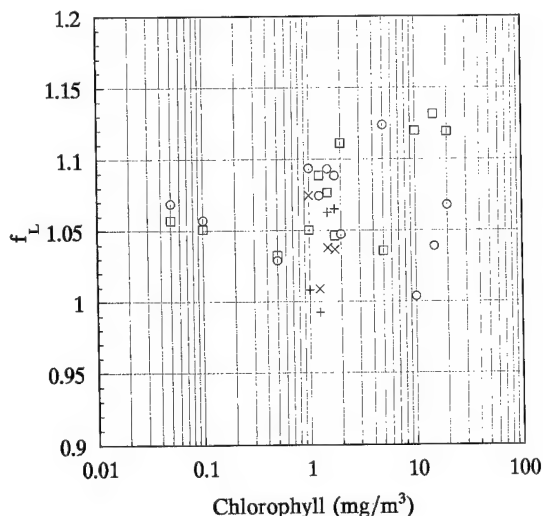

Figure 4. Mean percent error in backscattering retrieval as a function of chlorophyll for air mass 2 (60° solar angle); symbols as in Figure 3.
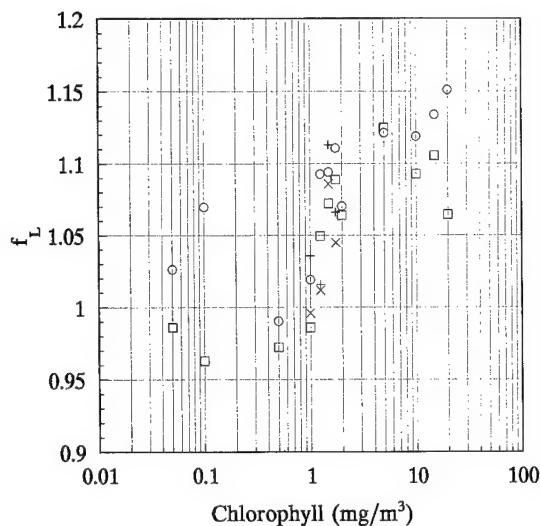
Figure 5. Shape factor f_L as a function of chlorophyll for air mass 1, all simulations; symbols as in Figure 3.
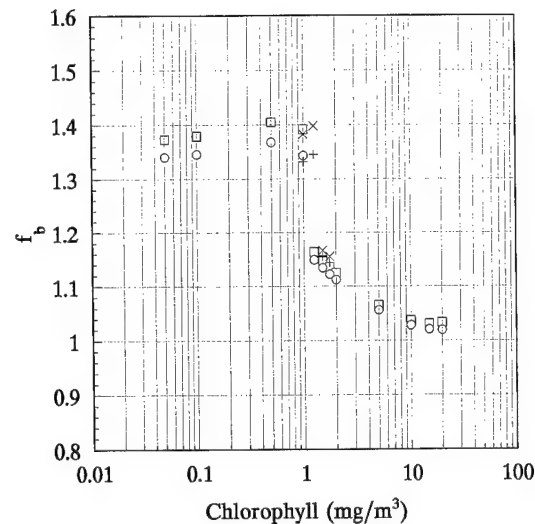

Figure 7. Shape factor f_b as a function of chlorophyll for air mass 1, all simulations; symbols as in Figure 3.

through the comparison of the exact (equation (4)) and the approximate solution (equation (7)) for RSR.

For f_L the differences between air mass 1 and air mass 2 results are small; f_L is not a strong function of solar angle (Figures 5 and 6). The range of f_L values is 0.963–1.152 which is broadened somewhat over the range reported by *Zaneveld* [1982]. One anticipates that for our simulations the near-surface radiance distribution will be strongly peaked in a forward direction, and thus f_L would not be expected to show large deviations [*Zaneveld*, 1982, this issue]. The sharper $\beta(\gamma)$ is in the forward direction, the less likely f_L is to show any great impact on the retrieval of b_b from remotely sensed reflectance. In addition, the exact solution (equation (4)) shows that f_L has only a small impact on the numerator through the modification of forward scattering b_f. In our simulations, f_L is nearly constant from 0.05 to 1.0 mg m^{-3} chlorophyll, with values of 1.0 and 1.07 for air mass 1 and air mass 2, respectively (Figures 5 and 6). The f_L

coefficient then increases to about 1.1 at the higher chlorophyll concentrations for both solar angles.

At scales too small to be significant in b_b retrieval there is a difference between air mass 1 and 2 in the importance of bacteria on f_L. For a solar angle of 11°, nearly all the f_L values are higher in those simulations without bacteria. However, the trend disappears or even shifts slightly to lower f_L values for the 60° solar angle.

Of more interest is the calculation of f_b for the model simulations (Figures 7 and 8). The range of f_b values averaged over the first attenuation length is 0.821–1.41 which extends *Zaneveld*'s [1982] range only at the high end. As (4) predicts, the retrieval of b_b from RSR is inversely proportional to f_b, and therefore changes in f_b are manifest in the retrieval of b_b from RSR. The values for air mass 1 range from 1.4 in the low-chlorophyll range (0.05–1.0 mg m^{-3}) to 1.02 at 20 mg m^{-3} chlorophyll (Figure 7). There is a sudden decrease in f_b that is characteristic of the change in the mean percent error at 1.25 mg m^{-3}. The shape is distinct and follows the hyperbolic shape exhibited in the mean percent error [*Stavn and Weidemann*, 1994]. Air mass 2 results show a similar trend, but the values for f_b are about 1.03 at low chlorophyll, decreasing to <0.9 at high chlorophyll concentrations (Figure 8). In contrast to f_L, there is a significant difference between f_b values for air mass 1 and air mass 2 when bacteria are present versus when they are absent. For the air mass 1 (11° solar angle) simulations, f_b is always higher with bacteria included; the converse is the case for air mass 2. Since f_b is dominated by the backscattering function and the radiance distribution, this result indicates that the volume scattering function in the backward direction is affected significantly by the presence or absence of the bacteria. This result indicated that further analysis into the effect on the shape factors caused by the partitioning of the constituents was required.

Figure 6. Shape factor f_L as a function of chlorophyll for air mass 2, all simulations; symbols as in Figure 3.

Partitioning of f_b

We can extend the analysis of f_b further by taking advantage of the parameterizations possible with Monte Carlo technique. Each component of b_b is evaluated separately in
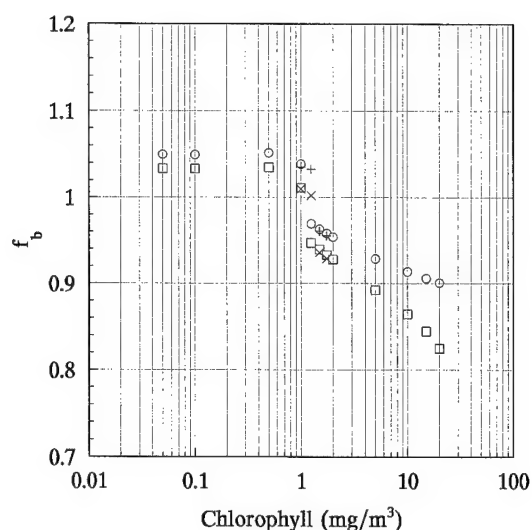
Figure 8. Shape factor f_b as a function of chlorophyll for air mass 2, all simulations; symbols as in Figure 3.

its effect on the photon flux, as each represents a different probability, and the same is true for the volume scattering function for each hydrosol component. All of the scattering coefficients are additive, and thus their contributions to a calculation of f_b from (5) are determined separately, appropriately weighted, and summed. That is, a shape factor f_b is determined for each individual component (water, algae, bacteria, organics, etc.) of the hydrosol. In Table 1 we have the backscattering shape factors evaluated for three chlorophyll concentrations (0.05, 1.0, and 20.0 mg m^{-3}) and the f_b values for each hydrosol component. The partitioning of the f_b coefficient among the hydrosol components as shown in Table 1 gives some indication as to why the f_b parameter is neither simple nor easy to dismiss. For example, individual hydrosol components vary in their f_b value by much more than the variation in the shape factor for the entire hydrosol (i.e., the weighted average). In contrast to the values for f_b of the entire hydrosol originally estimated by *Zaneveld* [1982], the shape factors in the surface layer can be as low as 0.118 for bacteria at a chlorophyll concentration of 20 mg m^{-3} and air mass 2 to as high as 2.596 for quartzlike material at 20 mg m^{-3} chlorophyll and air mass 1. Clearly, radical shifts in the concentration of hydrosol components strongly effects f_b; consider an algal bloom, a bloom of bacterial decomposers after an algal bloom has run its course, or

transport of quartzlike suspended matter into coastal waters by a river after a storm or just by disturbance of bottom sediments. The pattern that emerges from Table 1 is that for a given external radiance distribution the backscattering shape factor for each component is essentially unchanged, no matter what the chlorophyll concentration. However, because f_b is dominated by $\beta(\gamma)$ once $L(\theta, z)$ is defined, changes in the concentration of individual components will shift the weighting factor for each component f_b and alter the final backscattering shape factor for the entire hydrosol. For the low chlorophyll concentrations (0.05–1.0 mg m^{-3}) at air mass 1 the highest f_b values in the study are associated with the very high f_{bq} values for quartzlike material, which is apparently the major factor in causing high hydrosol f_b values. At the high chlorophyll concentration (20.0 mg m^{-3}) the value for f_b appears to be affected most strongly by the f_{ba} value associated with algae, although air mass 2 values would indicate some bacterial effect. In general, the bacterial effect on the hydrosol f_b value can vary from 3 to 12%.

The causes for the variation in the backscattering shape factor for individual hydrosol components are illustrated in Figures 1, 2, 9, and 10. The schematic diagrams of Figures 1 and 2 illustrate the geometry of the volume scattering function in the backward direction associated with a given downwelling radiance. In both cases we also illustrate the nonuniform volume scattering function in the backward direction for bacteria and quartzlike material. The figures graphically show how the bacterial volume scattering function in Figure 1 scatters less into the nadir radiance than would be predicted from the assumption of uniformity of the volume scattering function in the backward direction. Conversely, in Figure 2 the quartzlike material will scatter more into the nadir radiance than would be predicted by the assumption of uniformity of the backscattering function. The interactions leading to the typical backscattering shape factors for bacteria and quartzlike material are illustrated quantitatively in Figures 9 and 10, where plots of radiance distributions and the backscattering function for quartzlike material and bacteria are shown. In Figure 9 we have plotted the downwelling zonal radiance distribution $L(\Theta', 2\pi)d\omega$ against the backscattering lobe of the volume scattering function $\beta(\gamma)$ of the quartzlike material. This plot of zonal radiance (integrated over a 2π azimuth angle) multiplied by $d\omega$ represents the integral term of (5). We see that the dominant zonal radiance from this air mass 1 radiance distribution interacts with a near maximum of the volume scattering function in the backscattering direction. This

Table 1. Backscattering Shape Factors f_b at 0 m Depth, 440 nm

	Air Mass 1						Air Mass 2					
	f_b	f_{bw}	f_{bq}	f_{bo}	f_{bb}	f_{ba}	f_b	f_{bw}	f_{bq}	f_{bo}	f_{bb}	f_{ba}
0.05 mg m^{-3} chlorophyll												
Bacteria	1.490	1.371	2.359	$\cdots$	0.861	0.587	1.026	1.138	0.858	$\cdots$	0.167	0.734
No Bacteria	1.391	1.368	2.351	0.728	$\cdots$	0.592	1.055	1.139	0.848	0.893	$\cdots$	0.738
1.0 mg m^{-3} chlorophyll												
Bacteria	1.474	1.385	2.40	$\cdots$	0.847	0.570	0.998	1.147	0.855	$\cdots$	0.129	0.717
No Bacteria	1.340	1.383	2.39	0.717	$\cdots$	0.570	1.037	1.140	0.894	0.854	$\cdots$	0.723
20.0 mg m^{-3} chlorophyll												
Bacteria	0.990	1.390	2.596	0.713	0.847	0.845	0.814	1.152	0.843	0.884	0.118	0.716
No bacteria	0.918	1.389	2.592	0.714	$\cdots$	0.846	0.915	1.151	0.844	0.884	$\cdots$	0.718

The subscripts with f_b are defined as follows: w, water; q, quartzlike; o, organic detritus; b, bacteria; and a, algae.
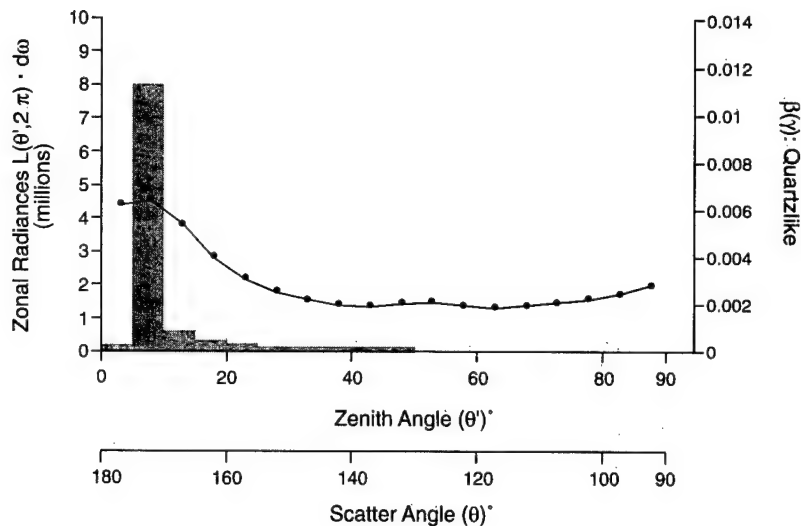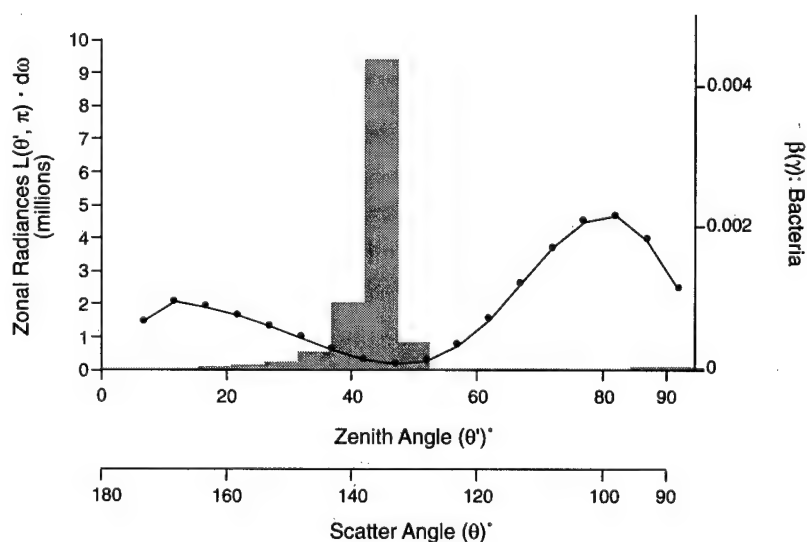
Figure 9. Data plotted from output of Naval Research Laboratory (NRL) Monte Carlo model. Simulation is at 440 nm with 20.0 mg Chl m^{-3} at 0 m depth and air mass 1. Downwelling zonal radiance distribution is each zonal radiance multiplied by $d\omega$, $L(\Theta', 2\pi, 0-)d\omega$. Backscattering lobe of volume scattering function (quartzlike material) will scatter radiant flux from the zonal radiance into the nadir radiance. Maximum zonal radiance at 7.5° zenith angle interacts with a maximum in the backscattering lobe of the volume scattering function. This explains the maximum in backscattering shape factor for quartzlike material in Table 1.

leads to a much greater amount of energy being scattered into the nadir radiance and a high value of f_{bq} for quartzlike material. In Figure 10 we have a similar plot of an air mass 2 zonal radiance distribution, $L(\Theta', 2\pi)d\omega$, against the backscattering lobe of bacteria. The dominant zonal radiance from the air mass 2 distribution interacts with a minimum in the bacterial volume scattering function in the backscattering direction. Thus the bacteria under air mass 2 conditions will

contribute a minimum to the backscattered flux entering the nadir radiance and resulting in a very low value of f_{bb} for bacteria. One merely has to shift the radiance distribution in the plots to predict the effects of changes in air mass on the backscattering shape factor. The two dominant factors controlling the backscattering shape factor are the radiance distribution of the downwelling light field and the shape of the volume scattering function of the scattering particle.

Figure 10. Data plotted from output of NRL Monte Carlo model. Simulation is at 440 nm with 20.0 mg Chl m^{-3} at 0 m depth and air mass 2. Downwelling zonal radiance distribution is each zonal radiance multiplied by $d\omega$, $L(\Theta', 2\pi, 0-)d\omega$. Backscattering lobe of volume scattering function (bacteria) will scatter radiant flux from the zonal radiance into the nadir radiance. Maximum zonal radiance at 42.5° zenith angle interacts with a minimum in the backscattering lobe of the volume scattering function. This explains the minimum in backscattering shape factor for bacteria in Table 1.
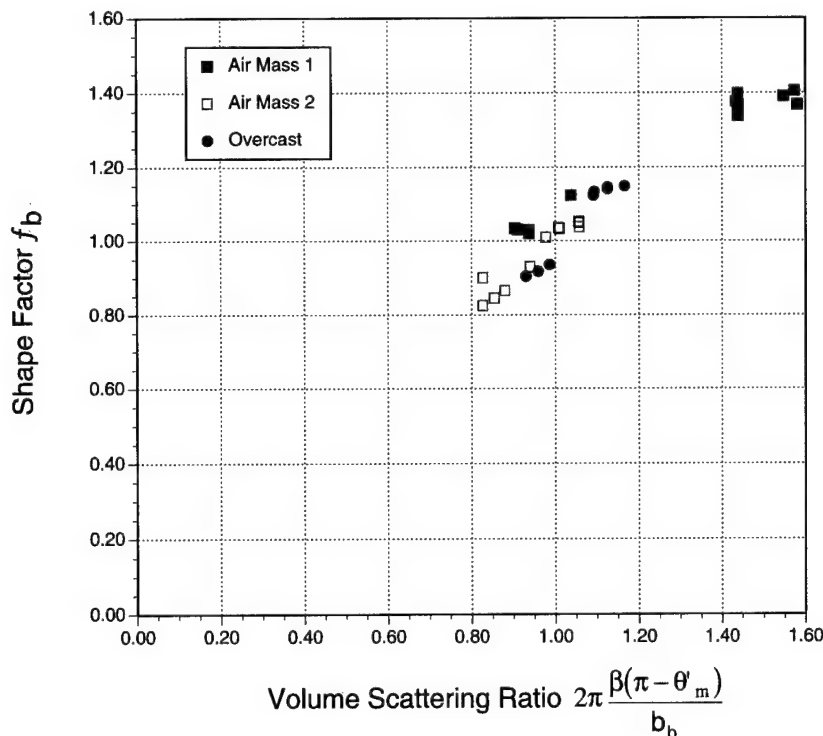
Figure 11. Backscattering shape factors calculated from the NRL Monte Carlo output compared with the volume scattering ratio. Comparisons are made from the entire range of chlorophyll concentrations, 0.05–20.0 mg m^{-3}.

Direct Estimation of f_b

Given the number of variations in the backscattering shape factor documented above, it may be difficult to simulate enough oceanic conditions to estimate the probable f_b value for a given oceanic region; alternatively, it may be possible to estimate f_b from specific oceanic optical measurements. To the end of determining f_b directly, consider an approximation of the $E_{od}(z)$ term used in these equations utilizing the maximum radiance, usually at the refracted solar zenith angle (see also *Zaneveld* [this issue]). If $L(\Theta'_m, \phi'_m, z)$ is the dominant or maximum radiance, then we make the approximation

$$E_{od}(z) \simeq \int_{\Omega_m} L(\theta'_m, \phi'_m, z) \, d\omega_m, \tag{10}$$

where $d\omega_m = \sin \Theta'_m d\Theta'_m d\phi'_m$. Substituting into (5)

$$f_b(z) \approx \frac{\displaystyle\int_{\Omega_m} \beta(\pi - \theta'_m, z)L(\theta'_m, \phi'_m, z) \, d\omega_m}{\dfrac{b_b(z)}{2\pi} E_{od}(z)}, \tag{11}$$

$$f_b(z) \approx \frac{\beta(\pi - \theta'_m, z)E_{od}(z)}{\dfrac{b_b(z)}{2\pi} E_{od}(z)}, \tag{12}$$

$$f_b(z) \approx 2\pi \frac{\beta(\pi - \theta'_m, z)}{b_b(z)}. \tag{13}$$

In Figure 11 we compare the volume scattering ratio formulation for f_b (equation (13)) with the f_b calculated from Monte Carlo output. The deviations from the true value average about 5%, whereas the worst case deviation is about 13%. The best general agreement appears to be for air mass 2 conditions, while total overcast conditions deviate a bit more. The greatest deviation appears to occur for air mass 1 conditions at high f_b values for open ocean conditions with low chlorophyll concentration. The f_b values reported in Figure 11 are averages over the first attenuation length of the surface layers. The agreement of the volume scattering ratio with the f_b value at 0 m depth is even better. Under air mass 1 conditions the agreement at 0 m depth is very good because a dominant radiance is easily identified. Diffusion of the downwelling radiance field, perhaps in a nonlinear fashion, degrades the agreement between measurement and prediction as depth increases. Under air mass 2 and overcast conditions the radiance distribution around the dominant radiance tends to be more symmetrical and the errors in identifying a dominant radiance tend to cancel out.

From the above evidence we conclude that for the first time it is possible to estimate a rather difficult optical parameter, the backscattering shape factor, utilizing the ratio of the volume scattering function at the angle $(\pi - \Theta'_m)$ to the backscattering coefficient b_b. Thus the f_b coefficient can be approximated on the assumption that the nadir radiance is populated with photons largely from single scattering at a dominant downwelling radiance. This parameter should be measurable very soon, with the development of backscattering meters that will allow an interpolation of the volume scattering function in the backscattering lobe.

The radiance needed to determine the zenith angle at which to apply the volume scattering function may be determined by knowledge of just the angle of the refracted solar beam. For cloudier skies and differing sea state conditions, Monte Carlo simulations will be needed to determine the typical dominant radiance. There are possibilities for mapping regions of specific f_b factors relative to air mass and sea state conditions, and new algorithms utilizing $\beta(\pi - \Theta'_m, z)$ are being proposed by *Zaneveld* [this issue].

Backscattering: Water, Algae, and Bacteria

The abrupt change in the mean percent error in the retrieval of b_b near 1.25 mg m^{-3} chlorophyll (Figures 3 and 4) shows that absorption and scattering partitioning is important in the performance of (7) and also for most remote sensing algorithms. Several simulations are carried out between 1.0 and 2.0 mg m^{-3}, where the recovery of b_b changes the most. The sensitivity of this change to the variation in cell model input values at 1 mg m^{-3} chlorophyll concentration is investigated as follows. We employ "nonstandard" simulations utilizing the large-cell model at and below 1.0 mg m^{-3} chlorophyll concentration and the small-cell model for chlorophyll concentrations above 1.0 mg m^{-3}. The use of the large-cell model at chlorophyll concentrations of 1.0 mg m^{-3} or less did not affect the trends reported from the "standard" model simulations (small-cell model at 1.0 mg m^{-3} chlorophyll or less). However, use of the small-cell model for chlorophyll concentrations $>$1.0 mg m^{-3} did affect the transition point for the mean percent error and f_b (Figures 3, 4, 7, and 8). Rather than declining in f_b and mean percent error between 1.0 and 1.25 mg m^{-3} chlorophyll, the transition point now occurs between 1.25 and 1.50 mg m^{-3}. However, the decrease in f_b and the mean percent error is as pronounced in these nonstandard simulations as those reported for the standard simulations (Figures 3 and 7). Keep in mind that small movement in the position of the falloff (transition) of f_b and the mean percent error in these nonstandard simulations occurs with a 2.5-fold decrease in the specific absorption coefficient, and a sixfold increase in the b_{bp}/b_p ratio. Thus the change in cell model parameters is not responsible for the general hyperbolic shape found in the simulations and the drastic change in f_b with increasing chlorophyll concentration. Therefore, even though the model is affected by the cell model parameters, factors other than the phytoplankton optical properties alone are crucial in determining the region of the rapid change in mean percent error and f_b.

On the basis of (13) it is seen that the answer lies in the following two areas: the relative contribution to scattering, backscattering, and absorption of "conservative" fractions (water, quartzlike material, background bacteria, and detritus) compared to the phytoplankton contribution and, secondly, the modification of the shape of the volume scattering function in the backward direction by constituents such as quartzlike material, phytoplankton, and bacteria. Thus the abrupt change in f_b and the rapid change in the mean percent error are brought about when the system switches from one dominated by conservative material (bacteria, quartzlike material, and water) to one dominated by the phytoplankton and its codependencies.

The presence or absence of bacteria affects the values of f_b (Figures 7 and 8). There is a clear difference between f_b

with and without bacteria for both the air mass 1 and air mass 2 simulations. In air mass 1 the f_b values with bacteria are higher than those without bacteria present; the converse is true for air mass 2. Bacteria apparently contribute more than organic detritus to backscattering for the low zenith angles (high Sun). However, for air mass 2, with a refracted solar zenith angle near the Brewster's angle, the largest contribution to the backscattering comes from near the 135° scattering angle (Figure 10). This scattering angle is near the minimum in the volume scattering function for bacteria (Figure 10). The scattering function for the backward direction at this angle is very different when bacteria are present versus when bacteria are excluded. It is this minimum and the "lobing" in the shape of the backscattering function for bacteria (Figures 1 and 10) that give rise to the distinct separation of the model output, an increase in the shape factor with a high Sun and a decrease in the shape factor with a low Sun.

Morel and Gentili [1991, 1993] put forth the parameters η, the ratio of b_w to b_T, and η_b, the ratio of b_{bw} to b_{bT}, where b_{bw} and b_{bT} are the backscattering attributable to water and the total backscattering, respectively. They then partitioned the marine hydrosol into two components: molecular water and an "average" particulate material. Furthermore, they proposed that the η and η_b parameters are directly correlated with the unique nature of the volume scattering function for the marine hydrosol. To the extent that the volume scattering function of all the particulates (bacteria, organic detritus, phytoplankton, etc.) can be summed and described by a single average function, it was proposed that the value of η and η_b describe the shape of the volume scattering function of the marine hydrosol and its backscattering function, respectively. Since each individual component of the marine hydrosol is treated separately in our simulations, an increase in chlorophyll implies an increased influence of the volume scattering function of the phytoplankton relative to the influence of all other components. The shape of the hydrosol volume scattering function changes accordingly. Since the particulate volume scattering function of Morel and Gentili remains constant for all chlorophyll concentrations, we contend that too much information about the scattering function is lost when parameterizations involving these simple ratios of scattering coefficients are utilized and therefore should not be employed in inversion techniques. There is too much variability in the scattering functions of the various hydrosol components, as we will demonstrate.

The parameter η at low chlorophyll concentrations is dominated by water, quartzlike material, and background bacteria concentration (there is no organic contribution at our lowest chlorophyll concentrations; bacteria are serving in the role of "organic detritus"). When the volume scattering function is dominated by these constituents, the value of f_b remains high and stable (Figures 12 and 13) due to the contribution of the quartzlike material and water. The high and stable f_b values exist over a broad range of η values, indicating essentially no functional relationship between the two parameters below the chlorophyll concentration of 1 mg m^{-3}. However, with increasing chlorophyll concentration there is a lessening of the dominance by water and the quartzlike material and an increase in the influence of phytoplankton absorption and scattering. No single relationship between η and f_b develops, but rather, several relationships occur that vary with compositional makeup of the
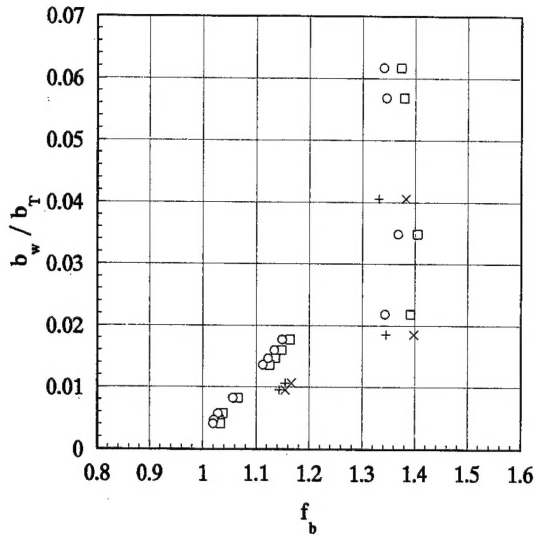
Figure 12. Fraction of total scattering attributed to molecular water η as a function of the shape factor f_b for air mass 1, all simulations; symbols as in Figure 3.

water. The region of transition lies between 1.0 and 1.25 mg m^{-3} chlorophyll. At least three different relationships appear between f_b and η based on the presence or absence of bacteria and presence of the small-cell phytoplankton model. Thus Figures 12 and 13 show that the total scattering ratio η does not tell us enough about the shape factors affecting the upwelled radiance. The three different relations at low η indicate that shape is important, but the effect is impossible to resolve. Likely, any change in the dominant scattering particle type will yield yet another unique functional relationship.

Since f_b is controlled by the shape of the volume scattering function in the backward direction (Figures 1, 2, 9, and 10 and equation (5)), one could argue that a strong relationship should exist between η_b and f_b. Morel and Gentili [1991, 1993] showed that the coefficient of proportionality between b_b/a and irradiance ratio (reflectance: ratio $R = E_u/E_d$), defined as the "f factor," is a function of η_b, the solar angle, and to some extent, the ratio of b/c. Functionally, f_b has similar dependencies, but they account for more than the f factor discussed by Morel and Gentili. Consider the following from Morel and Gentili [1993], where L_u is the nadir radiance [$= L(\pi)$]

$$\frac{L_u}{E_d(0-)} = \frac{f}{Q}\frac{b_b}{a}, \qquad (14)$$

where

$$E_d(0-) = \bar{\mu}_d(0-)E_{od}(0-), \qquad (15)$$

and substituting into (14)

$$\frac{L_u}{E_{od}(0-)} = \text{RSR} = \bar{\mu}_d(0-)\frac{f}{Q}\frac{b_b}{a}, \qquad (16)$$

then substituting into (5), replacing c with $(a + b)$, and rearranging

$$f_b = 2\pi\bar{\mu}_d(0-)\frac{f}{Q}\left[\frac{k(\pi) + b_b}{a} + 1 + (1 - f_L)\frac{b_f}{a}\right], \qquad (17)$$

and allowing $f_L = 1.0$

$$f_b \simeq 2\pi\bar{\mu}_d(0-)\frac{f}{Q}\left[\frac{k(\pi) + b_b}{a} + 1\right]. \qquad (18)$$

Recalling that the hemispherical scalar downwelling irradiance is used in the definition of RSR, we see that the f_b factor contains terms that are similar to the formulation of Morel and Gentili and others, but there is an extra term present, the downwelling mean cosine, $\bar{\mu}_d(0-)$, near the water/air interface. The $k(\pi)$ coefficient can be considered a function of b_b and a. The downwelling mean cosine, containing information about the radiance distribution of the downwelling hemisphere of the light field, provides information about the geometry of the light-particle interaction that is not available to the f factor.

The possible dependency of f_b on η_b is investigated further by examining the relationship between the ratio of backscattering attributable to water and the total backscattering (b_{bw}/b_{bT}). This is shown in Figure 14 (air mass 1) and Figure 15 (air mass 2). Two different functionalities emerge when the results from the two air masses are compared. The two different functionalities display the effect on f_b of interaction between the dominant radiance source and the shape of the volume scattering function in the backward direction (Figures 9 and 10). For air mass 1 there is nearly a linear relationship between η_b and f_b over all the simulations from chlorophyll concentrations of 0.05 to 20 mg m^{-3} (Figure 14). The presence or absence of bacteria shifts the relationship slightly. Thus, for remote sensing inversion with the Sun near the zenith, one can hypothesize that f_b could be estimated from η_b with reasonable accuracy. This result suggests either that the influences on f_b from quartz, bacteria, and phytoplankton compensate for one another or that the backscattering functions scattering into the nadir from the dominant radiance source are nearly identical for all the constituents and thus have a simple relationship with η_b. It must be pointed out that our η_b include highly variable
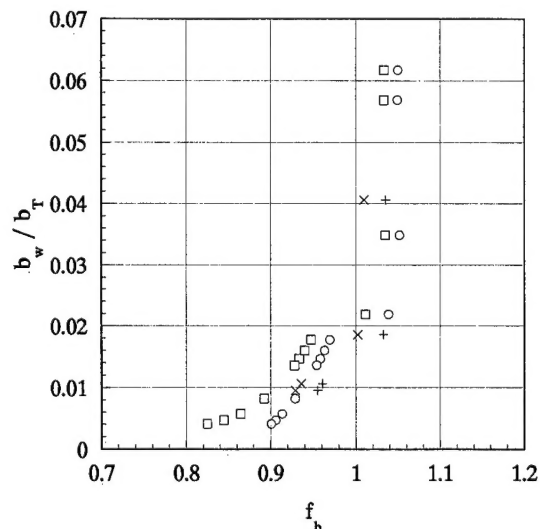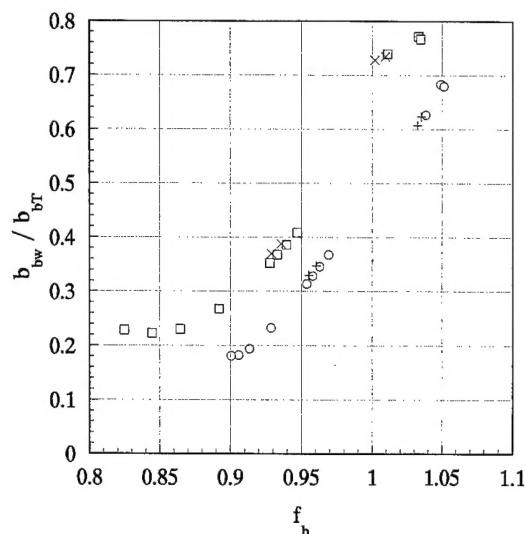

Figure 13. Fraction of total scattering attributed to molecular water η as a function of shape factor f_b for air mass 2, all simulations; symbols as in Figure 3.

shapes of $\beta(\gamma)$, whereas *Morel and Gentili* [1991, 1993] do not allow such variability.

For air mass 2 the minimum and the lobing in the shape of the backscattering function for bacteria (Figures 1 and 10) give rise to the distinct separation of the model output with and without bacteria (Figure 15). The lobate shape of the backscattering function for bacteria results in low f_b values for a given value of η_b. The curves at the higher f_b values of Figure 15 are parallel, as in Figure 14, but widely separated; there is no discernible relationship at the lower f_b values. The sudden changes in f_b are absent until concentrations of 5–10 mg m^{-3} chlorophyll are obtained, at which point b_{bT} is controlled by phytoplankton and bacteria and not by the other constituents. The significance is in the separation of the curves with and without bacteria. While bacteria do not change the total scattering, their presence does influence the magnitude of scattering into the nadir from particular angles (Figures 1 and 10). Here the use of η_b as a parameterization of the backscattering function is inappropriate and falls apart. The shape factor f_b changes by about 8% just by changing the constituents in the water. The results suggest that for inversion of remote sensing signals, use of only scattering functions for molecular water and San Diego Harbor particulates, as in the work by *Morel and Gentili* [1993], is insufficient.

## Implications and New Inversion Techniques

Zaneveld's [1982] RSR model (equation (4)) is correct; however, the assumption that f_b and, to a lesser extent, f_L are approximately 1.0 is not appropriate over the range of the phase functions studied here, and the modified formulation [*Zaneveld*, this issue] should be used. The results from this study have several implications for modifications needed in the approximate equations derived from the exact RSR model. The most important point is the dependency of f_b (or the mean percent errors) on solar angle and the shape of the volume scattering function for the backward direction for the constituents in the water (i.e., bacteria, quartzlike material,

Figure 15. Fraction of total backscattering attributed to molecular water η_b as a function of f_b for air mass 2, all simulations; symbols as in Figure 3.

etc.). Such information, as we have demonstrated here, is necessary in order to predict b_b to accuracies better than 30%, and this type of information is becoming available. It is worth noting that this range of uncertainty of the method discussed here based on the RSR utilizing the downwelling hemispherical scalar irradiance demonstrates nearly an order of magnitude improvement over the uncertainties inherent in other remote sensing inversion schemes that employ only the reflectance ratio R. *Zaneveld* [this issue] has proposed an analytic derivation with successive approximations of the exact RSR inversion which includes the solar angle (for the dominant radiance in the downwelling direction) and the volume scattering function (in the backward direction) derived in part from the results presented in the Direct Estimation of f_b section. The difficulty becomes knowing the volume scattering function a priori to any degree of accuracy. New schemes for measuring and mapping the backscatter coefficient and estimating the backscattering lobe of the volume scattering function in the ocean will potentially alleviate this problem. The estimation of b_b from $\beta(\pi - \theta_m)$ is only as good as our estimation of the shape of $\beta(\gamma)$. Using various solar angles zenith angles may allow $\beta(\gamma)$ to be approximated from remote sensing.

Another conclusion from these simulations with important implications is the stability of the mean percent error and f_b relationships for open ocean conditions even when optical properties of algae are changed significantly. The nonstandard simulations did not alter the conclusions; the inflection value of f_b or the mean percent error in backscattering retrieval occurs in a relatively narrowly defined region of chlorophyll concentration, 1.0–1.5 mg m^{-3}. Clearly, the importance of water and other nonalgal material is evident. *Morel and Ahn* [1991] have suggested that larger algae are practically inoperative in the backscattering process when case 1 situations are extended to high-chlorophyll regimes at >1 mg m^{-3}. However, in our model the effect of larger algae on backscattering increases with the increase in chlorophyll concentration. At the highest chlorophyll levels the backscattering due to algae is of the same order as the backscat-
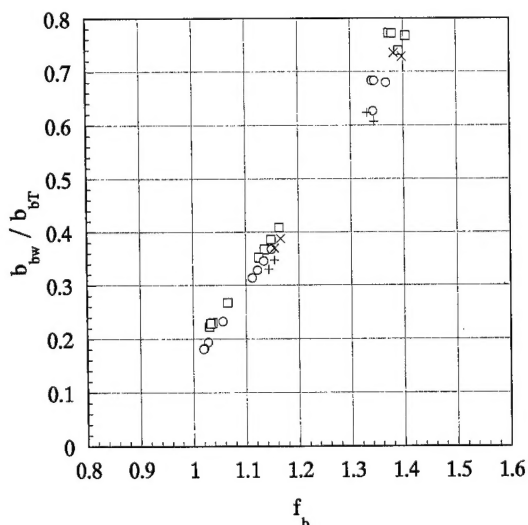
Figure 14. Fraction of total backscattering attributed to molecular water η_b as a function of f_b for air mass 1, all simulations; symbols as in Figure 3.

tering due to the water molecule. The overall pattern is one in which the algae, once the transition point at 1 mg m^{-3} is exceeded, reduce the shape factors in magnitude and allow simpler algorithms to be used to retrieve the backscattering coefficient.

In addition, still other relationships have been demonstrated with our model, which takes the optical properties of individual hydrosol components into account. For example, the potential importance of bacteria to measurements of remote sensing reflectance has not been well documented or appreciated, although *Morel* [1991] and *Stramski and Kiefer* [1991] have called attention to bacterial effects on hydrosol scattering. Of potential importance for case 2 waters are the results on the effect of the quartzlike material partitioning of f_b (Table 1). This material is primarily responsible for the very high values of f_b for low chlorophyll concentration with a high Sun (low zenith angle). This effect is then negated with a low Sun (high zenith angle). The implication is that the backscattering function must be known in some detail for retrieval of the inherent properties to be carried out in an analytic manner.

Notation

a	absorption coefficient (total), m^{-1} ($=a_T$).
a_{bact}	bacterial absorption coefficient, m^{-1}.
a_d	detrital absorption coefficient, m^{-1} ($=a_o + a_{bact}$).
a_o	organic detrital absorption coefficient, m^{-1}.
a_p	phytoplankton absorption coefficient, m^{-1}.
a_y	yellow substance (dissolved) absorption coefficient, m^{-1}.
a_w	water absorption coefficient, m^{-1}.
b	scattering coefficient (total), m^{-1} ($=b_T$).
b_{bact}	bacterial scattering coefficient, m^{-1}.
b_d	detrital scattering coefficient, m^{-1} ($=b_o + b_{bact}$).
b_o	organic detrital scattering coefficient, m^{-1}.
b_p	phytoplankton scattering coefficient, m^{-1}.
b_q	quartzlike material scattering coefficient, m^{-1}.
b_w	water scattering coefficient, m^{-1}.
b_b	backscattering coefficient, m^{-1}.
b_f	forward scattering coefficient, m^{-1}.
$\beta(\gamma)$	volume scattering function, m^{-1} sr^{-1}.
c	beam attenuation coefficient, m^{-1}.
$\bar{\varepsilon}$	mean percent error of b_b retrieval.
E_d	downwelling plane irradiance, W m^{-2}.
E_{od}	downwelling scalar irradiance, W m^{-2}.
E_u	upwelling plane irradiance, W m^{-2}.
f	ratio of R to b_b/a.
f_b	backscattering shape factor.
f_{ba}	algal backscattering shape factor.
f_{bb}	bacterial backscattering shape factor.
f_{bo}	organic detritus backscattering shape factor.
f_{bq}	quartzlike backscattering shape factor.
f_{bw}	water backscattering shape factor.
f_L	radiance shape factor.
ϕ	azimuth angle.
ϕ'	azimuth angle of radiance contributing to path radiance.
γ	scattering angle.
K_d	vertical attenuation coefficient for downwelling plane irradiance, m^{-1}.
$k(\pi)$	vertical attenuation coefficient for nadir radiance, m^{-1}.
k_∞	asymptotic vertical attenuation coefficient for nadir radiance, m^{-1}.
L	radiance, W m^{-2} sr^{-1}.
L^*	path radiance, W m^{-3} sr^{-1}.
$\bar{\mu}_d$	downwelling mean cosine.
λ	wavelength, nm.
θ	zenith angle.
θ'	zenith angle of radiance contributing to path radiance.
Q	ratio of upwelling irradiance to the upwelling nadir radiance, sr.
R	reflectance ratio.
RSR	remotely sensed reflectance, sr^{-1}.
z	depth, m.

References

Baker, K. S., and R. Frouin, Relation between photosynthetically available radiation and total insolation at the ocean surface under clear skies, *Limnol. Oceanogr.*, *32*, 1370–1377, 1987.

Bohren, C. F., and D. R. Huffman, *Absorption and Scattering of Light by Small Particles*, John Wiley, New York, 1983.

Bricaud, A., and A. Morel, Light attenuation and scattering by phytoplanktonic cells, *Appl. Opt.*, *25*, 571–580, 1986.

Bricaud, A., and D. Stramski, Spectral absorption coefficients of living phytoplankton and nonalgal biogenous matter: A comparison between the Peru upwelling area and the Sargasso Sea, *Limnol. Oceanogr.*, *35*, 562–582, 1990.

Bricaud, A., A. L. Bedhomme, and A. Morel, Optical properties of diverse phytoplanktonic species: Experimental results and theoretical interpretation, *J. Plankton Res.*, *10*, 851–873, 1988.

Brine, D. T., and M. Iqbal, Diffuse and global solar spectral irradiance under cloudless skies, *Sol. Energy*, *30*, 447–453, 1983.

Carder, K. L., R. G. Steward, J. H. Paul, and G. A. Vargo, Relationships between chlorophyll and ocean color constituents as they affect remote-sensing reflectance models, *Limnol. Oceanogr.*, *31*, 403–413, 1986.

Cho, B. C., and F. Azam, Biogeochemical significance of bacterial biomass in the ocean's euphotic zone, *Mar. Ecol. Prog. Ser.*, *63*, 253–259, 1990.

Cleveland, J., A model of absorption by phytoplanktonic and detrital particles in the ocean and applications to photosynthetic quantum yield and *in vivo* fluorescence, Ph.D. thesis, Univ. of Wash., Seattle, 1988.

Cleveland, J., Regional models for phytoplankton absorption as a function of chlorophyll *a* concentration, *J. Geophys. Res.*, this issue.

Cole, J. J., S. Findlay, and M. L. Pace, Bacterial production in fresh and saltwater ecosystems: A cross-system overview, *Mar. Ecol. Prog. Ser.*, *43*, 1–10, 1988.

Dickey, T., J. Marra, T. Granata, C. Langdon, M. Hamilton, J. Wiggert, D. Siegel, and A. Bratkovich, Concurrent high resolution bio-optical and physical time series observations in the Sargasso Sea during the Spring of 1987, *J. Geophys. Res.*, *96*, 8643–8663, 1991.

Gallegos, C. L., D. L. Correll, and J. W. Pierce, Modeling spectral diffuse attenuation, absorption, and scattering coefficients in a turbid estuary, *Limnol. Oceanogr.*, *35*, 1486–1502, 1990.

Gershun, A. A. The light field, *J. Math. Phys.*, *18*, 51–151, 1939.

Gordon, H. R., Dependence of the diffuse reflectance of natural waters on the sun angle, *Limnol. Oceanogr.*, *34*, 1484–1489, 1989.

Gordon, H. R., and D. K. Clark, Remote sensing optical properties of a stratified ocean: An improved interpretation, *Appl. Opt.*, *19*, 3428–3430, 1980.

Gordon, H. R., and A. Morel, Remote assessment of ocean color for interpretation of satellite visible imagery, in *Lecture Notes on Coastal and Estuarine Studies*, edited by R. T. Barber, C. K. Mooers, M. J. Bowman, and B. Zeitzschel, pp. 1–113, Springer-Verlag, New York, 1983.

Gordon, H. R., O. B. Brown, R. H. Evans, J. W. Brown, R. C. Smith, K. S. Baker, and D. K. Clark, A semianalytic radiance model of ocean color, *J. Geophys. Res.*, *93*, 10,909–10,924, 1988.

Kitchen, J. C., and J. R. V. Zaneveld, On the noncorrelation of the vertical structure of light scattering and chlorophyll *a* in case I waters, *J. Geophys. Res.*, *95*, 20,237–20,246, 1990.

Kullenberg, G., Scattering of light by Sargasso Sea water, *Deep Sea Res.*, *15*, 423–432, 1968.

Lee, Z., K. L. Carder, S. K. Hawes, R. G. Steward, T. G. Peacock, and C. O. Davis, A model for interpretation of hyperspectral remote-sensing reflectance, *Appl. Opt.*, *33*, 5721–5731, 1994.

Marees, G., and M. R. Wernand, Interpretation of optical remote sensing data over coastal waters, *Rep. BCRS 91-27*, 105 pp., Beleidscomm. Remote Sens., Texel, Netherlands, 1991.

Mobley, C. D., B. Gentili, H. R. Gordon, Z. Jin, G. W. Kattawar, A. Morel, P. Reinersman, K. Stamnes, and R. H. Stavn, Comparison of numerical models for computing underwater light fields, *Appl. Opt.*, *32*, 7484–7504, 1993.

Morel, A., Optical properties of pure water and pure seawater, in *Optical Aspects of Oceanography*, edited by N. G. Jerlov and E. Steeman Nielsen, pp. 1–24, Academic, San Diego, Calif., 1974.

Morel, A., In-water and remote measurement of ocean color, *Boundary Layer Meteorol.*, *18*, 177–201, 1980.

Morel, A., Chlorophyll-specific scattering coefficient of phytoplankton. A simplified theoretical approach, *Deep Sea Res., Part A*, *34*, 1093–1105, 1987.

Morel, A., Optical modeling of the upper ocean in relation to its biogenous matter content (case I waters), *J. Geophys. Res.*, *93*, 10,749–10,768, 1988.

Morel, A., Optics of marine particles and marine optics, in *Particle Analysis in Oceanography*, *NATO ASI Ser., Ser. G*, edited by S. Demers, pp. 141–189, Springer-Verlag, New York, 1991.

Morel, A., and Y. H. Ahn, Optical efficiency factors of free-living marine bacteria: Influence of bacterioplankton upon the optical properties and particulate organic carbon in oceanic waters, *J. Mar. Res.*, *48*, 145–175, 1990.

Morel, A., and Y. H. Ahn, Optics of heterotrophic nanoflagellates and ciliates: A tentative assessment of their scattering role in oceanic waters compared to those of bacterial and algal cells, *J. Mar. Res.*, *49*, 177–202, 1991.

Morel, A., and A. Bricaud, Inherent optical properties of algal cells including picoplankton: Theoretical and experimental results, *Can. Bull. Fish. Aquat. Sci.*, *214*, 521–559, 1986.

Morel, A., and B. Gentili, Diffuse reflectance of oceanic waters: Its dependence on Sun angle as influenced by the molecular scattering contribution, *Appl. Opt.*, *30*, 4427–4438, 1991.

Morel, A., and B. Gentili, Diffuse reflectance of oceanic waters, 2, bi-directional aspects, *Appl. Opt.*, *32*, 6864–6879, 1993.

Petzold, T. J., Volume scattering functions for selected ocean waters, *Rep. SIO Ref. 72-78*, 79 pp., Scripps Inst. of Oceanogr., La Jolla, Calif., 1972.

Preisendorfer, R. W., *Hydrologic Optics*, vol. 6, U.S. Department of Commerce, Washington, D. C., 1976.

Prieur, L., and S. Sathyendranath, An optical classification of coastal and oceanic waters based on the specific spectral absorption curves of phytoplankton pigments, dissolved organic matter, and other particulate materials, *Limnol. Oceanogr.*, *26*, 671–689, 1981.

Smith, R. C., and K. S. Baker, Optical properties of the clearest natural waters (200–800 nm), *Appl. Opt.*, *20*, 177–184, 1981.

Stavn, R. H., and A. D. Weidemann, Optical modeling of ocean light fields: Raman scattering effects, *Appl. Opt.*, *27*, 4002–4010, 1988.

Stavn, R. H., and A. D. Weidemann, Shape factors, two-flow models, and the problem of irradiance inversion in estimating optical parameters, *Limnol. Oceanogr.*, *34*, 1426–1441, 1989.

Stavn, R. H., and A. D. Weidemann, Geometrical light field parameters for improving remote sensing estimates of the backscattering in the marine hydrosol, Ocean Optics 12, *2258*, *Proc. SPIE Int. Soc. Opt. Eng.*, 202–209, 1994.

Stramski, D., and D. Kiefer, Light scattering by microorganisms in the open ocean, *Prog. Oceanogr.*, *28*, 343–383, 1991.

Zaneveld, J. R. V., Remotely sensed reflectance and its dependence on vertical structure: A theoretical derivation, *Appl. Opt.*, *21*, 4146–4150, 1982.

Zaneveld, J. R. V., A theoretical derivation of the dependence of the remotely sensed reflectance of the ocean on the inherent optical properties, *J. Geophys. Res.*, this issue.

R. H. Stavn, Department of Biology, University of North Carolina, Greensboro, NC 27412.

A. D. Weidemann, Naval Research Laboratory, Stennis Space Center, MS 39529. (e-mail:alanw@indyvih.nrlssc.navy.mil)

M. R. Wilcox, Neptune Sciences, Inc., 150 Cleveland Avenue, Slidell, LA 70458.

J. R. V. Zaneveld, College of Oceanic and Atmospheric Sciences, Oregon State University, Ocean Administration Building 104, Corvallis, OR 97331.